

AD-A090 531

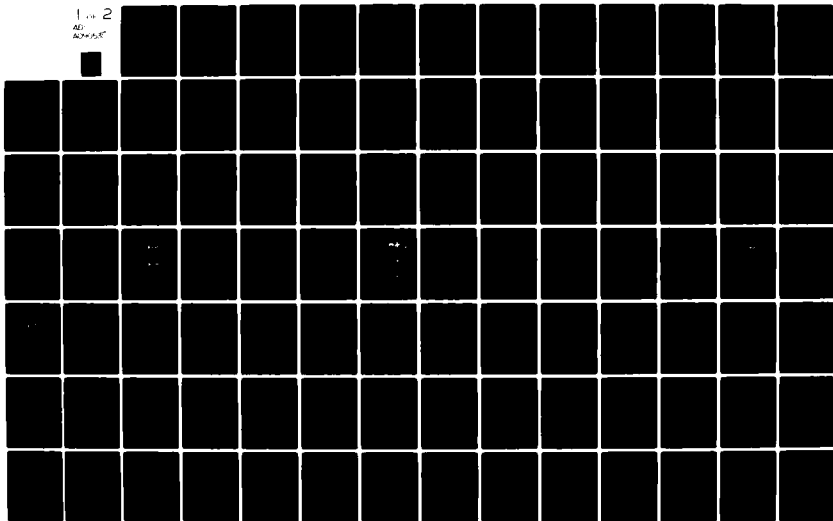
NEW MEXICO UNIV ALBUQUERQUE ERIC H WANG CIVIL ENGINE--ETC F/G 18/3
DYNAMIC AIRBLAST SIMULATOR (DABS) INSTRUMENTATION DEVELOPMENT. --ETC(U)
JUN 80 W R EDGEL, N P BAUM F29601-76-C-0015

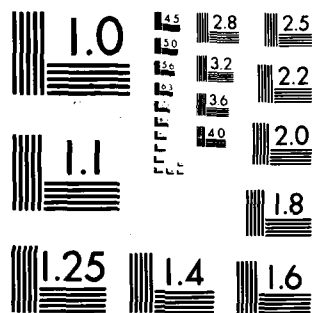
UNCLASSIFIED

AFWL-TR-79-155

NL

1 of 2
AD
A090 531





MICROCOPY RESOLUTION TEST CHART
NATIONAL BUREAU OF STANDARDS-1963-A

AFWL-TR-79-155

(12)

LEVEL III

A060 732

AFWL-TR-79-155

AD A090531

DYNAMIC AIRBLAST SIMULATOR (DABS) INSTRUMENTATION DEVELOPMENT - PHASE II

W. Reed Edgel
Neal P. Baum

Eric H. Wang Civil Engineering Research Facility
University of New Mexico
Albuquerque, NM 87131

June 1980

Final Report

Approved for public release; distribution unlimited.

This research was sponsored by the Defense Nuclear Agency
under Subtask H11CAXSX355, Work Unit 0702; Title:
Instrumentation Requirement.

Prepared for
Director
DEFENSE NUCLEAR AGENCY
Washington, DC 20305

AIR FORCE WEAPONS LABORATORY
Air Force Systems Command
Kirtland Air Force Base, NM 87117

DTIC
ELECTE
OCT 16 1980
S D B

DDC FILE COPY

80 9 11 018

This final report was prepared by Eric H. Wang, Civil Engineering Research Facility, University of New Mexico, Albuquerque, New Mexico, under Contract F29601-76-C-0015, Job Order WDNS0321 with the Air Force Weapons Laboratory, Kirtland Air Force Base, New Mexico. Mr. Joe V. Quintana (NTED-I) was the Laboratory Project Officer-in-Charge.

When US Government drawings, specifications, or other data are used for any purpose other than a definitely related Government procurement operation, the Government thereby incurs no responsibility nor any obligation whatsoever, and the fact that the Government may have formulated, furnished, or in any way supplied the said drawings, specifications, or other data, is not to be regarded by implication or otherwise, as in any manner licensing the holder or any other person or corporation, or conveying any rights or permission to manufacture, use, or sell any patented invention that may in any way be related thereto.

This report has been authored by a contractor of the United States Government. The United States Government retains a nonexclusive, royalty-free license to publish or reproduce the material contained herein, or allow others to do so, for United States Government purposes.

This report has been reviewed by the Public Affairs and is releasable to the National Technical Information Service (NTIS). At NTIS, it will be available to the general public, including foreign nations.

This technical report has been reviewed and is approved for publication.

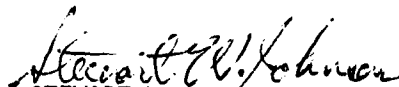


JOE V. QUINTANA
Project Officer



R. V. MATALUCCI
Lt Colonel, USAF
Chief, Simulation Branch

FOR THE DIRECTOR



STEWART W. JOHNSON
Lt Colonel, USAF
Chief, Civil Engineering Research
Division

DO NOT RETURN THIS COPY. RETAIN OR DESTROY.



UNCLASSIFIED

SECURITY CLASSIFICATION OF THIS PAGE (When Data Entered)

(16) WDNS, H11CAXS

(17) 13, X355

19 REPORT DOCUMENTATION PAGE		READ INSTRUCTIONS BEFORE COMPLETING FORM	
1. REPORT NUMBER (18) AFWL-TR-79-155	2. GOVT ACCESSION NO. AD-A090531	3. RECIPIENT'S CATALOG NUMBER	
4. TITLE (and Subtitle) (6) DYNAMIC AIRBLAST SIMULATOR (DABS) INSTRUMENTATION DEVELOPMENT, PHASE II.		5. TYPE OF REPORT & PERIOD COVERED (7) Final Report	
7. AUTHOR(s) (10) W. Reed/Edge Neal P./Baum		8. CONTRACT OR GRANT NUMBER(s) (11) F29601-76-C-0015	
9. PERFORMING ORGANIZATION NAME AND ADDRESS Eric H. Wang, Civil Engineering Research Facility University of New Mexico Albuquerque, NM 87131		10. PROGRAM ELEMENT, PROJECT, TASK AREA & WORK UNIT NUMBERS 62704H/WDNS0321	
11. CONTROLLING OFFICE NAME AND ADDRESS Air Force Weapons Laboratory (NTED-I) Kirtland Air Force Base, NM 87117		12. REPORT DATE (11) Jun 1980	
14. MONITORING AGENCY NAME & ADDRESS (if different from Controlling Office) Director Defense Nuclear Agency Washington, DC 20305		13. NUMBER OF PAGES 122 (12) 119	
		15. SECURITY CLASS. (of this report) UNCLASSIFIED	
		15a. DECLASSIFICATION/DOWNGRADING SCHEDULE	
16. DISTRIBUTION STATEMENT (of this Report) Approved for public release; distribution unlimited.			
17. DISTRIBUTION STATEMENT (of the abstract entered in Block 20, if different from Report)			
18. SUPPLEMENTARY NOTES This research was sponsored by the Defense Nuclear Agency under Subtask H11CAXSX355, Work Unit 0702; Title: Instrumentation Requirement.			
19. KEY WORDS (Continue on reverse side if necessary and identify by block number) Blast Tube Tests Infrared Detection Blast Wave Measurements Mach Number Doppler Radar Stresses Velocimeters			
20. ABSTRACT (Continue on reverse side if necessary and identify by block number) Development of explosives-driven nuclear blast simulators requires instrumenta- tion for measurements to characterize blast flow. In a series of field tests with a large shock-tube-like dynamic air-blast simulator (DABS) blast flow characterization is attempted through measurements of parameters related to dynamic pressure. Doppler radar and infrared thermometry techniques are described toward determination of detonation product interface velocity. Blunt face drag body and acoustic techniques are implemented toward determination of (Over)			

DD FORM 1 JAN 73 1473

EDITION OF 1 NOV 65 IS OBSOLETE

UNCLASSIFIED

SECURITY CLASSIFICATION OF THIS PAGE (When Data Entered)

1100116

JCB

UNCLASSIFIED

SECURITY CLASSIFICATION OF THIS PAGE(When Data Entered)

20. ABSTRACT (Cont'd)

→ flow Mach number. Other measurements include high stress and particle velocity in the walls of the explosives driver chamber using manganin sensors, conduction pins, and a mutual inductance particle velocimeter. Results of the measurement implementations indicate the soundness of the technical approaches for measurement techniques in the extremely hostile blast flow environment.

71

Accession For	
NTIS GRA&I	<input checked="checked" type="checkbox"/>
DTIC TAB	<input type="checkbox"/>
Unannounced	<input type="checkbox"/>
Justification	
By	
Distribution/	
Availability Codes	
Dist	Avail and/or Special
A	

UNCLASSIFIED

SECURITY CLASSIFICATION OF THIS PAGE(When Data Entered)

CONTENTS

<u>Section</u>	<u>Page</u>
I INTRODUCTION	5
II DOPPLER RADAR	13
III INFRARED (IR) DETECTORS	21
IV BLAST BEHIND BLAST (B ³)	67
V DRAG BODIES	81
Analysis	81
Conclusions and Recommendations	90
VI DRIVER CHAMBER MOTION MEASUREMENTS	93
Rigid-Body Motion of Chamber Back Wall	93
Shock Propagation in Chamber Back Wall	99
Particle Velocity in Chamber Back Wall	99
Stress in Chamber Back Wall	113

ILLUSTRATIONS

<u>Figure</u>	<u>Page</u>
1 Test-Bed Layout, HAVE HOST-SHELTER 1 (HH-S1) Event	8
2 Test-Bed Layout, HH-S2 Event	9
3 Test-Bed Layout, HH-S3 Event	10
4 Test-Bed Layout, DSOT-1	11
5 Developmental Instrumentation Layout, DABS-IIIA	12
6 Radar Schematic, HH-S1, S2, and S3	14
7 Radar Schematic, HH-T3	18
8 Radar Velocity Data on HH-S2	19
9 Intensity Versus Wavelength and Temperature - Blackbody Radiation	22
10 Transmission Curves for Filters	24
11 Intensity-Versus-Temperature Filtered Blackbody Radiation	26
12 Sensitivity of Lead Selenide Photoresistors	27
13 Comparison of Infrared Data with TOA Crystal and Doppler Radar Data	28
14 Infrared (IR) Detector, HH-S1	29
15 IR Detector Instrumentation, HH-S1	30
16 IR Detector Connections, HH-S2	32

ILLUSTRATIONS (Continued)

<u>Figure</u>		<u>Page</u>
17	IR Detector, HH-S2	33
18	Data From IR Detectors, HH-S2	34
19	Three-Color IR Detector, HH-S3	35
20	Wiring Diagram, IR Detectors, HH-S3	37
21	Calibration of Three-Color IR Detector Unit 1, HH-S3	39
22	Calibration of Three-Color IR Detector Unit 2, HH-S3	40
23	Data From IR Detector Unit 1, HH-S3	41
24	Reduction of HH-S3 Data from IR Detector Unit 1 (X = 15.2 m)	42
25	DPI Intensities at X = 15.2 m, HH-S3	43
26	HH-S3 Data From IR Detector 2	45
27	Reduction of HH-S3 Data From IR Detector 2 (X = 28 m)	46
28	DPI Intensities at X = 28 m, HH-S3	47
29	IR Detector Wiring, DSOT-I	48
30	Calibration of Three-Color IR Detector Unit 1, DSOT-I	49
31	Calibration of Three-Color IR Detector Unit 2, DSOT-I	50
32	DSOT-I Data from IR Detector Unit 1	51
33	Data from IR Detector Unit 2, DSOT-I	53
34	Reduction of DSOT-I Data from IR Detector Units 1 and 2	54
35	IR Detector, DABS-IIIA	55
36	IR Detector Instrumentation, DABS-IIIA	56
37	Calibration of Three-Color IR Detector, DABS-IIIA	57
38	DABS-IIIA Data from IR Detector	58
39	Reduction of DABS-IIIA IR Detector Data - DPI at Detector	60
40	Reduction of DABS-IIIA IR Detector Data, Detonation Peak	62
41	Improved Spectral Definition Resulting from Additional Data Points	65
42	Blast Behind Blast (B ³) Experiment Layout	68
43	Shock-on-Shock (SOS) Experimental Data (Gage 1 Output)	70
44	Test-Bed Layout, HH-S1 B ³ Experiment	71
45	Test-Bed Layout, HH-S2	72
46	B ³ Data HH-S2	73
47	B ³ Test-Bed Layout, HH-S3	75
48	Schematic B ³ Mixer	76

ILLUSTRATIONS (Concluded)

<u>Figure</u>		<u>Page</u>
49	B ³ Data HH-S3	77
50	B ³ Test-Bed Layout, DSOT-I Experiment	78
51	B ³ Data, DSOT-I	80
52	Drag Body Assembly	84
53	Strain/Pressure Drag Body Assembly, DABS-IIIA5	88
54	Load Cell Drag Body Response	89
55	Pre- and Posttest Calibration of a Load Cell Drag Body	91
56	Developmental Instrumentation Layout - Driver, DABS-IIIA	94
57	Gage Body - TOA Gage 2 DABS-IIIA	95
58	TOA 2 Instrumentation DABS-IIIA	97
59	DABS-IIIA Driver Motion Measurements	98
60	DABS-IIIA TOA 2 Data Reduction	100
61	TOA 1 Gage, DABS-IIIA	101
62	TOA 1 Instrumentation for DABS-IIIA	102
63	Mutual Inductance Particle Velocimeter (MIPV) Gage Undergoing Deformation from Particle Motion	104
64	MIPV Circuit Characteristics	106
65	Mutual Inductance Particle Velocimeter (MIPV)	108
66	MIPV 1 Instrumentation for DABS-IIIA	110
67	Construction and Magnetically Active Elements of an ASM Probe	112
68	Manganin Gage Cylindrical Configuration - DABS-IIIA	114
69	Manganin Gage Flat Pack Configuration - DABS-IIIA	115
70	Manganin Gage Instrumentation DABS-IIIA	116

TABLES

<u>Table</u>		<u>Page</u>
1	DABS Instrumentation Development Tests	7
2	Intensities of Filtered Blackbody Radiation	25
3	Results of Infrared Experiments	63
4	Drag Body Measurement in HH-S2	86
5	Drag Body Measurement in HH-S3	87
6	Driver Motion Measurements	93

SECTION I

INTRODUCTION

Since the signing of the Limited Nuclear Test Ban Treaty in 1963, the United States Air Force (USAF) has needed a relatively inexpensive technique for simulating airblast to approximate and test the effects of very high explosives (principally nuclear weapons) on military structures. More specifically, the USAF has sought a technique to determine airblast loadings on scale models of various shelters which have been proposed for the fourth-generation Missile X (MX). To meet this need the Air Force Weapons Laboratory (AFWL) at Kirtland Air Force Base (KAFB) in Albuquerque, New Mexico, and the University of New Mexico Civil Engineering Research Facility (UNM/CERF) have jointly developed the Dynamic Airblast Simulator (DABS) technique.

A DABS consists of a tunnel or trench with a roof covered with any given depth of overburden. A high-explosive charge is placed at one end of the tunnel and the other end left open. The DABS is sometimes referred to as a *disposable shock tube*. This description is not quite accurate, however, because a shock tube is usually made long enough to permit the blast wave to propagate for at least ten diameters before it is used for test purposes; whereas, for reasons of cost, a DABS usually has a total length less than ten "diameters" (the cross section is not generally circular). It would be more nearly correct to refer to a DABS as an *airblast director*.

The purpose of the DABS is to simulate the airblast loading that would be developed by a nuclear device at a given range. Thus the simulator must produce an airblast wave with a fast rise time and an appropriately intense peak value. To achieve this effect, it is necessary to allow the expanding detonation products behind the clean air shock to provide a significant portion of the blast loading on the structure being tested. This necessity causes great difficulty from both a theoretical and an experimental standpoint. While the equation-of-state for *clean* shocked air is well known, there is no adequate equation-of-state for the *dirty* conglomeration of detonation products. Therefore, the burden of describing the shock wave falls upon experimental methods. Unfortunately, however, the atmosphere of unknown constituents at unknown

temperatures and the high incidence of debris which defy theoretical characterization also make it very difficult to obtain meaningful measurements with which to devise an experimental description of the blast wave.

The primary variables that need to be known in order to characterize the blast wave in the DABS are the side-on or incident pressure, the shock velocity, and the dynamic pressure in the shock wave. The first two are easily and routinely measured; the third is not as easily obtained. It can be calculated from

$$Q = \rho \frac{V^2}{2} \quad (1)$$

where Q = Dynamic Pressure
 ρ = Material Density in the Flow
and V = Flow Velocity

Of these three variables, only the flow velocity can be measured directly. The overall objective of this program is the development of transducers that can obtain measurements of the variables from which the dynamic pressure in the DABS shock wave can be inferred. The variables being sought include flow velocity, the velocity of the interface between the clean air and the detonation products, stagnation pressure, temperature, Mach number of flow, and the driver chamber pressure.

The program was initiated with a series of DABS tests conducted in 1978 and 1979 at KAFB. Several techniques were tried in an effort to obtain the various desired measurements. Only some techniques were shown to be feasible. The initial (Phase I) effort is described in Reference 1. The continuation of the effort (Phase II) is the subject of this report.

The measurement systems and methods selected for further development on the basis of the Phase I results are as follows:

1. Doppler Radar, for measurement of Detonation Product Interface (DPI) velocity.

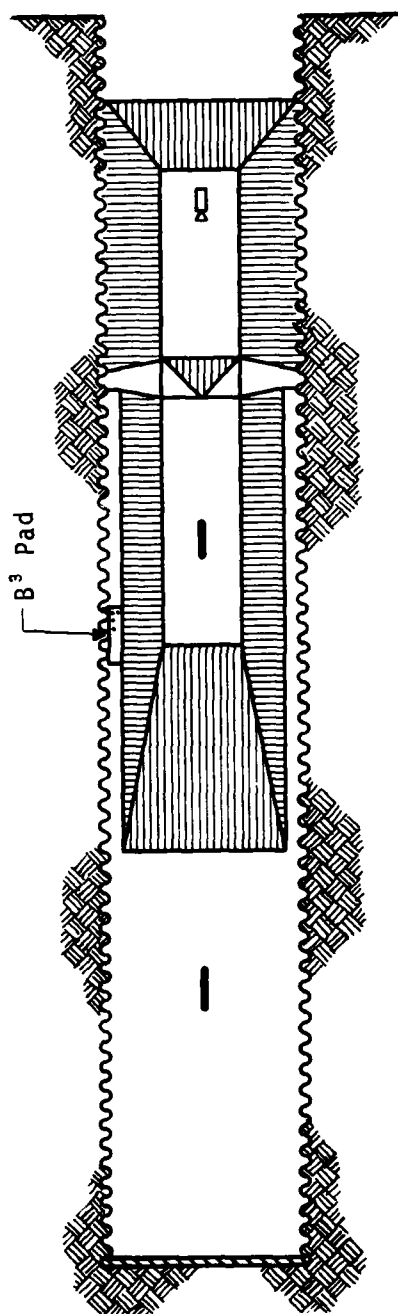
1. Baum, Neal, *Dynamic Airblast Simulator (DABS) Instrumentation Development - Phase I*, Technical Report AFWL-TR-77-6, Eric H Wang Civil Engineering Facility, University of New Mexico, Albuquerque, New Mexico, May 1978.

2. Infrared (IR) Detectors, for Time-of-Arrival (TOA) and temperature measurements on the DPI.
3. Blast Behind Blast (B^3) experiment, for determination of Mach number of flow.
4. Drag Body, for determination of flow Mach number (and stagnation pressure).
5. Driver Motion Measurements (consisting of particle and shock velocities in the back wall, rigid body motion of the back wall, and stress in the back wall) for determination of driver chamber pressure.

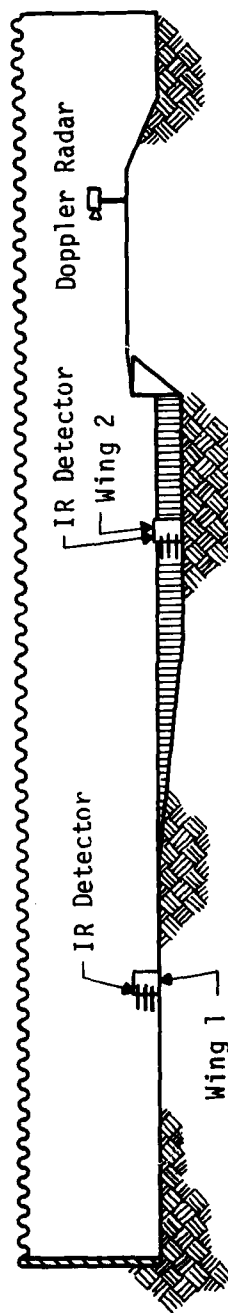
These systems and methods were tested on one or more of Events S1, S2, and S3 of the HAVE HOST (HH) series at Yuma, Arizona, and in the Dynamic Side-On Trench (DSOT) Event 1 or DABS-IIIA, the latter two experiments having been conducted at KAFB. Table 1 shows which measurements were fielded on which events, and Figures 1 through 5 show general test-bed layouts as well as the locations of the various measurements.

TABLE 1. DABS INSTRUMENTATION DEVELOPMENT TESTS

MEASUREMENT	HH-S1	HH-S2	HH-S3	DSOT-I	DABS-IIIA
Doppler Radar	X	X	X		X
IR Detectors	X	X	X	X	X
B^3	X	X	X	X	X
Drag Bodies		X	X		X
Driver Motion					X



Plan



Elevation

Figure 1. Test-Bed Layout, HH-S1 Event

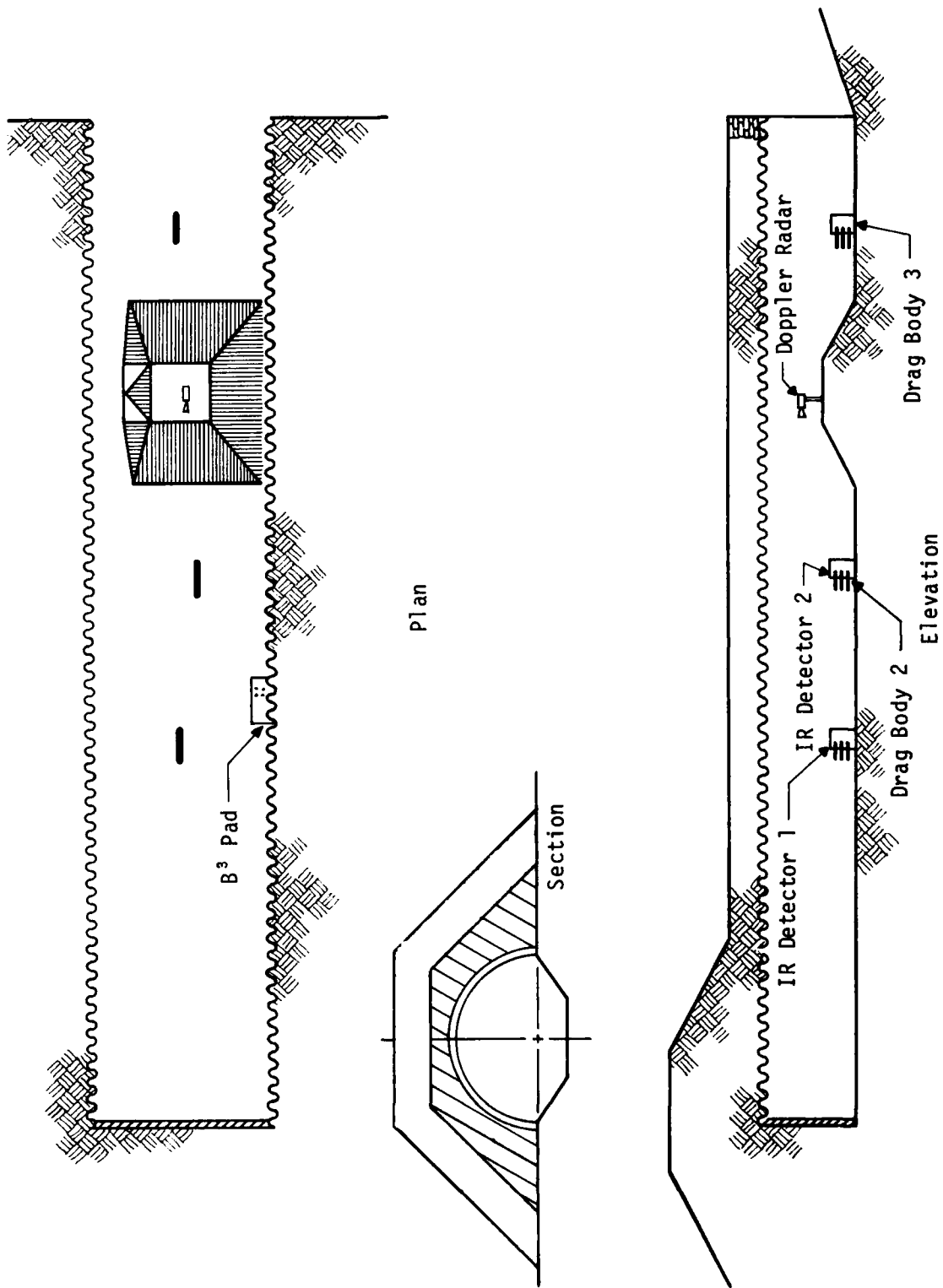


Figure 2. Test-Bed Layout, HH-S2 Event

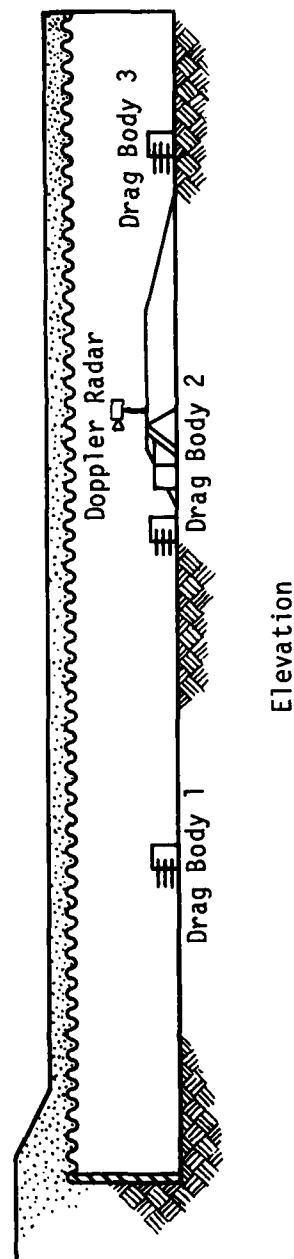
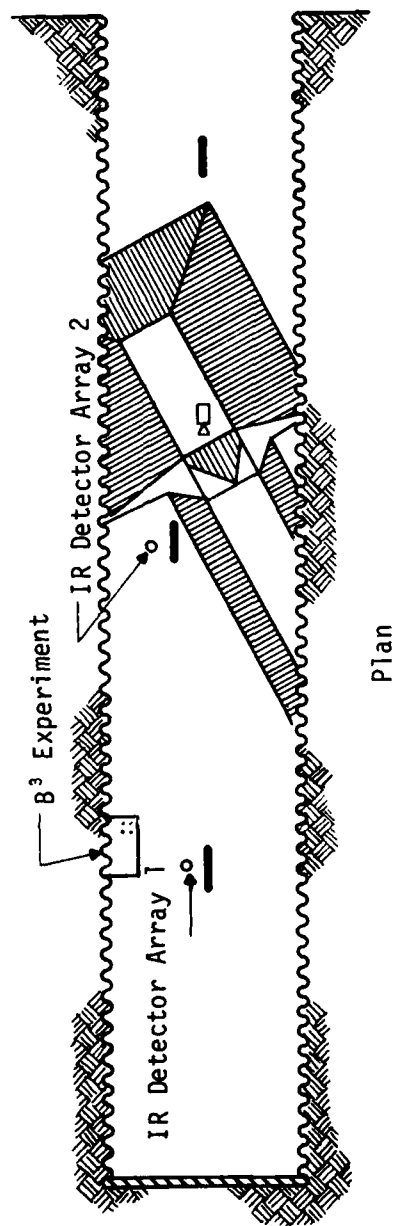
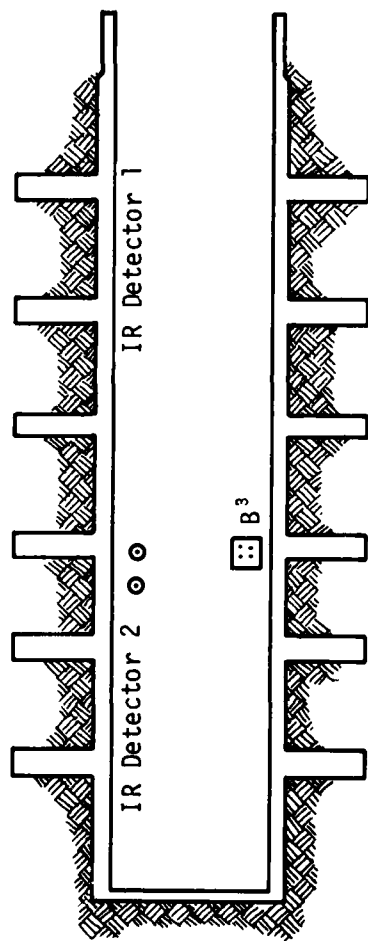
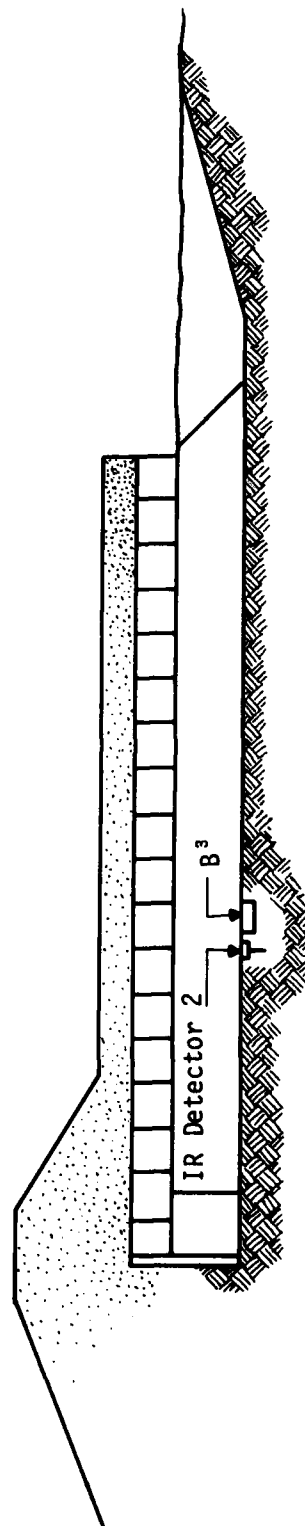


Figure 3. Test-Bed Layout, HH-S3 Event

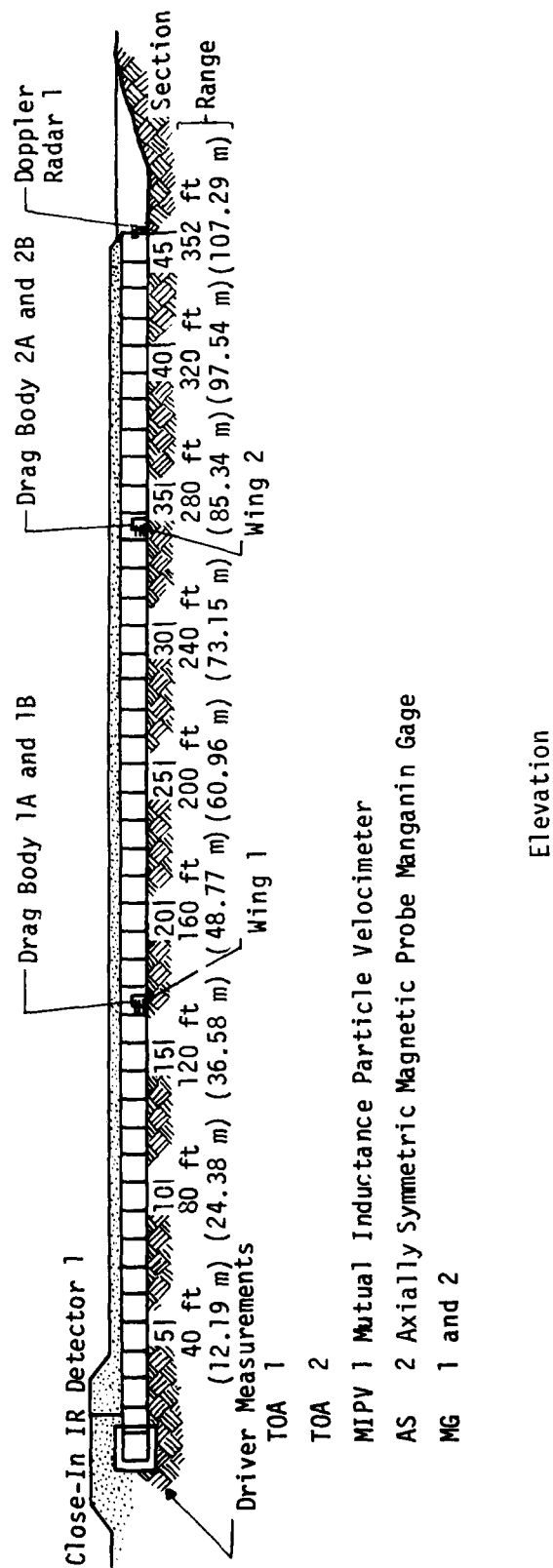


Plan



Elevation

Figure 4. Test-Bed Layout, DSOT-1



SECTION II DOPPLER RADAR

An inexpensive Doppler radar system in the form of a traffic "speed-gun" has been used successfully to measure the velocity of the DPI. The unit as purchased from CMI Inc., of Minturn, Colorado consists of a housing, a circular horn antenna, and a preamplifier circuit board. A digital display and its associated electronics complete the standard unit; however, these are not purchased since they are replaced by a line driver and are tape recorded in the present application. Thus, a relatively sophisticated microwave measurement system is obtained at a cost less than that of a typical blast-pressure gage.

The pertinent specifications for the speed gun as given by the manufacturer are as follows:

Frequency -- $10,525 \pm 25$ MHz

Polarization -- Circular

Beam Width -- 8 deg or less (side lobes suppressed greater than 24 dB down)

Antenna -- 4-in aperture; circular horn type

FR Power -- 20 mW min; 100 mW Max

Receiver Diode -- Shotky barrier type rated for 100 mW burnout

A schematic of the radar unit as used in the HH series is shown in Figure 6. The Shotky diode output (at the Doppler frequency, f_d) is highpass filtered and amplified by the preamplifier; the resulting signal is put into the line-driver amplifier, which in turn drives the signal line to the recording station.

The relationship between the signal (Doppler) frequency and the target velocity is:

$$f_d = \frac{2Vf_r}{c} \quad \text{or} \quad V = \frac{c}{2f_r} f_d \quad (2)$$

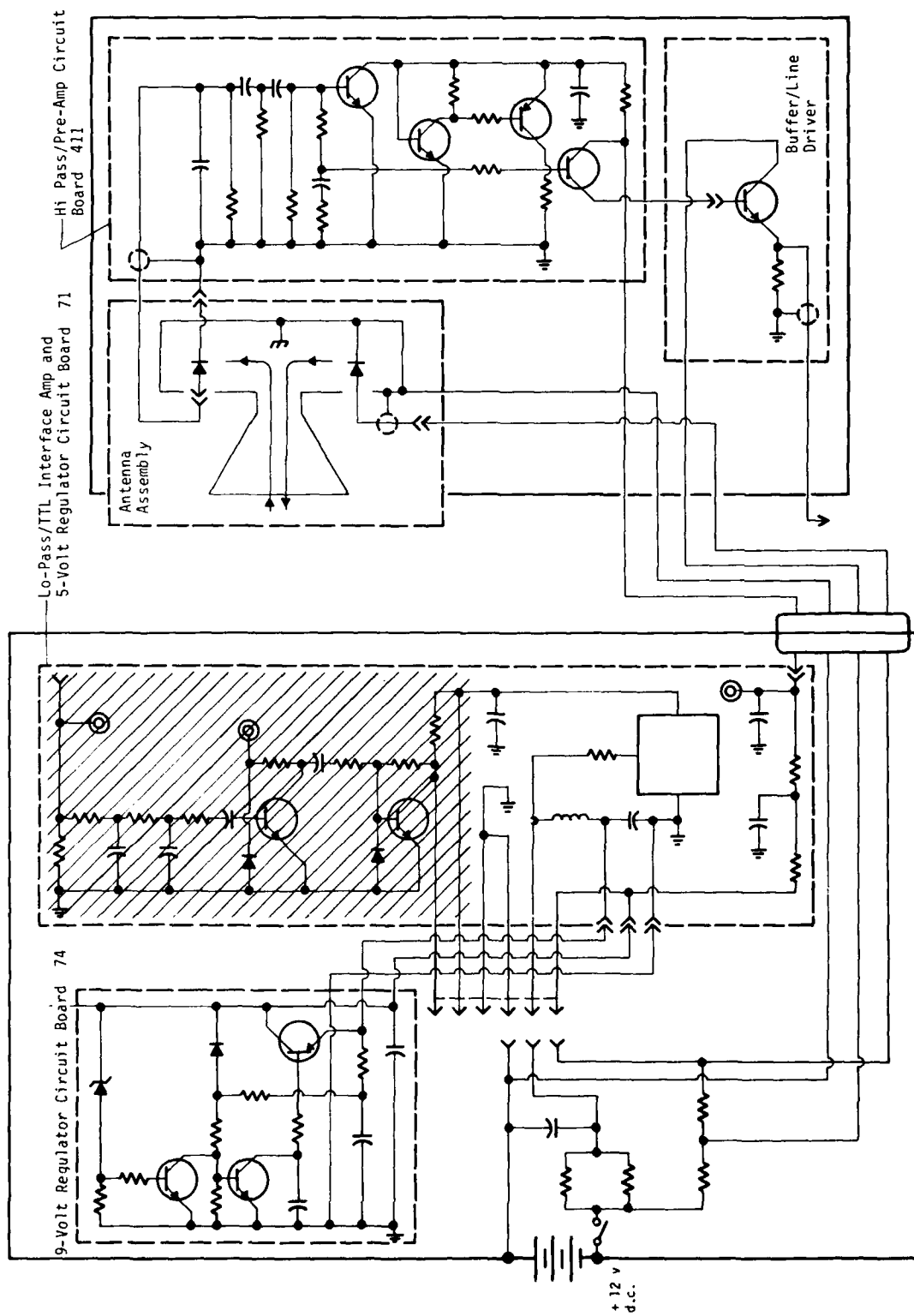


Figure 6. Radar Schematic, HH-S1, S2, and S3.

Where f_d = Doppler frequency
 V = Velocity of target
 f_r = Radar frequency (10,525 MHz)
 c = Velocity of light (3×10^8 m/s)

For target velocity in units of feet per second (ft/s), Equation 2 reduces to:

$$V = 46.76 \times 10^{-3} \text{ ft } f_d$$

The purpose of the Doppler radar measurement in these experiments was to measure the speed of the interface between the clean-air shock and the expanding detonation products driving it. A DABS, as has been previously explained, consists of a high-explosive charge situated at one end of a tunnel. When this charge is detonated, it drives a shock wave down the tunnel. This shock wave is used to load a given structure in a manner similar to the airblast generated by a nuclear device.

The basic problem with this type of simulator is that it is too short (for economic reasons) to obtain the high peak pressures desired. Thus the clean-air portion of the shock is short in distance and consequently short in duration. For this reason it is necessary that the detonation products do a significant portion of the loading on any structure to be tested. Because the thermodynamic properties of these products are not well characterized, the emphasis in this report is on finding the pertinent parameters of the explosive and detonation products.

The first problem to address is the position of the interface between the clean-air shock and the detonation products, i.e., what portion of the shock wave is not the well-characterized clean air? The Doppler radar was used to track the velocity of this interface and, by integrating the difference between it and the velocity of the shock front, to determine the approximate position of the interface.

The problem one has in making this determination is that the microwave beam must pass through a clean, shock-heated body of air and reflect off the interface. The possibility of doing this may seem questionable; but the problem has been addressed in a previous report (Ref. 1) in which it was shown that in

order to obtain a significant reflection from the shock front, free electron densities in the air must approach 3×10^7 electrons/mm³. Air at the pressures encountered in DABS however *does not* have plasma densities of this order of magnitude. The burning interface, on the other hand, *does* and can quite capably reflect the microwave beam.

The other problem, also addressed in the previously mentioned report, is the possible perturbation of the data due to the fact that the beam propagates *through* the shocked air. Equation 2 can be rewritten as follows:

$$V = \frac{d(nx)}{dt} = \frac{c}{2f_r} f_d \quad (3)$$

where x is the propagation distance and n is the effective index of refraction for the 10.5 GHz microwave beam. The problem is that shocked air may change in index in such a way as to perturb the data. This effect, however, was also shown to be negligible.

As can be seen from Table 1, the Doppler radars were fielded on four test events in this series. The data produced agree quite well with other data as illustrated in Figure 14 in the following section. The notable exception was data from HH-S1. This is the only event in which the radar did not function. The reason for this failure was false economy on the part of the authors. If one looks at Figure 6, it can be noted that the power supply was separate from the radar antenna and its preamp and signal line drivers (75 Ω output impedance). The power line connecting the two was at about 197 ft (60 m). This distance was provided to protect the power supply from blast effects. During the morning prior to the test event, the system was working well when checked out just before the experimenters left the test bed. During the ensuing hours, however, the temperature rose in a manner not inconsistent with normal weather patterns in the desert. This rise caused an increase in line resistance, dropping the voltage at the antenna. When this voltage drops to below approximately 8 V d.c., the Gunn diode in the antenna assembly will cease to function and cause a total failure in the device because of the lack of emission of the microwave signal.

In order to prevent this situation, a higher voltage battery was used closer in to the radar on subsequent events (Fig. 7). Figure 8 provides an example of some of the data obtained.

The basic conclusion that one can draw from the data is that the empirical "wags" of shock experimenters are not too bad. In a theoretical sense, as air is adiabatically shocked its density increases asymptotically to

a value defined by
$$\frac{\rho}{\rho_0} = \frac{\gamma+1}{\gamma-1} \quad (4)$$

where ρ_0 is the initial density, and ρ is the final density and γ is the ratio of the isobaric and isovolumetric specific heats. For air, this density ratio maximizes at six to seven. With this as a single datum point, one could infer that the clean-air shock would have a linear propagation distance equal to one-sixth to one-seventh of the total shock propagation distance of the high pressure wave. However, the existence of turbulence at the interface causes the detonation products to diffuse into the clean air shock, shortening this distance. "Shock tubers" have empirically found the actual distance to be approximately one half of the theoretical distance. This is sufficiently borne out by the data to constitute a good rule of thumb.

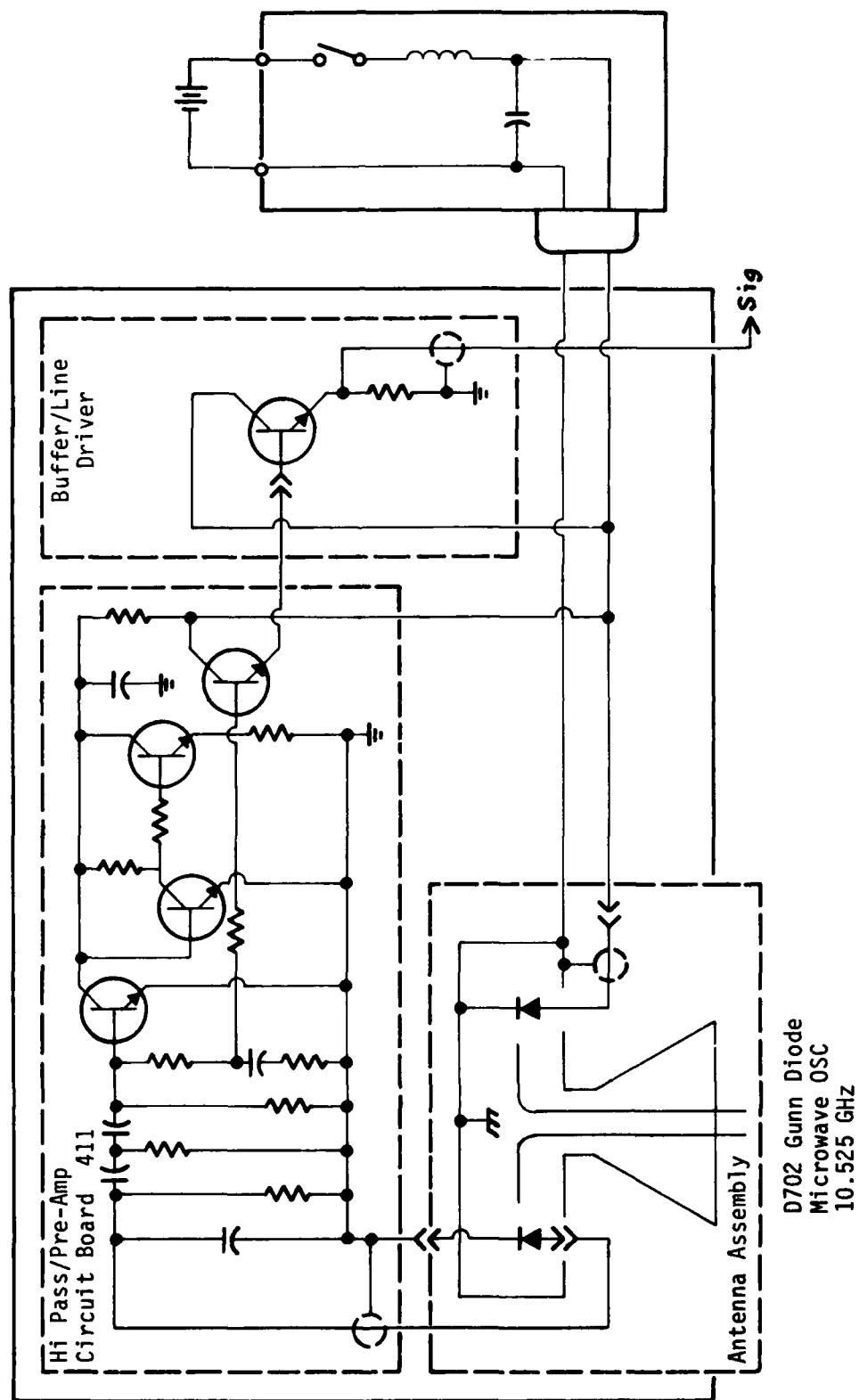


Figure 7. Radar Schematic, HH-T3

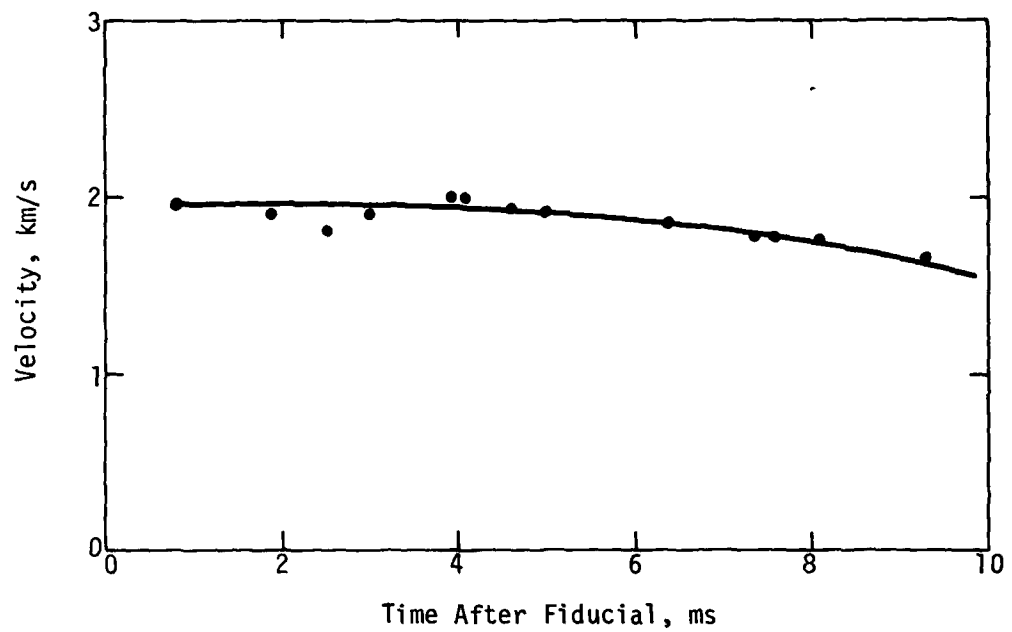


Figure 8. Radar Velocity Data on HH-S2

SECTION III INFRARED (IR) DETECTORS

Experimental results from the DABS-I series gave rise to speculation that the DPI might be radiating as a blackbody. If this were the case, then the temperature could be found by the intensity of the radiation at any given wavelength and calculating the temperature from Planck's blackbody distribution function; viz.,

$$\frac{I(\lambda T)}{\lambda} = \frac{2\pi c^2 h}{\lambda^5 (e^{ch/\lambda kT} - 1)} \quad (5)$$

where

- I = Radiation intensity
- λ = Wavelength
- T = Absolute temperature, K
- c = Speed of light
- h = Planck's constant (6.625×10^{-34} J-s)
- k = Boltzmann's constant (1.38×10^{-23} J-s)

Figure 9 shows a plot of this function for several different temperatures.

In order to test the blackbody DPI hypothesis, a simultaneous measurement of the intensities at three different wavelengths was attempted. As shown in Figure 9, the blackbody nature of the DPI would be verified if the three intensities were related to each other to fall on any curve obeying Equation 5; and the curve so described would uniquely define the temperature. The measurement was made with three identical lead selenide photosensitive infrared (IR) detectors, each covered with a narrow bandpass filter at the indicated wavelength.

The intensity of the radiation passed through each filter is given by

$$I_{\lambda T \tau} = \tau_{\lambda} \frac{I_0(\lambda, T)}{\lambda} \Delta\lambda \quad (6)$$

where

- $I_0(\lambda, T)$ = Intensity of radiation, W/cm²
- τ_{λ} = Transmission coefficient of filter at wavelength λ
- λ = Center wavelength of filter, μm
- $\Delta\lambda$ = Half amplitude bandpass of filter, μm

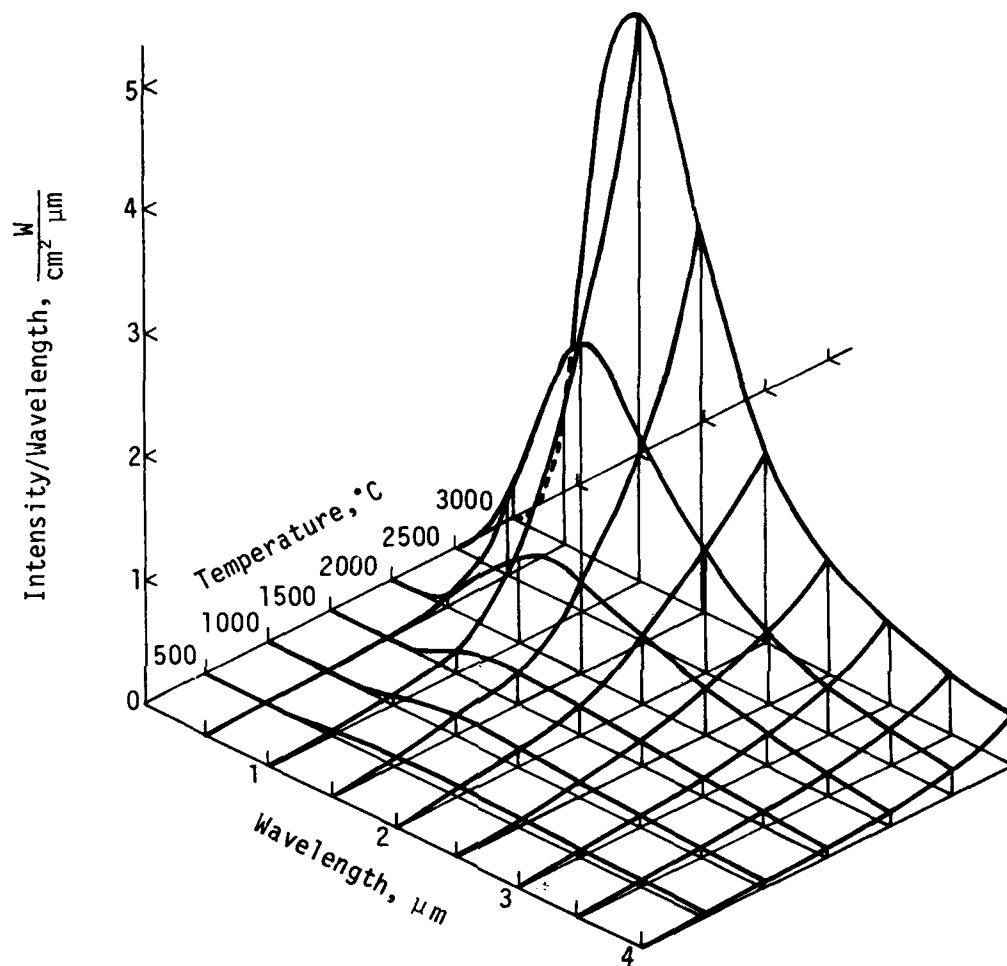


Figure 9. Intensity Versus Wavelength and Temperature - Blackbody Radiation

The transmission curves for the three filters used in the three-color IR detector are shown in Figures 10a, b, and c. The wavelengths of 1.076, 2.227 and 3.994 μm were chosen for the following reasons: (1) these values were readily available; (2) they are positioned in the spectrum to give one point near the maximum of most of the likely temperature curves, one near the half point and one in the 5-to-15 percent region; and (3) they are not located at any of the well-known emission lines for the principal constituent elements in the DPI.

The intensities at the three chosen wavelengths for various temperatures are given in Table 2. Graphs of the intensity of the filtered radiation as a function of temperature for the three bandpass wavelengths are given in Figure 11. If the DPI is in fact radiating as a blackbody, then the measured intensities at the three wavelengths should fall on an abscissa (Fig. 11), the value of which will be the temperature of the DPI.

One further complication in the measurement scheme arises from the fact that the response of the photoresistor depends upon the wavelength as shown in Figure 12a and upon the frequency of the variation of radiation intensity as shown in Figure 12b. This problem was solved by calibrating the detectors (with the filters in place) against a blackbody reference prior to use in the field.

Development of the IR-detector measurement scheme under Phase I was limited to recording the response of an uncalibrated detector to the shock arrival and DPI arrival. Data from this effort, when compared with crystal pin time-of-arrival (TOA) data and Doppler radar data from the same test, indicate that the shock arrival is readily distinguished from the DPI arrival and does in fact lag the shock arrival as expected. The correlation between shock velocity from crystal-pin TOA data, DPI velocity from Doppler-radar data, and DPI velocity from IR-detector data is shown in Figure 13.

The IR detectors fielded on HH-S1 were, like those used during Phase I, simple, uncalibrated photoresistors without filters. The detector package was installed in the top of the wing and protected with a quartz window as shown in Figure 14. The close-coupled electronics were unchanged from DABS-IE. The complete wiring diagram of the HH-S1 setup is shown in Figure 15.

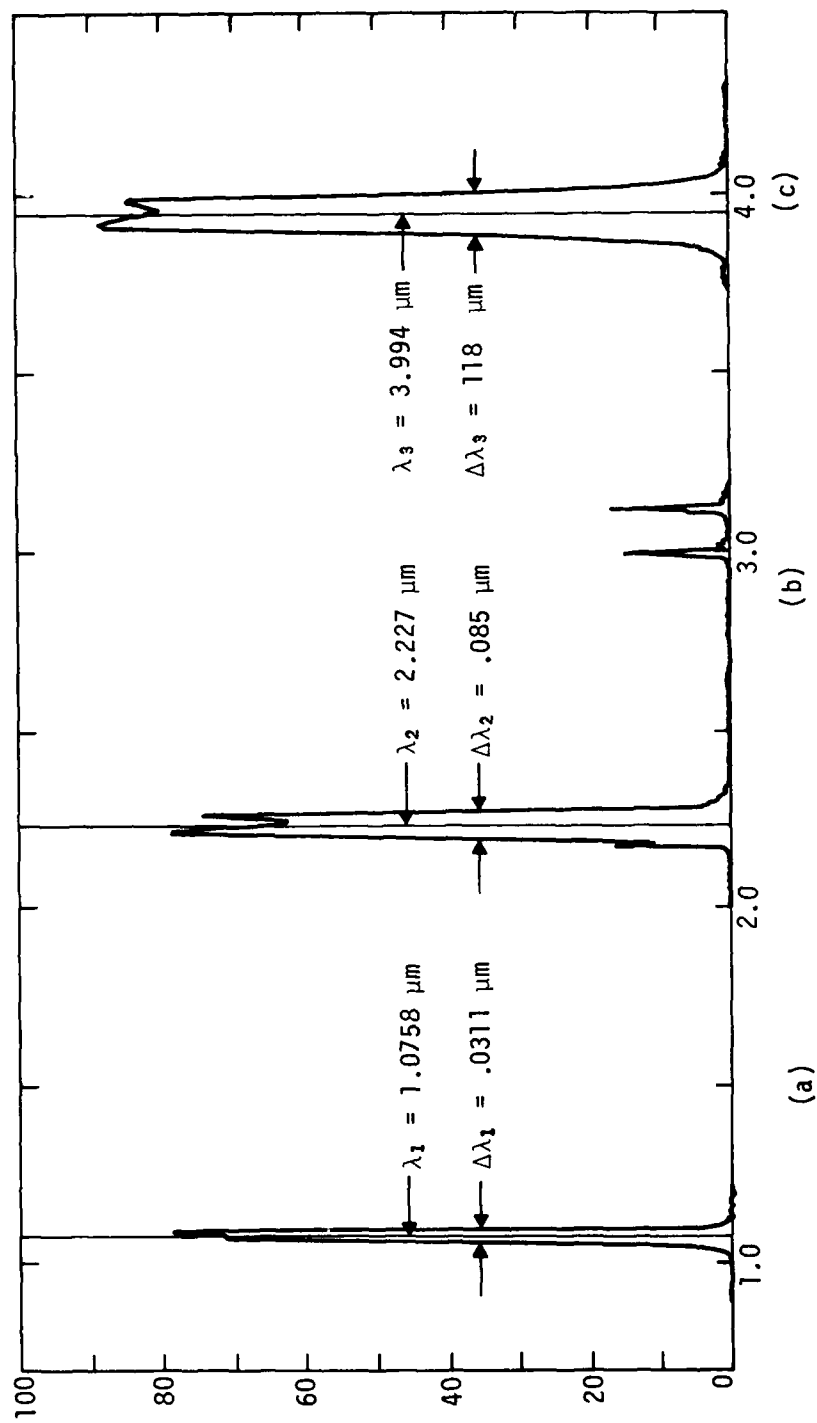


Figure 10. Transmission Curves for Filters

TABLE 2. INTENSITIES OF FILTERED BLACKBODY RADIATION

λ	T	$\frac{I(\lambda, \tau)}{\lambda}$	$\Delta\lambda$	τ	$I_{\lambda, T}$
(μm)	($^{\circ}\text{C}$)	($\frac{\text{W}}{\text{cm}^2 \mu\text{m}}$)	(μm)	(percentage)	($\frac{\text{mW}}{\text{cm}^2}$)
1.0758 2.227 3.994	1500	.1370 .1832 .0556	.0311 .085 .118	73 70 82.5	3.1 10.9 5.4
1.0758 2.227 3.994		.7229 .4227 .0950	.0311 .085 .118	73 70 82.5	16.4 25.1 9.2
1.0758 2.227 3.994		2.1014 .7364 .1382	.0311 .085 .118	73 70 82.5	47.70 43.81 13.45
1.0758 2.227 3.994	3000	4.4320 1.1022 .1837	.0311 .085 .118	73 70 82.5	100.6 65.58 17.88
1.0758 2.227 3.994		7.7148 1.5046 .2306	.0311 .085 .118	73 70 82.5	175.1 89.53 22.44
1.0758 2.227 3.994		11.865 1.9331 .2784	.0311 .085 .118	73 70 82.5	269.4 115.0 27.1
1.0758 2.227 3.994	4500	16.771 2.381 .327	.0311 .085 .118	73 70 82.5	380.8 141.6
1.0758 2.227 3.994		22.318 2.842 .376	.0311 .085 .118	73 70 82.5	506.7 169.1 36.6

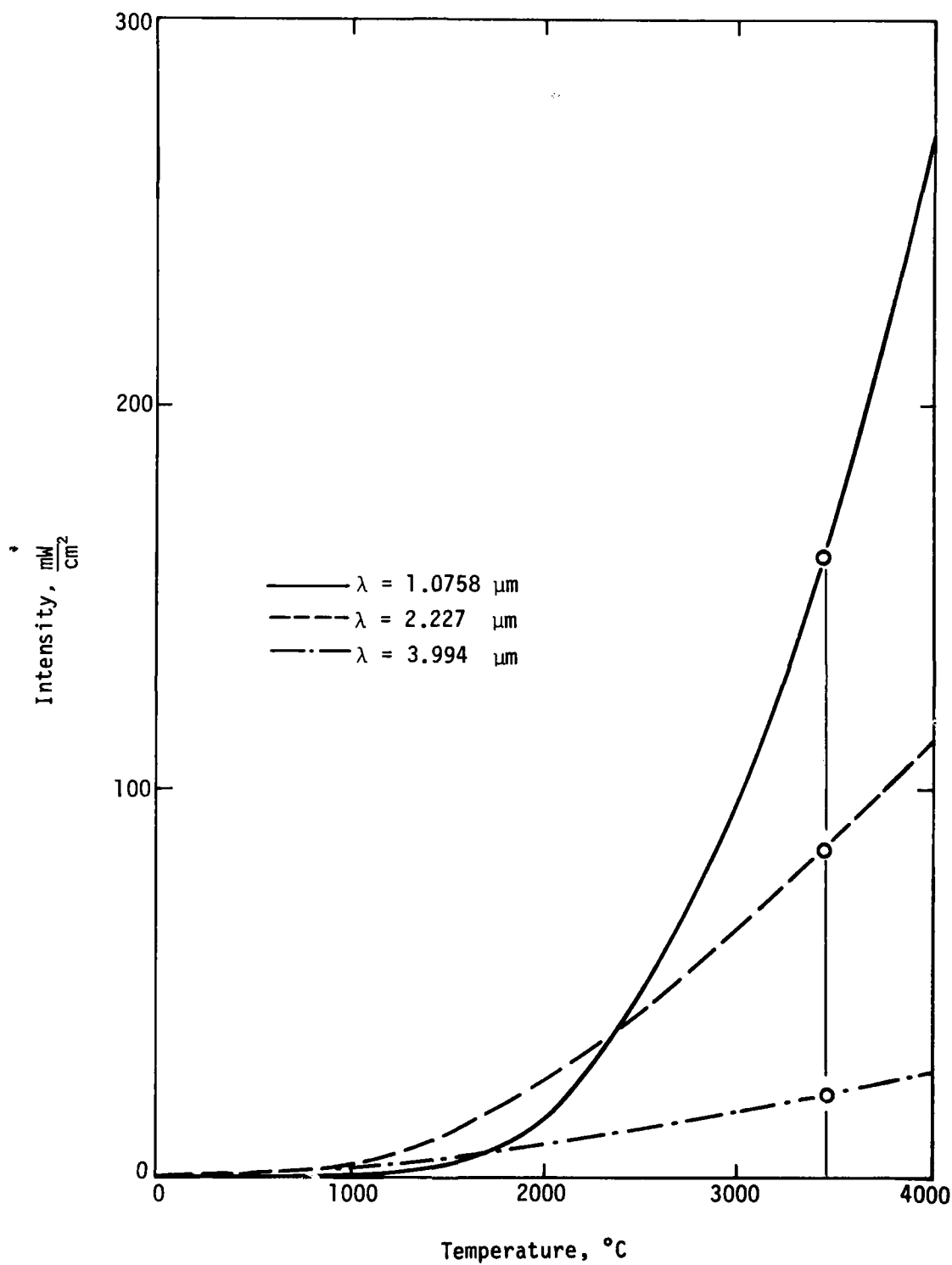
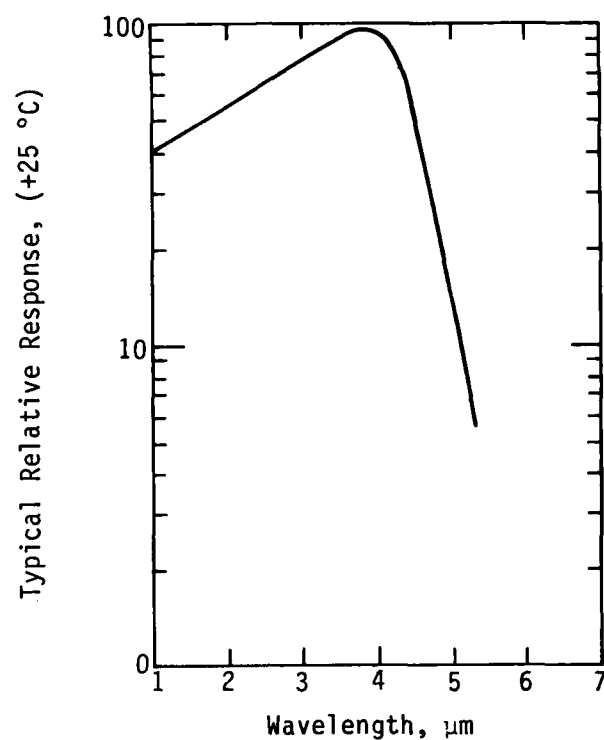
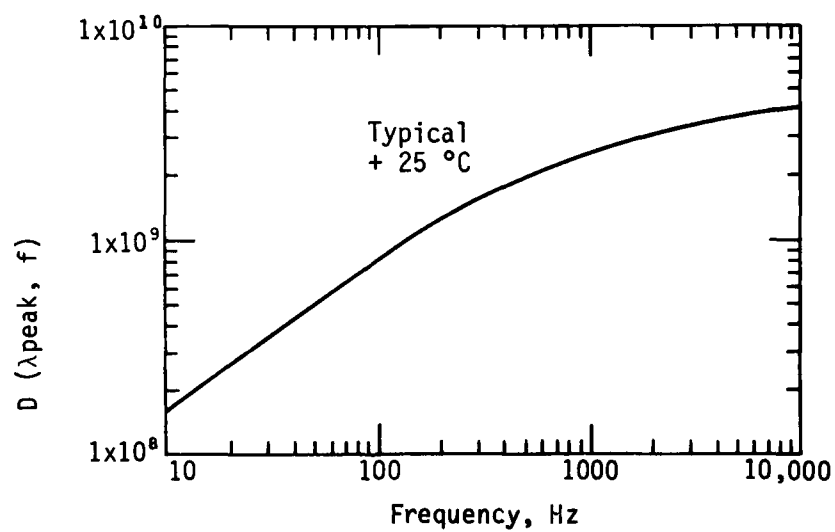


Figure 11. Intensity-Versus-Temperature Filtered Blackbody Radiation



(a) Response as a Function of Wavelength



(b) Response as a Function of Frequency

Figure 12. Sensitivity of Lead Selenide Photoresistors

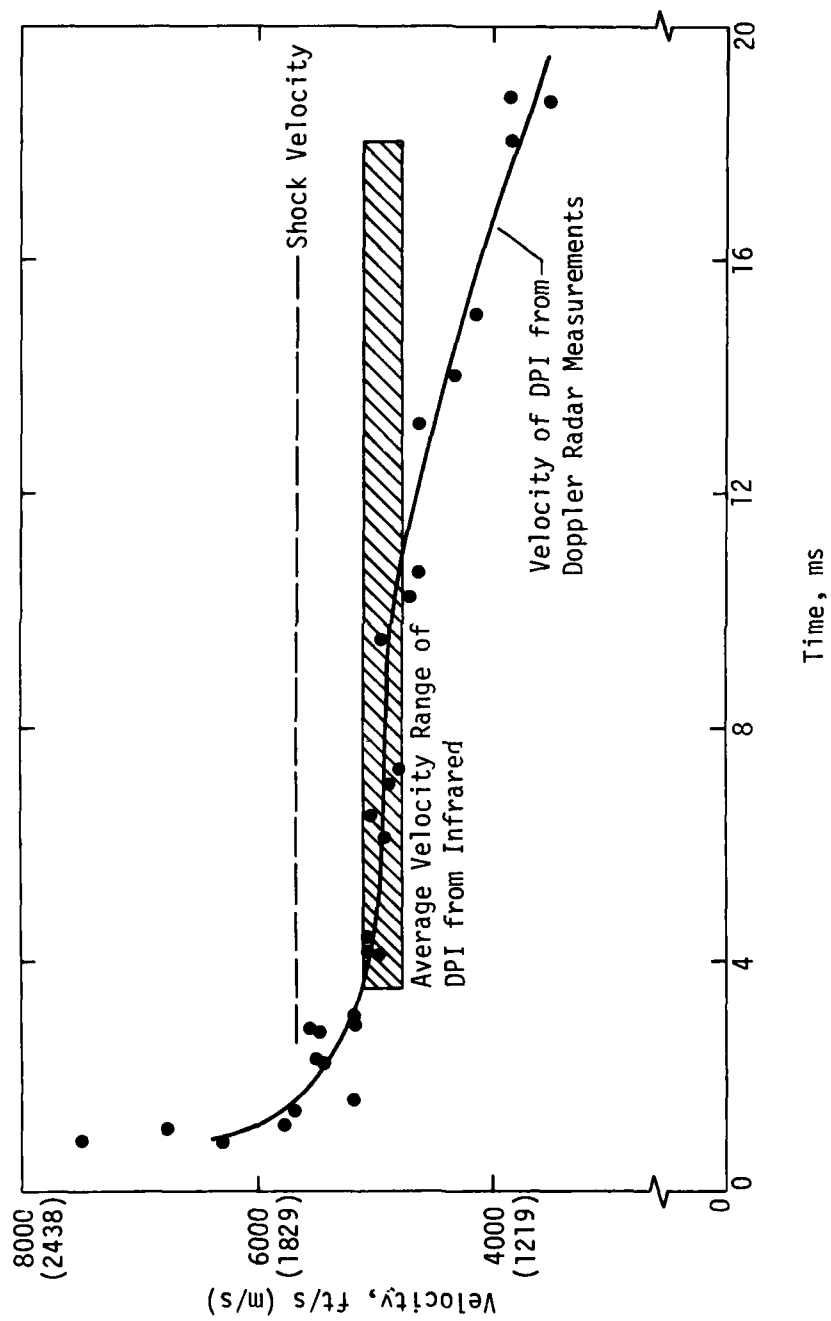


Figure 13. Comparison of Infrared Data with TOA Crystal and Doppler Radar Data

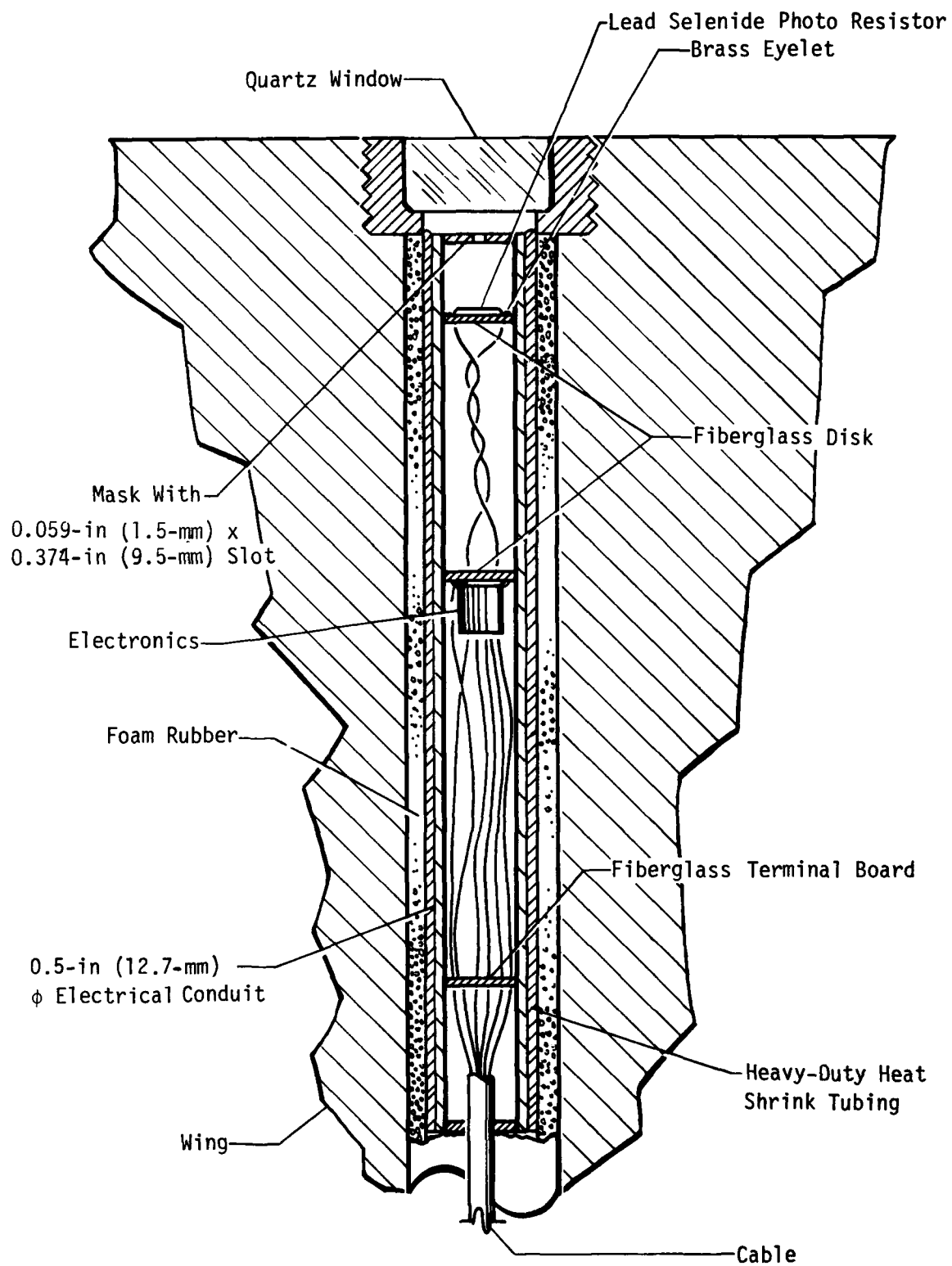


Figure 14. Infrared (IR) Detector, HH-S1

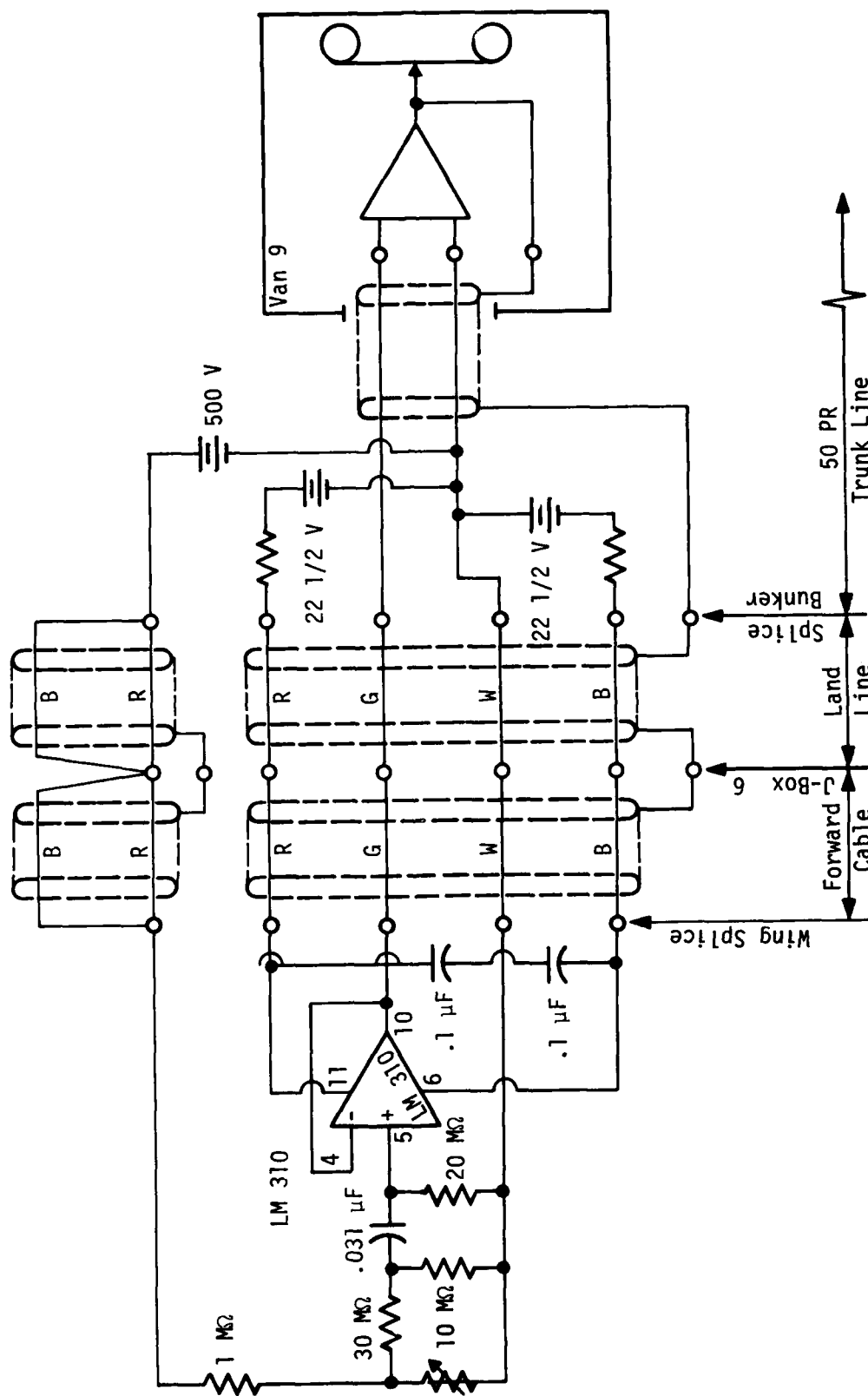


Figure 15. IR Detector Instrumentation, HH-S1

The IR detectors fielded on HH-S2 were also uncalibrated and without filters, but a different package and close-coupled electronics circuits were used. The objective was to d.c.-couple the detector signal to the recording electronics, which necessitated elimination of the d.c. offset at the input to the close-coupled amplifier. This adjustment was accomplished with the bridge circuit shown in Figure 16. In this configuration, the detector package (Fig. 17a) was located in the wing receptacle, but the electronics package was located in the wing-splice pocket. The balance potentiometer was located in the splice bunker in order that the bridge could be balanced without getting into the wing. It was necessary to use a differential amplifier in the recording van to isolate the low sides of the signals from the two detectors. The amplifier used was part of the AFWL mini-conditioner 200 circuit, an AD 521 instrumentation amplifier. Two existing mini-conditioner 200-circuit boards were modified for this purpose.

Because of late delivery, only one quartz window, left over from HH-S1, was available for HH-S2. The window was installed over the detector in Wing 1. A steel plug with a 0.150-in (3.8-mm) diameter hole in it (Fig. 17b) was installed over the detector in Wing 2. It was hoped that the small hole would allow the detector to survive shock arrival and access DPI response data.

The data obtained from the IR detectors on HH-S2 are shown in Figure 18. The output signal came up significantly just after detonation (about +0.75 ms) and increased steadily until the DPI reached the location of the detector (about +8.5 ms). This indicates that the detector in Wing 1 responded to the presumably high levels of light being reflected from the arch ribs. Note that shock arrival (6.3 ms from crystal pin data) did not affect the detector because it was protected by the quartz window. The data indicate that the DPI was 2.25 ms behind the shock front. On the other hand, the detector in Wing 2 for unknown reasons produced a negative output shortly after detonation. The output then gradually rose as the DPI neared the detector. Unfortunately, the detector failed shortly after shock arrival and did not record the arrival of the DPI. It was therefore reaffirmed that the detector must be protected from the shock.

The IR detectors fielded on HH-S3 were three-color units in enclosures in the floor of the DABS as shown in Figure 19. This configuration utilized

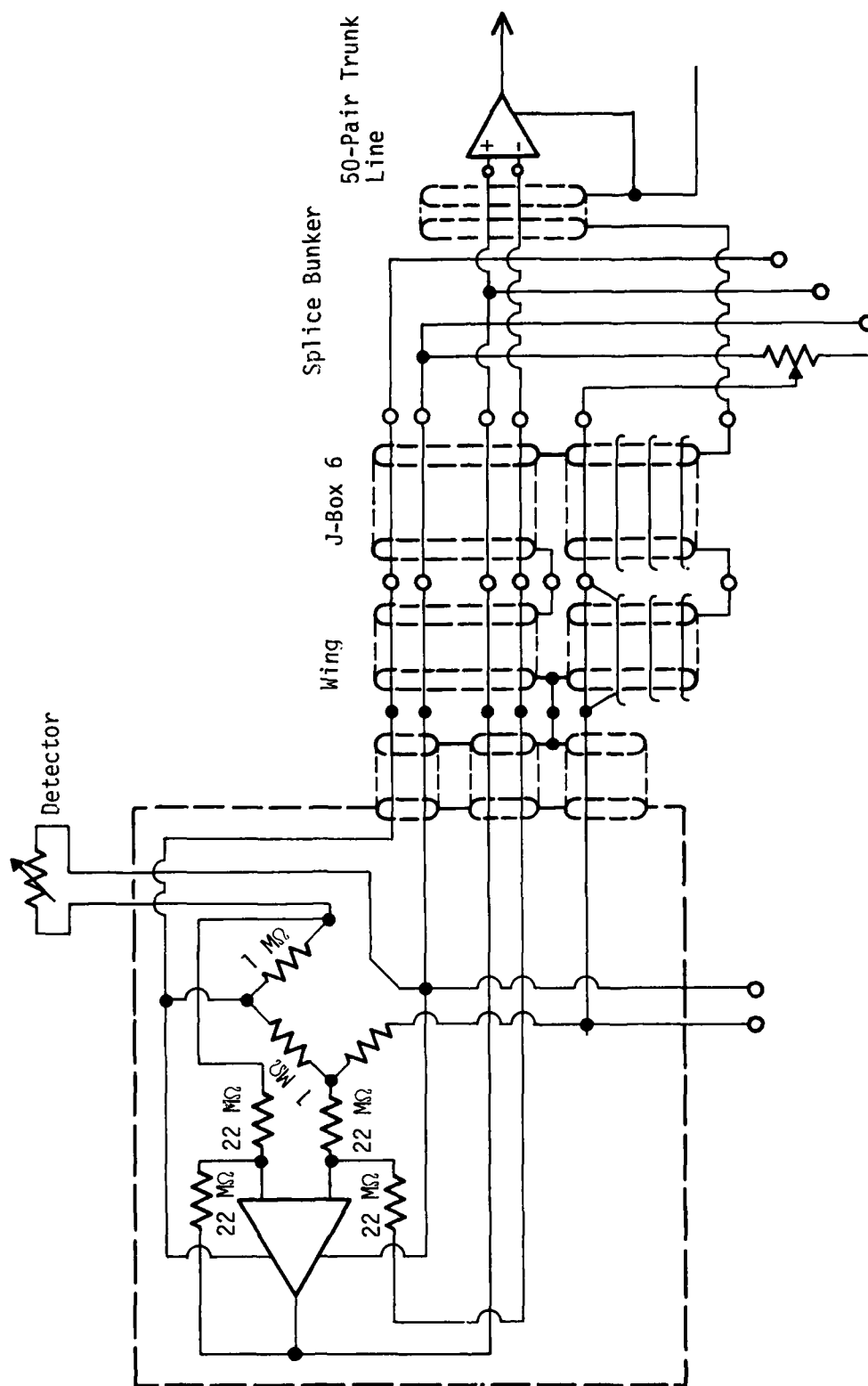
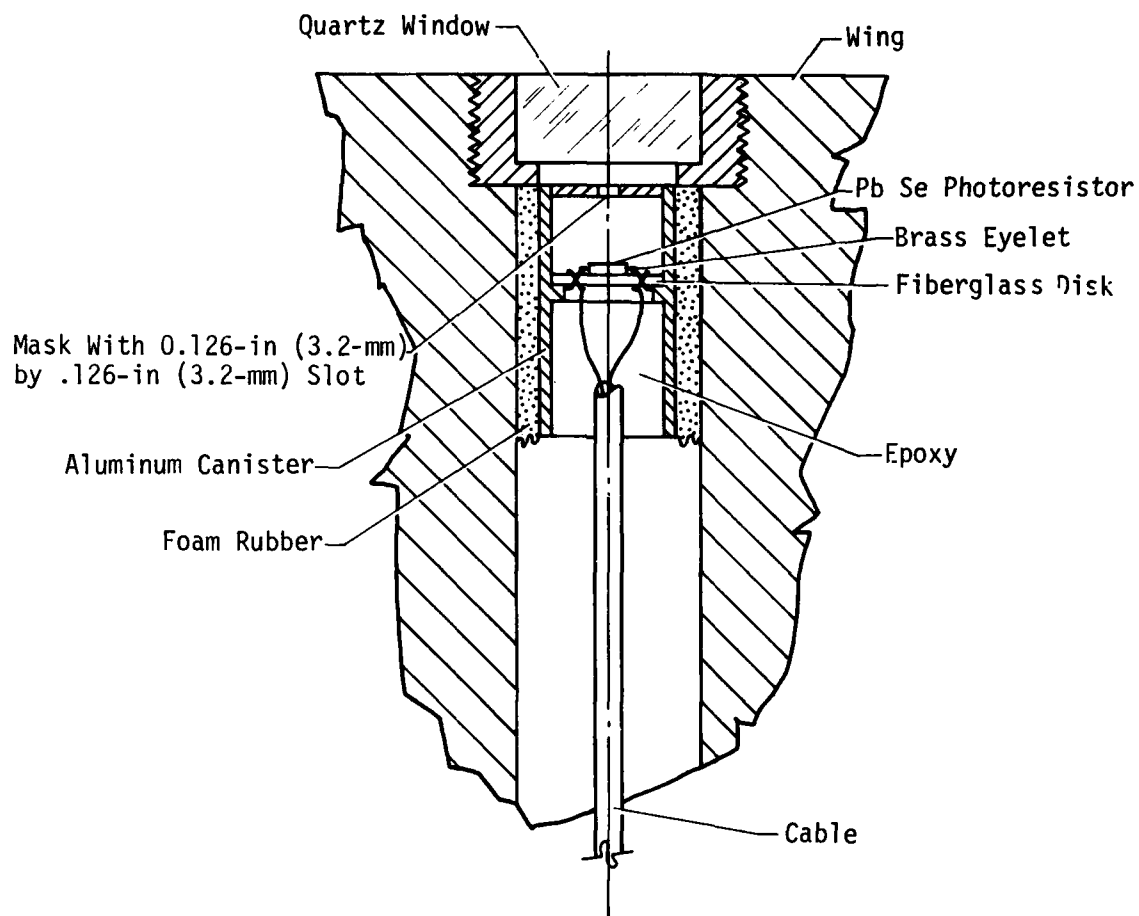
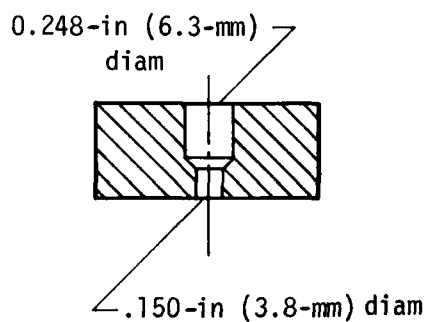


Figure 16. IR Detector Connections, HH-S2



Dia

a) Forward Wing (1) Installation



b) Steel Plug Used in Aft (2) Wing

Figure 17. IR Detector, HH-S2

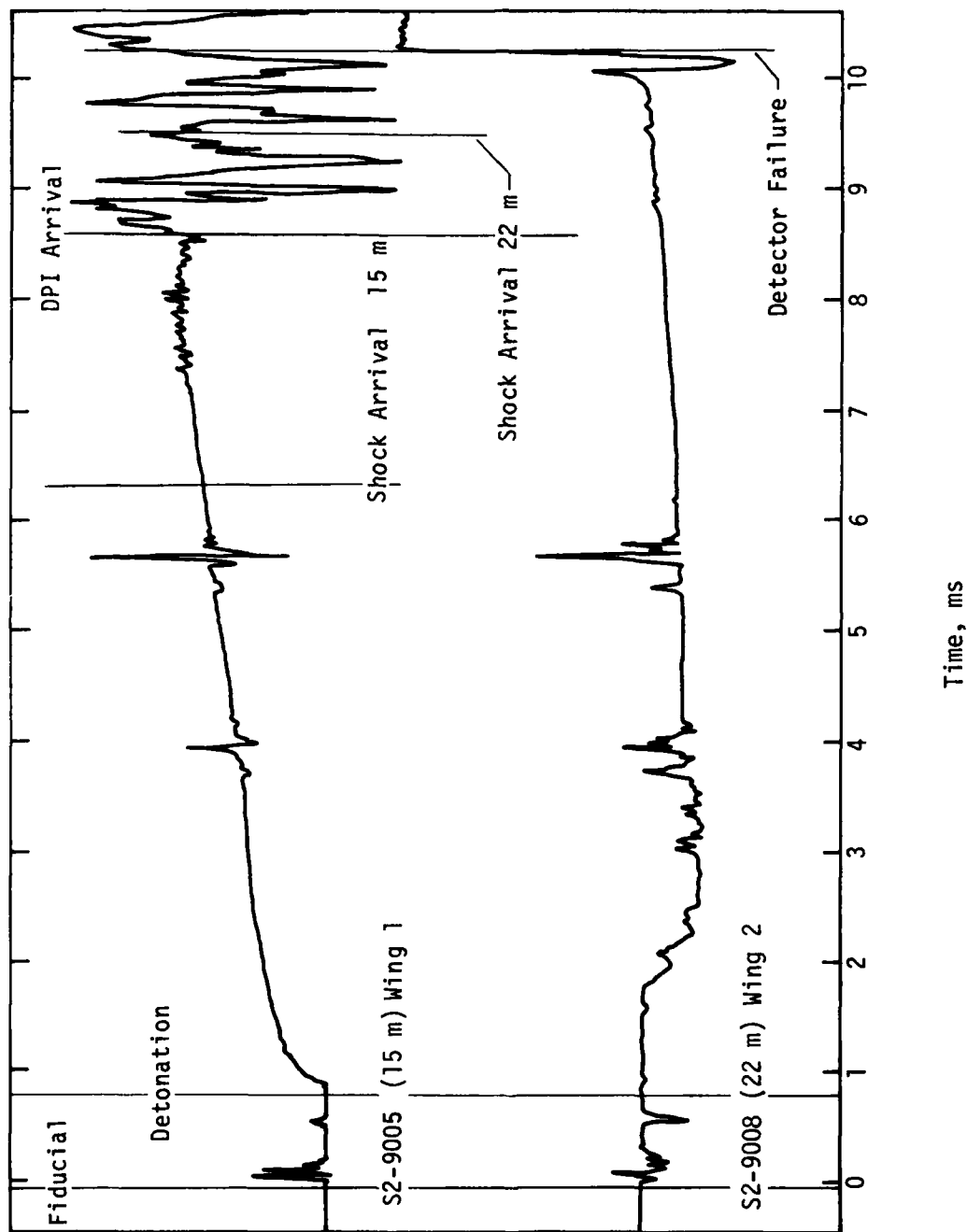


Figure 18. Data from IR Detectors, HH-S2

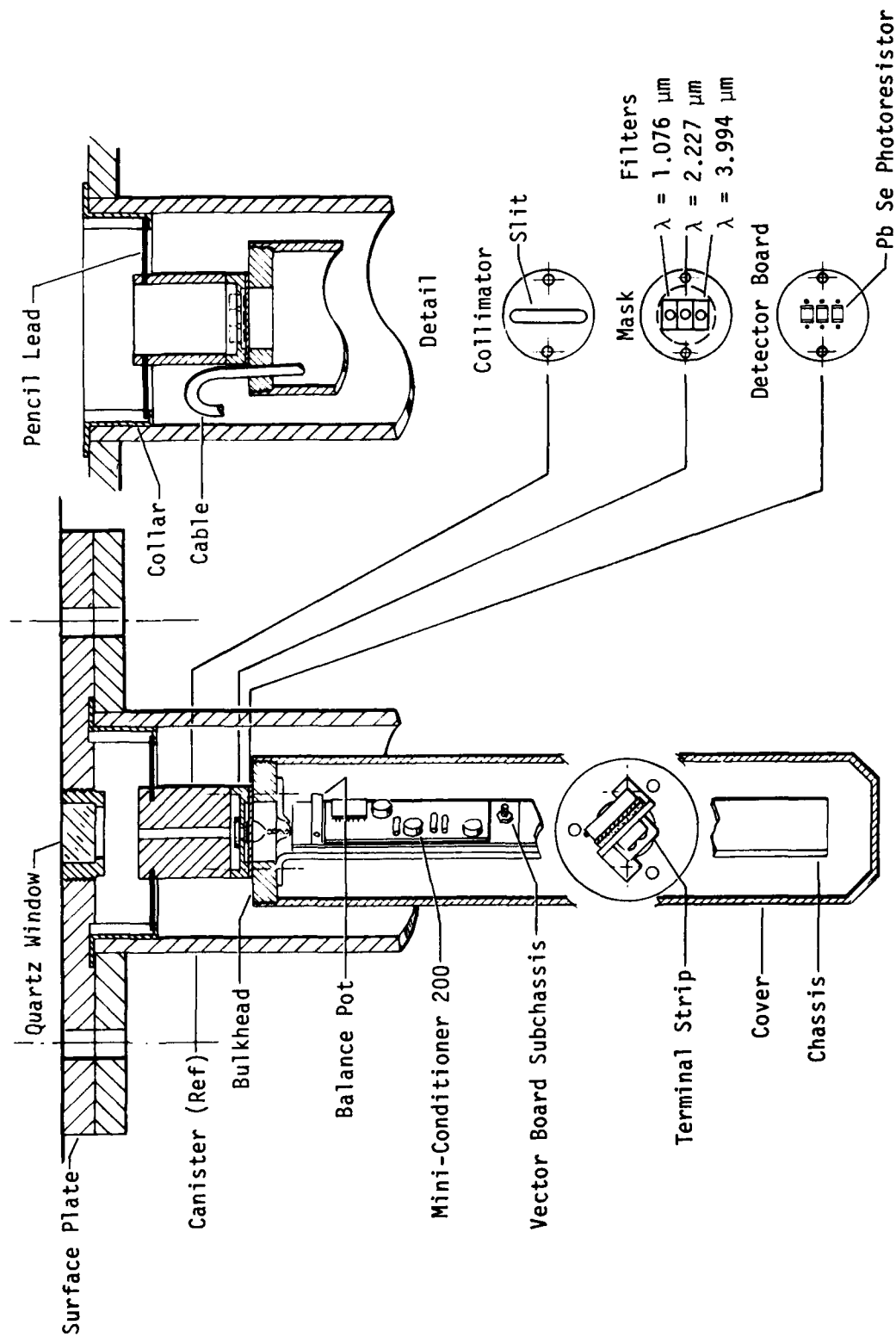


Figure 19. Three-Color IR Detector, HH-S3

the AFWL mini-conditioner 200 close-coupled amplifier. The circuit is shown in Figure 20. The photoresistors, filters, and signal conditioners are all housed in a canister, suspended on pencil leads. This arrangement isolates the detector package from shock during the data window.

The a.c. coupling produced by the capacitors in the recording van was a last resort employed in an attempt to overcome a serious d.c.-drift problem associated with the mini-conditioners. The drift may have been the consequence of the extremely high impedance of the bridge or of a problem with the amplifiers. In any event, it was excessive since it was of the same order of magnitude as the expected signal.

The detector units were calibrated by exposing the assembled units, with filters and quartz windows in place, to a laboratory blackbody at 1500, 2000, and 2500 °C, and to an M-3 flashbulb whose color temperature was 3527 °C. The blackbody was a 0.75-in diameter by 6-in long carbon rod which was heated by passing direct current through it. Since the aperture of the quartz window mount has a diameter of 0.875 in, it was necessary to correct the value of the intensity. If it is recalled that the collimating slit is 0.1875 in wide x 1.25 in long, the irradiated area which the detector array sees is

$$A_0 = 0.875 \text{ in} \times 0.1875 \text{ in} \times (2.54 \text{ cm/in})^2 = 1.06 \text{ cm}^2 \quad (7)$$

The area irradiated by the blackbody is

$$A_i = 0.75 \text{ in} \times 0.1875 \text{ in} \times (2.54 \text{ cm/in})^2 \quad (8)$$

The effective intensity seen by the detectors is then

$$I_{\text{eff}} = \frac{P}{A_0} = \frac{I_i A_i}{A_0} = \frac{1.06}{0.91} I_i = 0.86 I_i \quad (9)$$

Since the flashbulb was used with a reflector, the whole slit was irradiated as it would be in the field. Therefore, no correction is needed for flashbulb or field data.

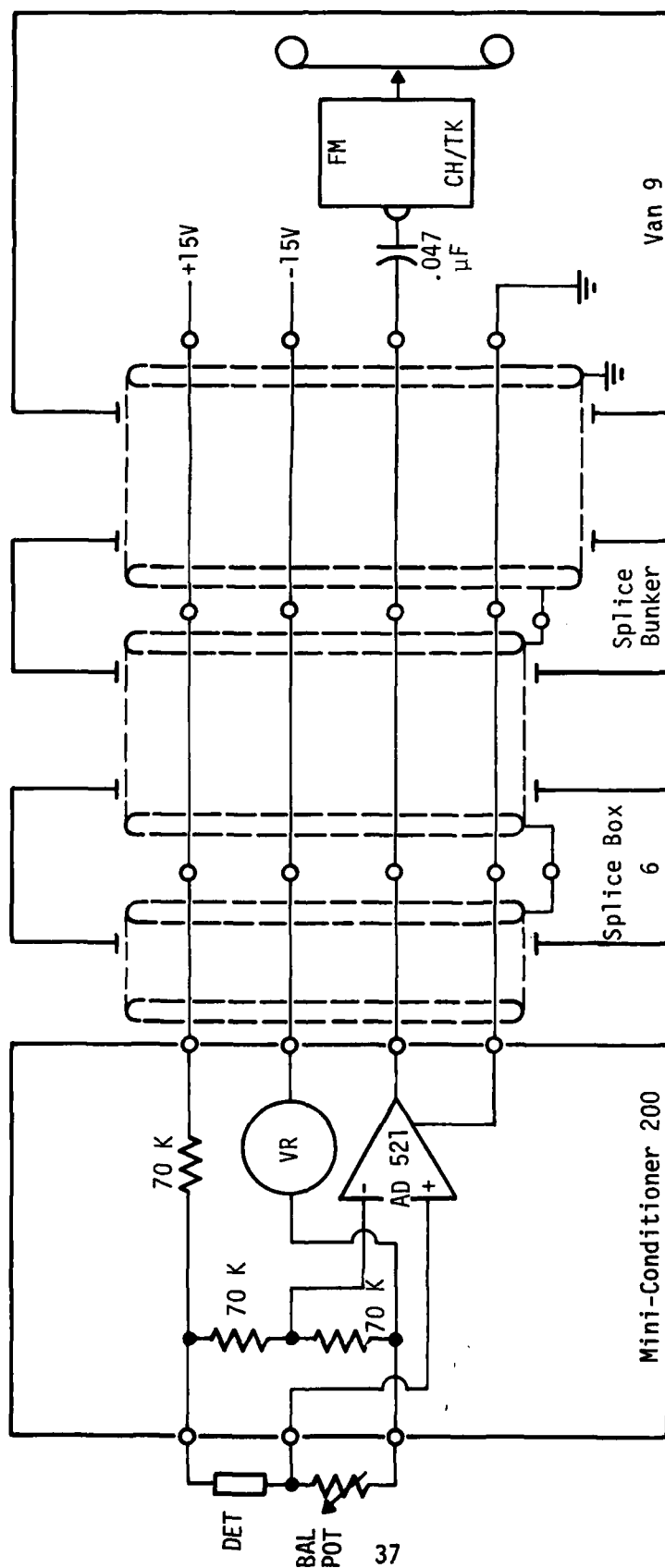


Figure 20. Wiring Diagram, IR Detectors, HH-S3

Temperatures, radiation intensities, and voltage outputs for the two detectors are related as shown in Figures 21 and 22.

The data obtained from the closest detector location (Unit 1, $X = 15.2$ m) are shown in Figure 23. Note that the DPI, indicated by the peak output, lagged behind the shock front by about 0.5 ms. The peak detector outputs were plotted on the detector calibration chart to give intensities and temperatures as shown in Figure 24. At this point in the flow, the DPI did not appear to be radiating as a true blackbody since the indicated temperatures do not coincide for the three wavelengths. A plot of intensity-versus-wavelength, obtained by reversing the process which generated Figure 24, is shown in Figure 25, along with the Planck curves (for comparison) for blackbodies at 3350 and 4500 °C.

It is possible that the higher intensities measured at 2.227 and 3.994 μm indicate a shift of the energy content of the DPI spectrum to higher wavelengths. It is more likely, however, that unknown emission lines, excited at this temperature, cause local increases in the intensity. The temperature of the DPI at this station is probably between 3350 and 4500 °C.

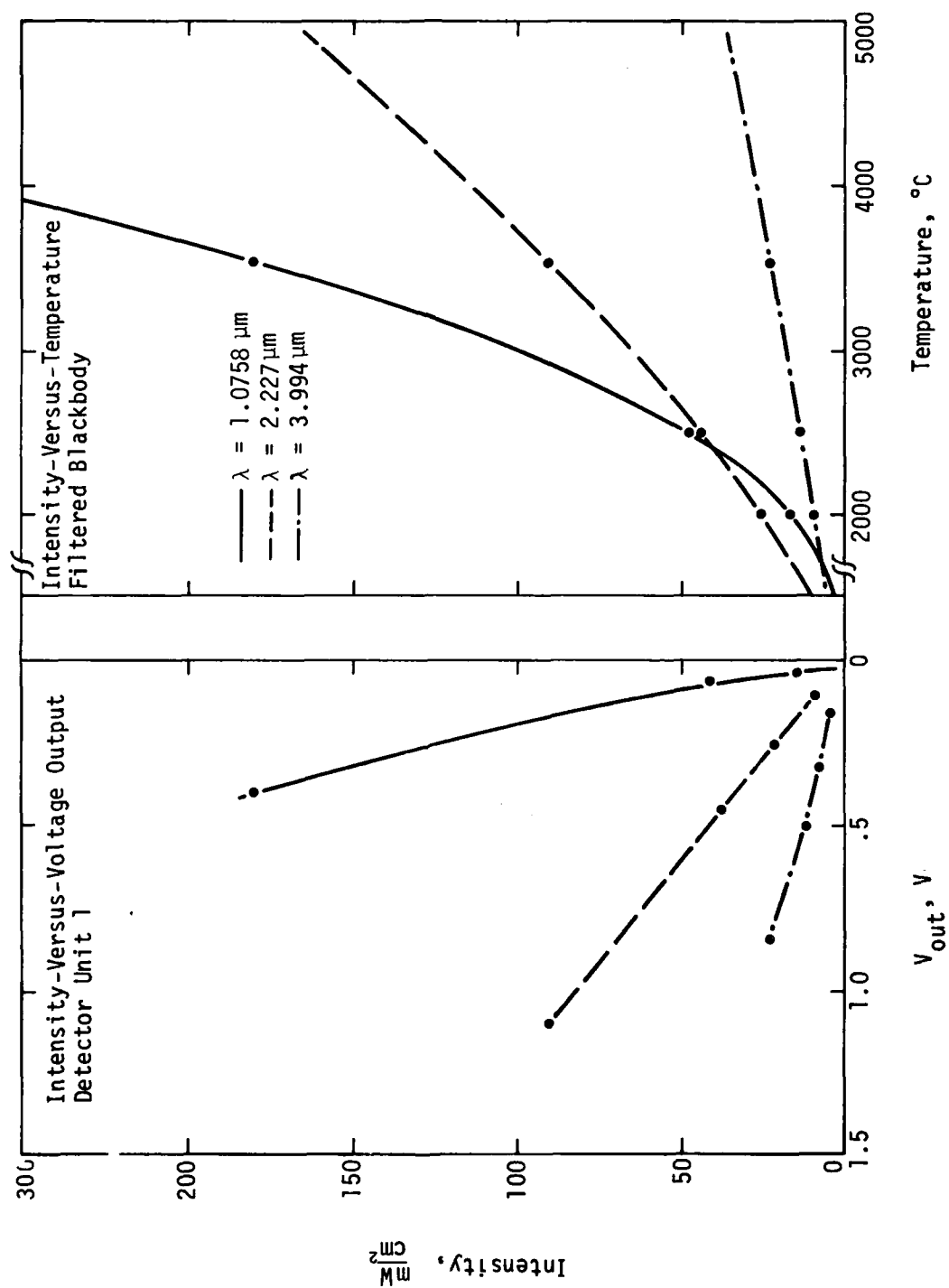


Figure 21. Calibration of Three-Color IR Detector Unit 1, HH-S3

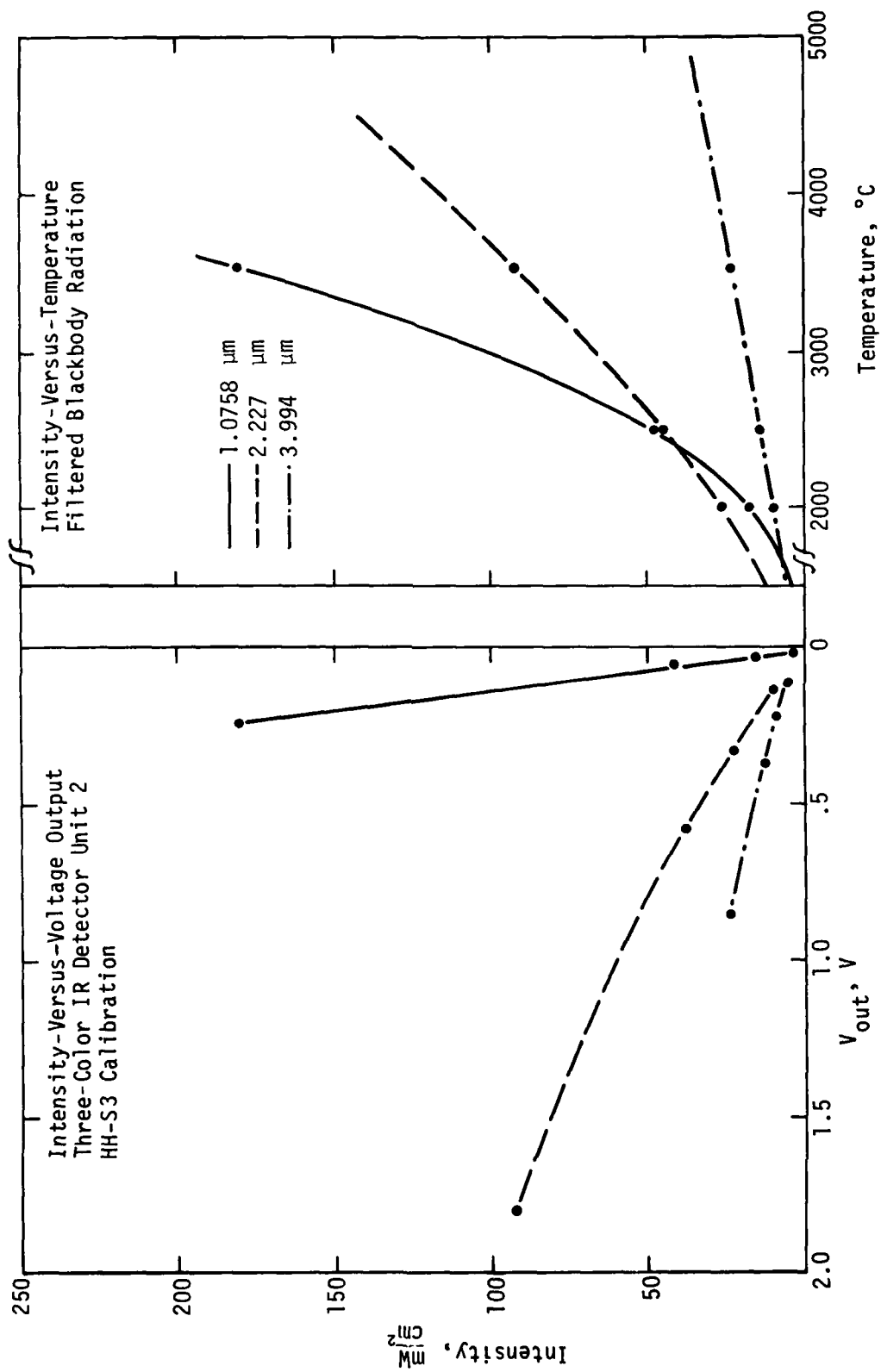


Figure 22. Calibration of Three-Color IR Detector Unit 2, HH-S3

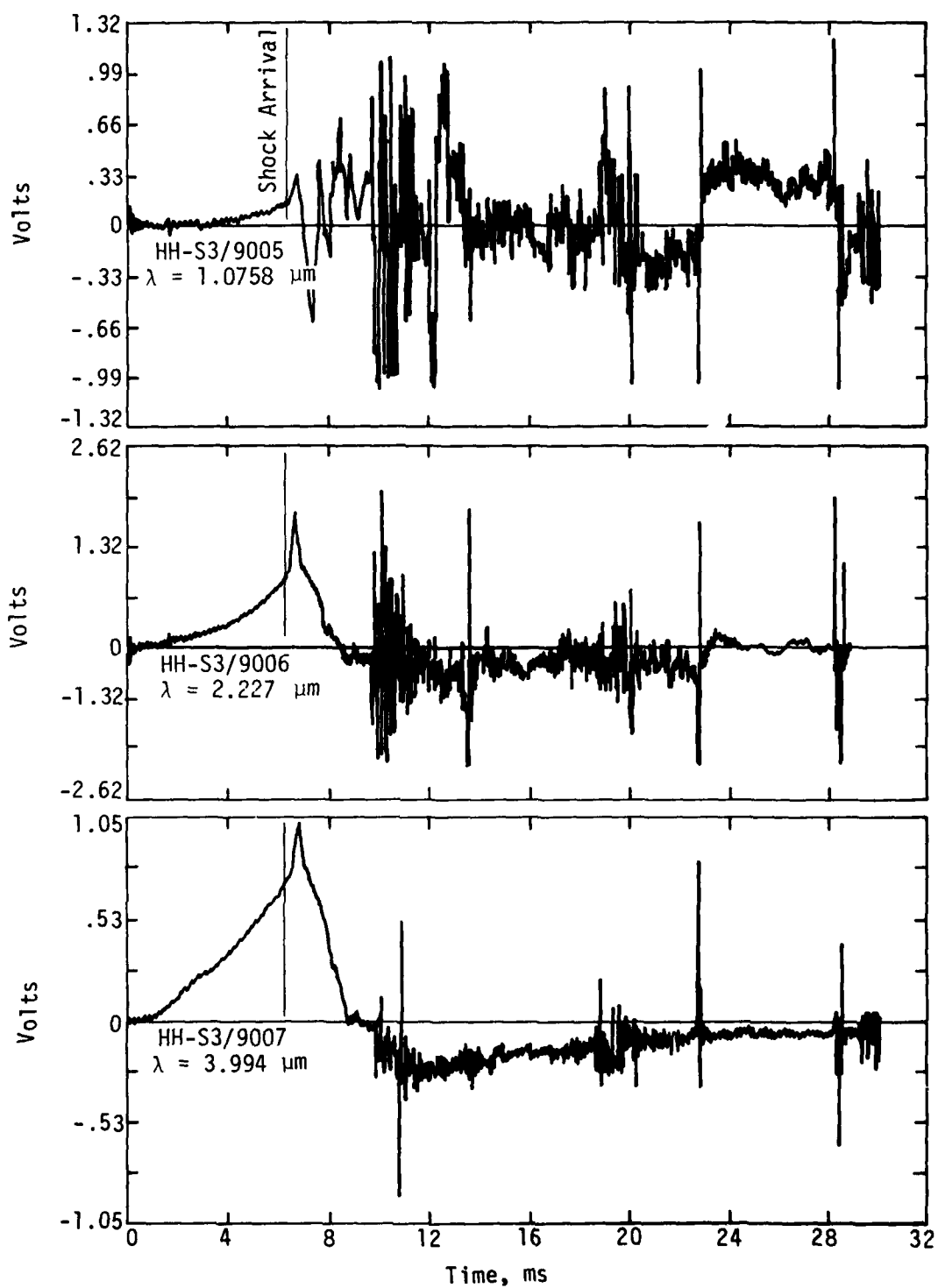


Figure 23. Data from IR Detector Unit 1, HH-S3

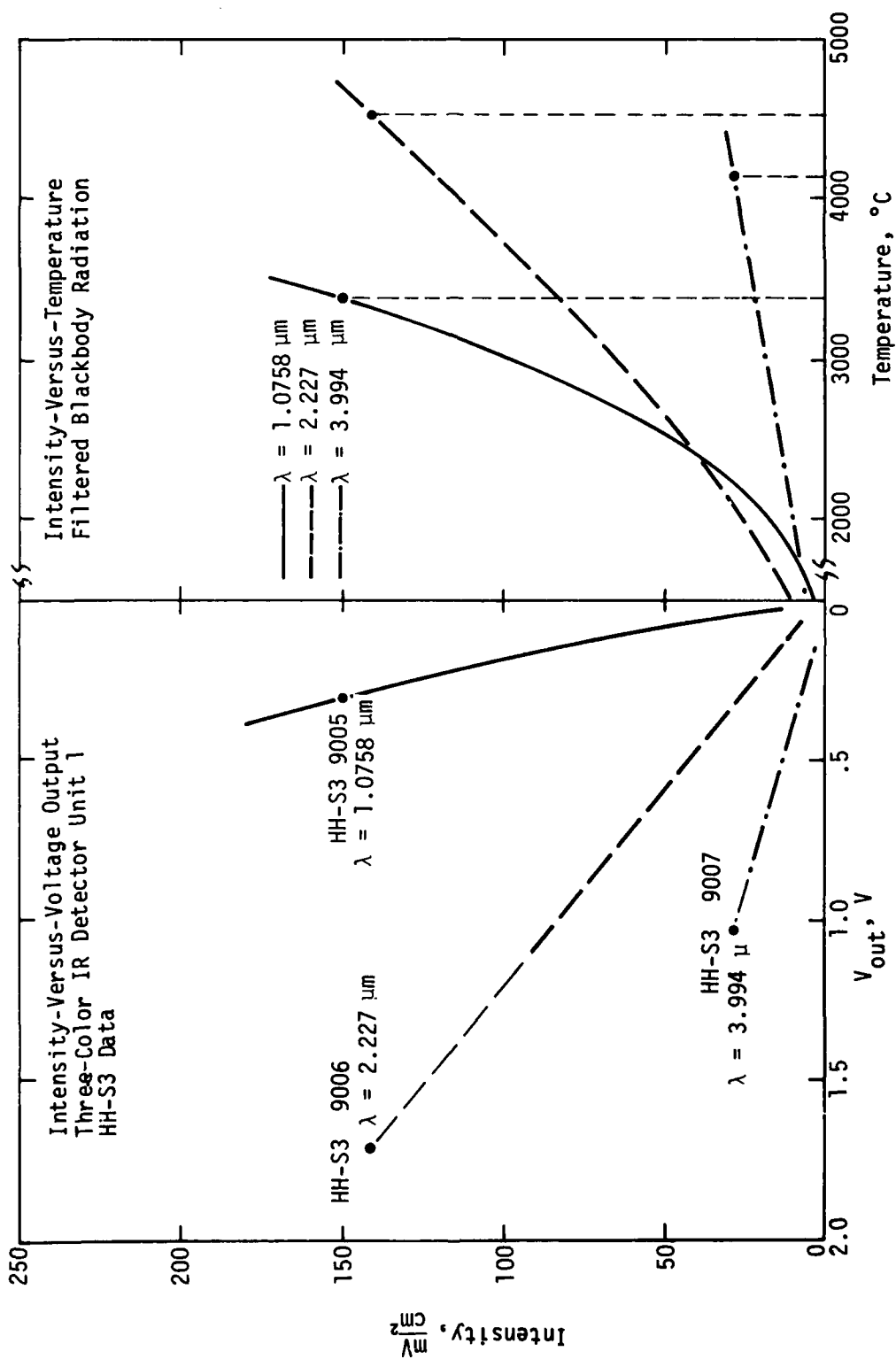


Figure 24. Reduction of HH-S3 Data from IR Detector Unit 1 ($X = 15.2 \text{ m}$)

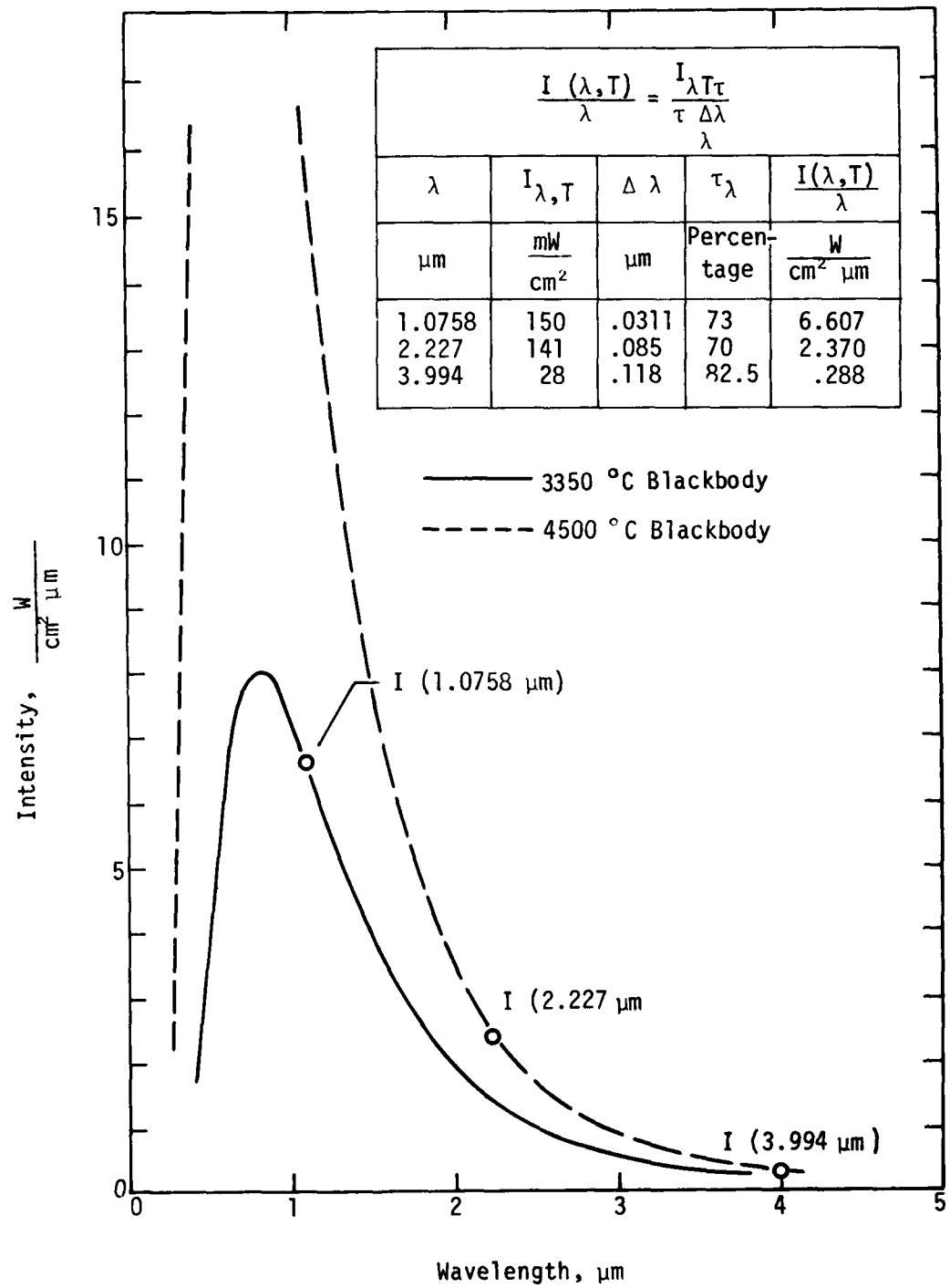


Figure 25. DPI Intensities at X = 15.2 m, HH-S3

The data obtained from the outermost detector (Unit 2, $X = 28$ m) are shown in Figure 26. Unfortunately, the $1.0758\text{ }\mu\text{m}$ channel had to be made so sensitive that the noise induced by another experiment nearby (which is visible on all three channels) obscured the data on the first channel. It is readily apparent from the $2.227\text{-}\mu\text{m}$ and the $3.994\text{-}\mu\text{m}$ channels that the DPI is still about 0.5 ms behind the shock front at this point. It is also apparent from Figure 27 that the DPI is radiating as a blackbody at this station since the temperatures indicated by the intensities at the two wavelengths are essentially coincident at $2700\text{ }^{\circ}\text{C}$. The DPI has cooled down considerably from the 15.2-ms station. The data results and the $2800\text{ }^{\circ}\text{C}$ blackbody spectrum are shown in Figure 28.

The IR detectors fielded on DSOT-I were modified from the HH-S3 configuration to use a different close-coupled electronics circuit as shown in Figure 29. This circuit employs a simple voltage divider instead of a bridge; and the voltage is a.c.-coupled to the amplifier input thus eliminating the drift problem associated with the HH-S3 configuration.

The laboratory blackbody source in conjunction with a chopper (to provide a time-variant stimulus) was used to calibrate the detectors. The calibration curves are shown in Figures 30 and 31.

The data obtained from the Unit 1 (located at $X = 9.15$ ms) are shown in Figure 32.

Unfortunately, only the $2.227\text{-}\mu\text{m}$ detector channel functioned properly, its output rising steadily after detonation and peaking sharply in response to the DPI. The reason for the second peak at 34 ms is unknown. Since the shock front and the DPI cleared the end of the tube by $t = 14$ ms, the second pulse is probably not a reflection. It is interesting to note, however, that since the other channels show some catastrophic response at the same time, the event might be a very intense shock.

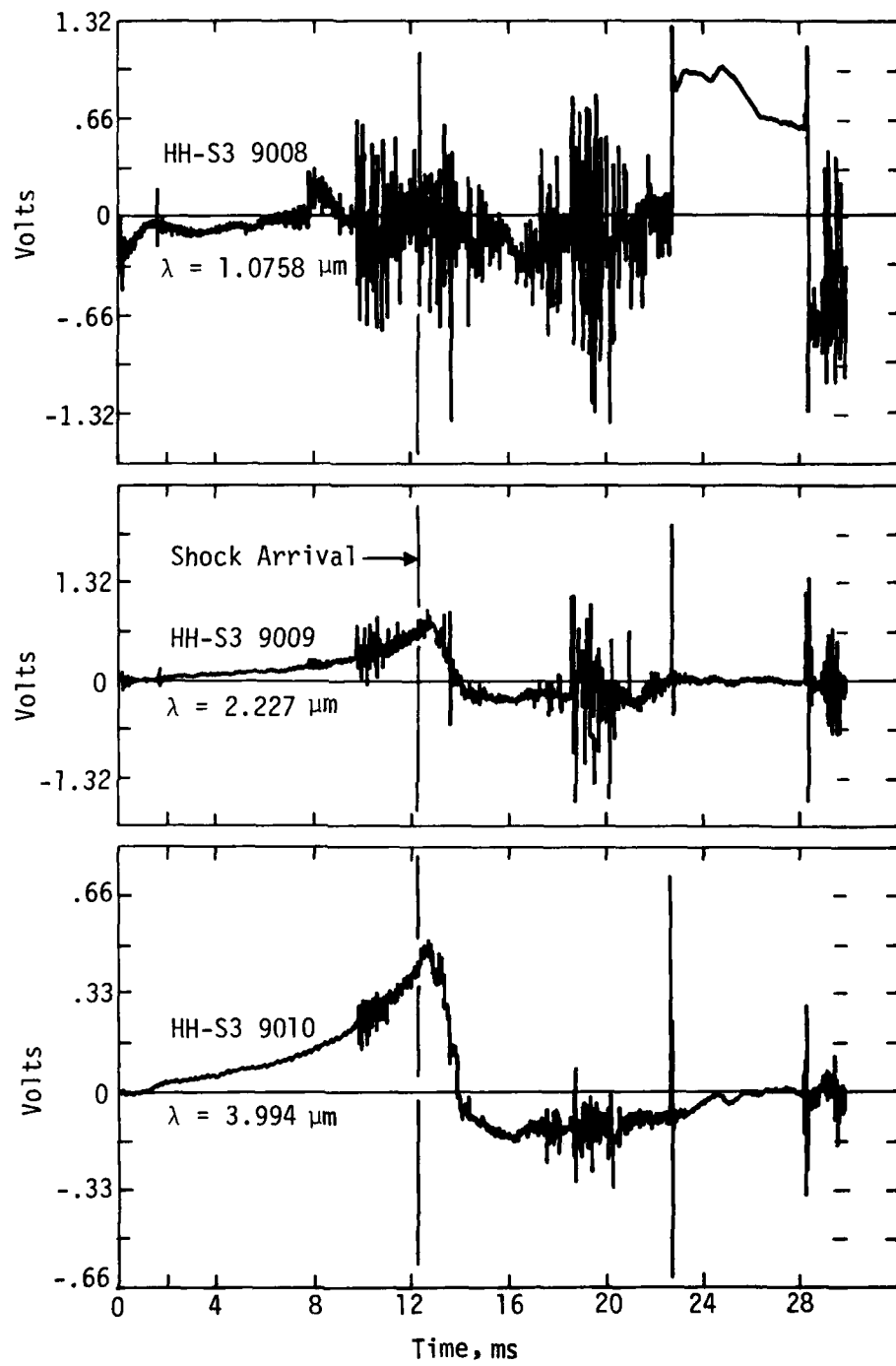


Figure 26. HH-S3 Data from IR Detector 2

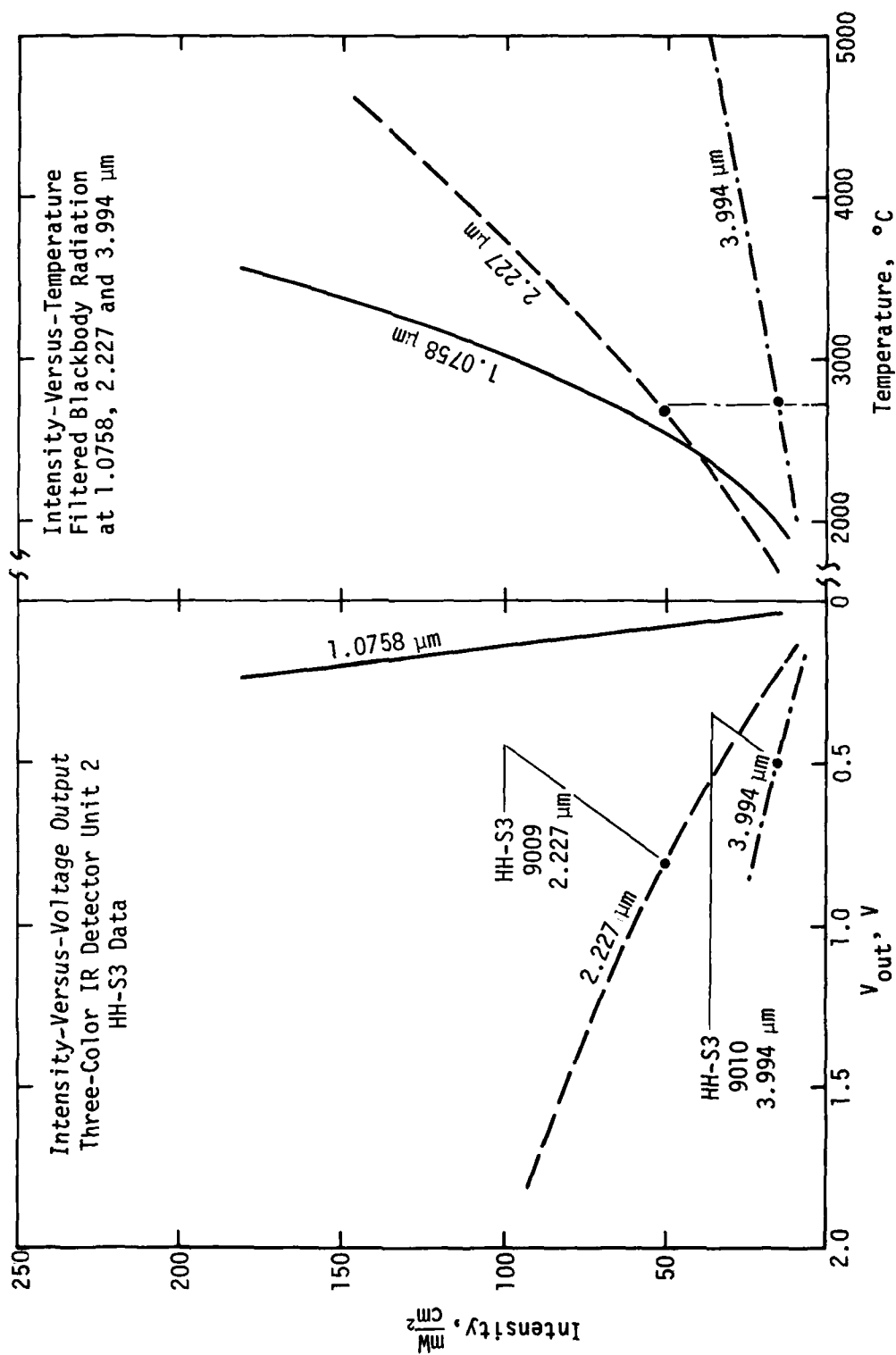


Figure 27. Reduction of HH-S3 Data from IR Detector 2 ($X = 28 \text{ m}$)

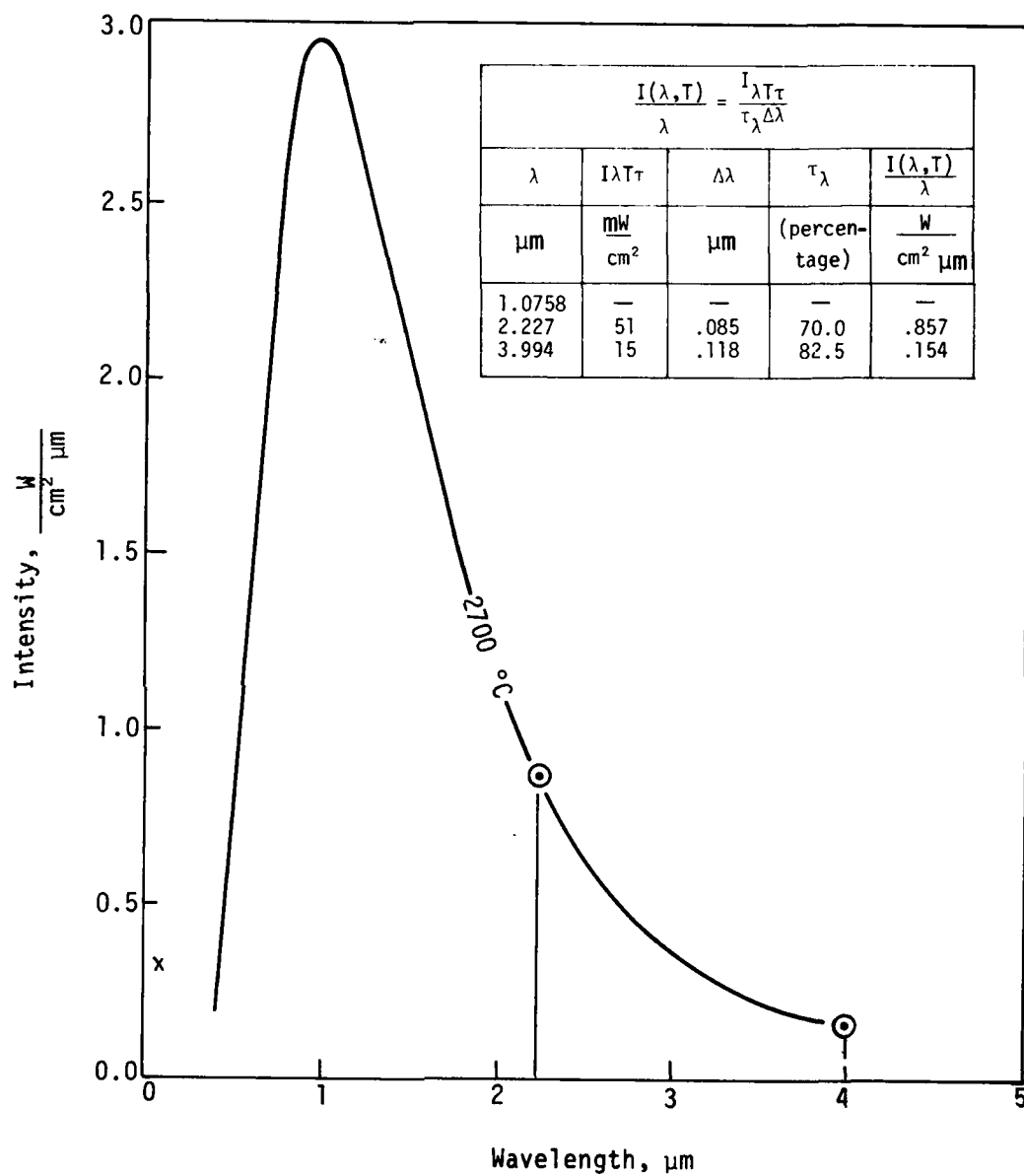


Figure 28. DPI Intensities at X = 28 m, HH-S3

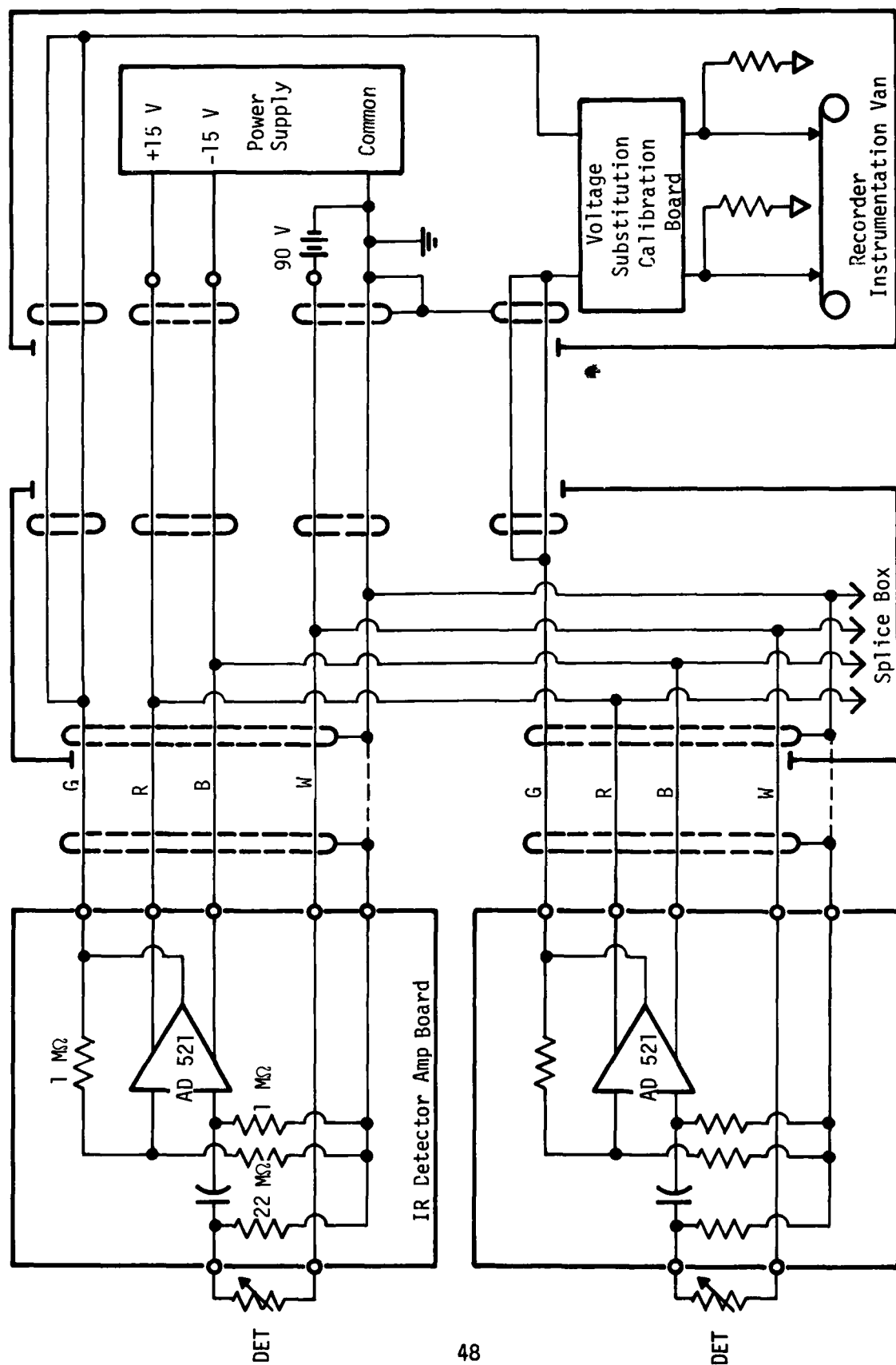


Figure 29. IR Detector Wiring, DSOT-1

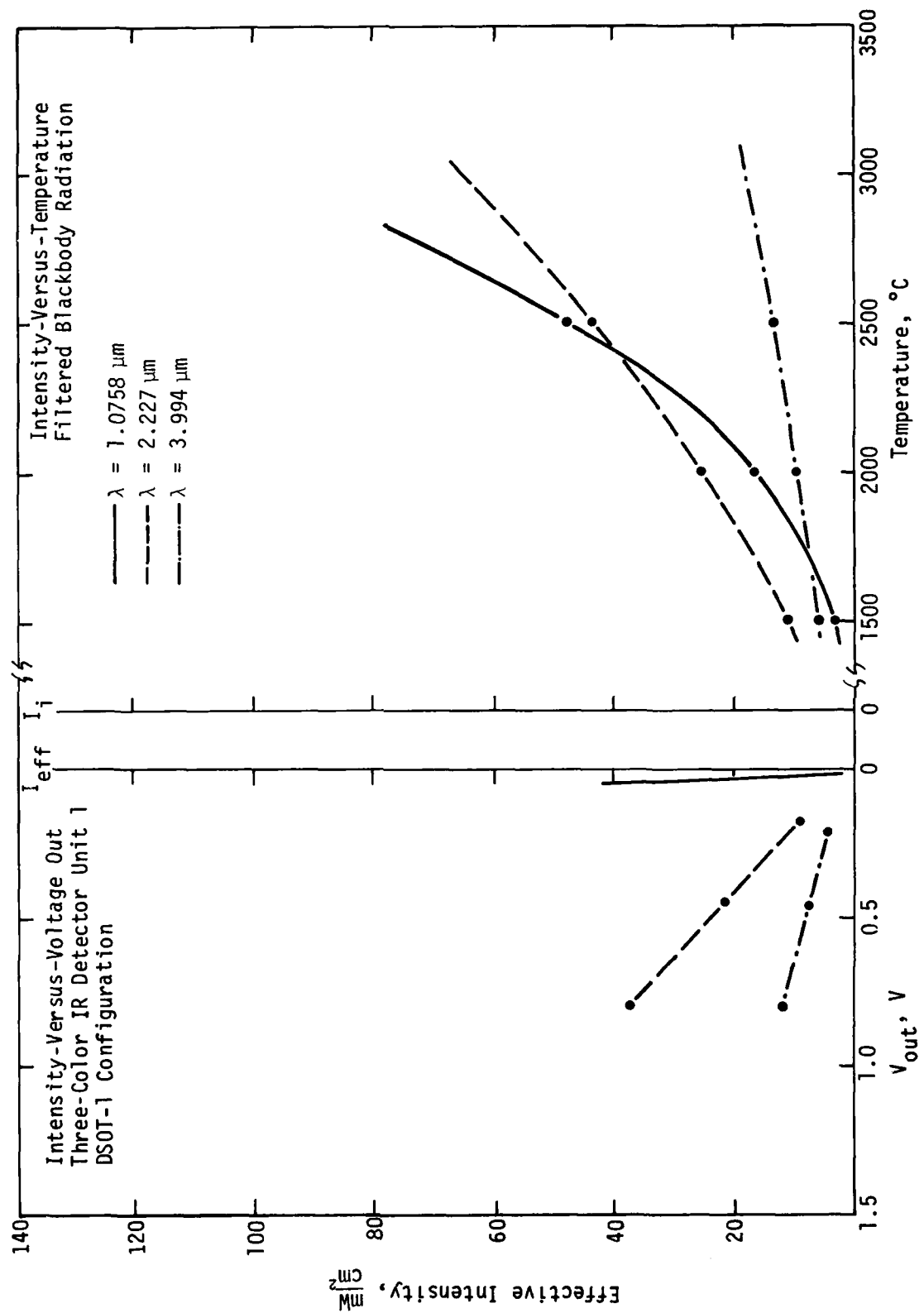


Figure 30. Calibration of Three-Color IR Detector Unit 1, DSOT-I

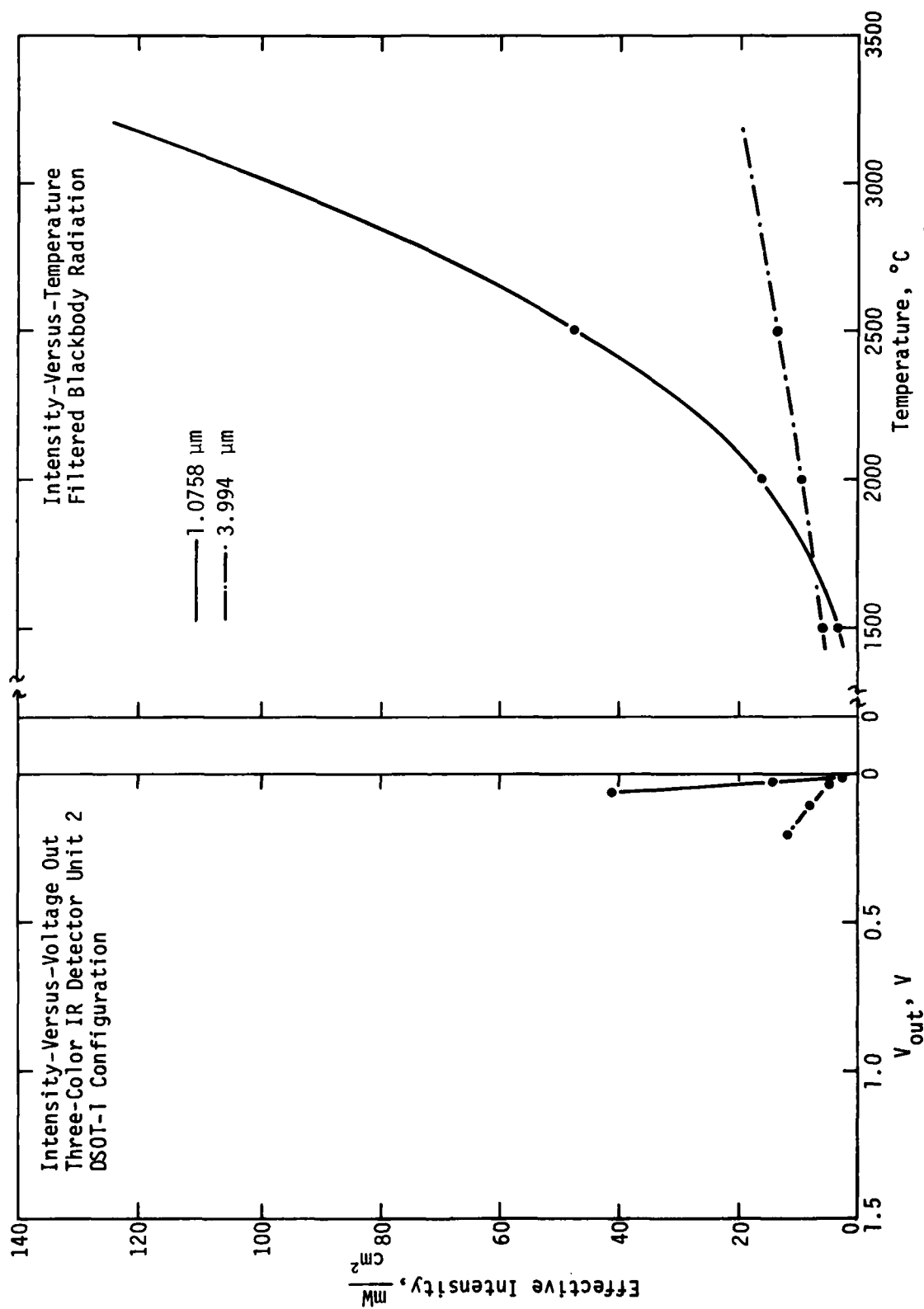


Figure 31. Calibration of Three-Color IR Detector Unit 2, DSOT-I

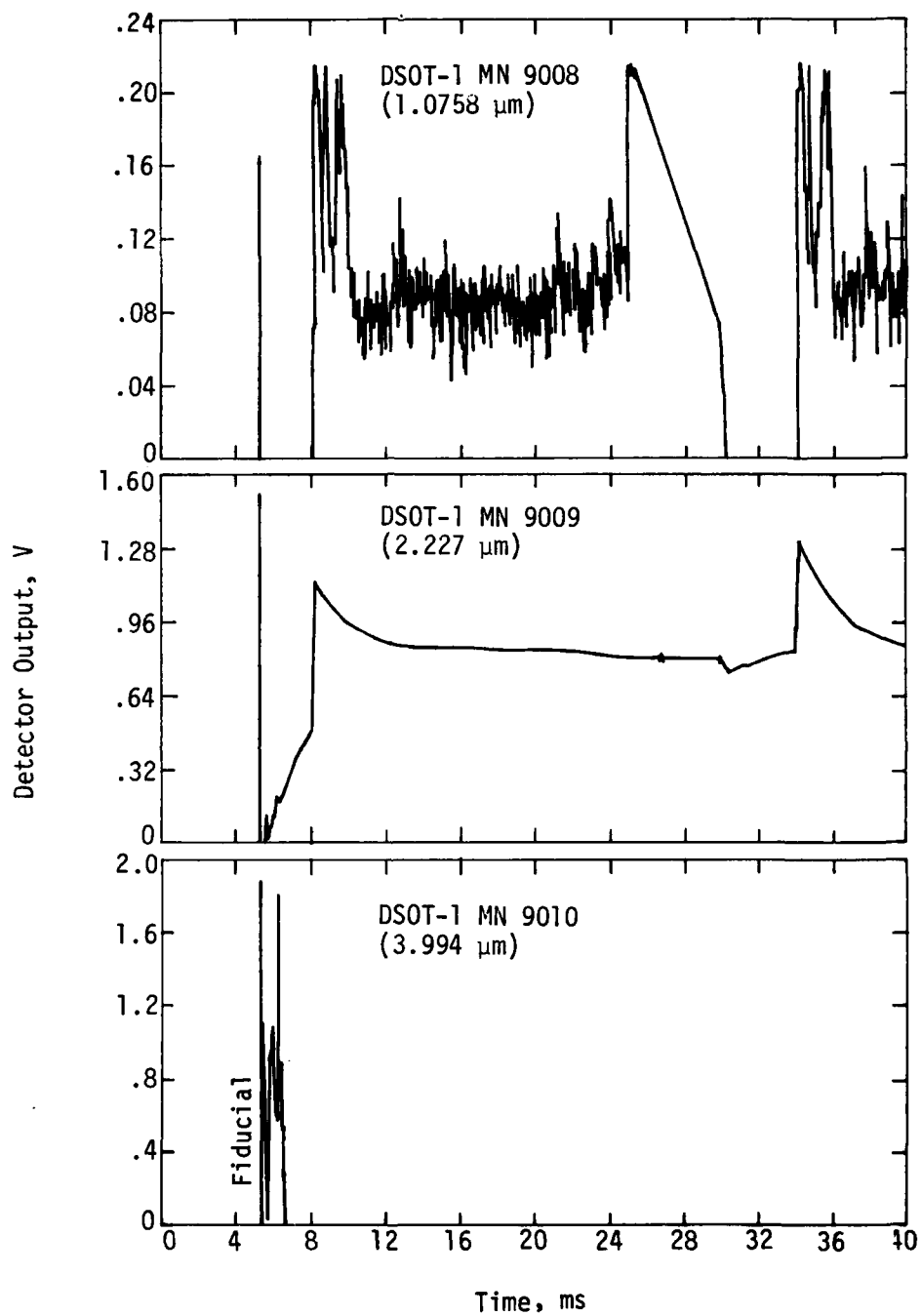


Figure 32. DSOT-I Data from IR Detector Unit 1

The data from Unit 2 (located at $X = 8.15$ ms) are shown in Figure 33. In this case, the $1.0758\text{-}\mu\text{m}$ detector is the only one which obtained even marginally usable data. The cause of the noise (which was intermittent and which was not present immediately before the shot) is thought to have been that the signal line was not properly terminated by the (high impedance) record-amplifier input. This matter will be discussed further in the next section.

The composite of the appropriate calibration curves was employed to reduce the usable data from each detector as shown in Figure 34. The measured temperatures are 3100°C at 8.15 ms and 2750°C at 9.15 ms. Comparison of the crystal pin and B^3 detector data with the IR data indicates that the DPI is traveling right along with the shock front at this point.

Only one detector unit was fielded on DABS-IIIA. It was mounted at the top end of a pipe 10-ft (3.8 m) long and 1.50 in (38.1 mm) in diameter at $X = 12$ ft (3.66 m) as shown in Figure 35. This confrontation was chosen to allow the detonation products to burn more readily as they entered the tube (which has an ample supply of oxygen) and to define more sharply the TOA at the mouth of the pipe. The temperature measured by the detector should thus be lower than that of the DPI in the DABS.

The electronics were the same as the DSOT-I except that the signal lines were terminated in $120\ \Omega$ (Fig. 36). The termination value of $120\ \Omega$ was chosen because the twisted-pair signal line to the recording van has a characteristic impedance of approximately $120\ \Omega$ and because a lower value ($50\ \Omega$ was also tried) attenuated the signal excessively. The termination apparently eliminated the noise problem, which was ascribed to the fact that the amplifier circuit became unstable and went into oscillation.

Calibration of the detector was limited to flashbulb exposure, since the laboratory blackbody was not available. In addition, the 1500°C blackbody points from the DSOT-I calibration were used to establish a straight line as shown in Figure 37.

The data obtained from the IR detector on DABS-IIIA are shown in Figure 38. These data have been filtered to remove a high-amplitude noise signal at approximately $20\ \text{kHz}$, the cause of which is unknown. It may be oscillation of the

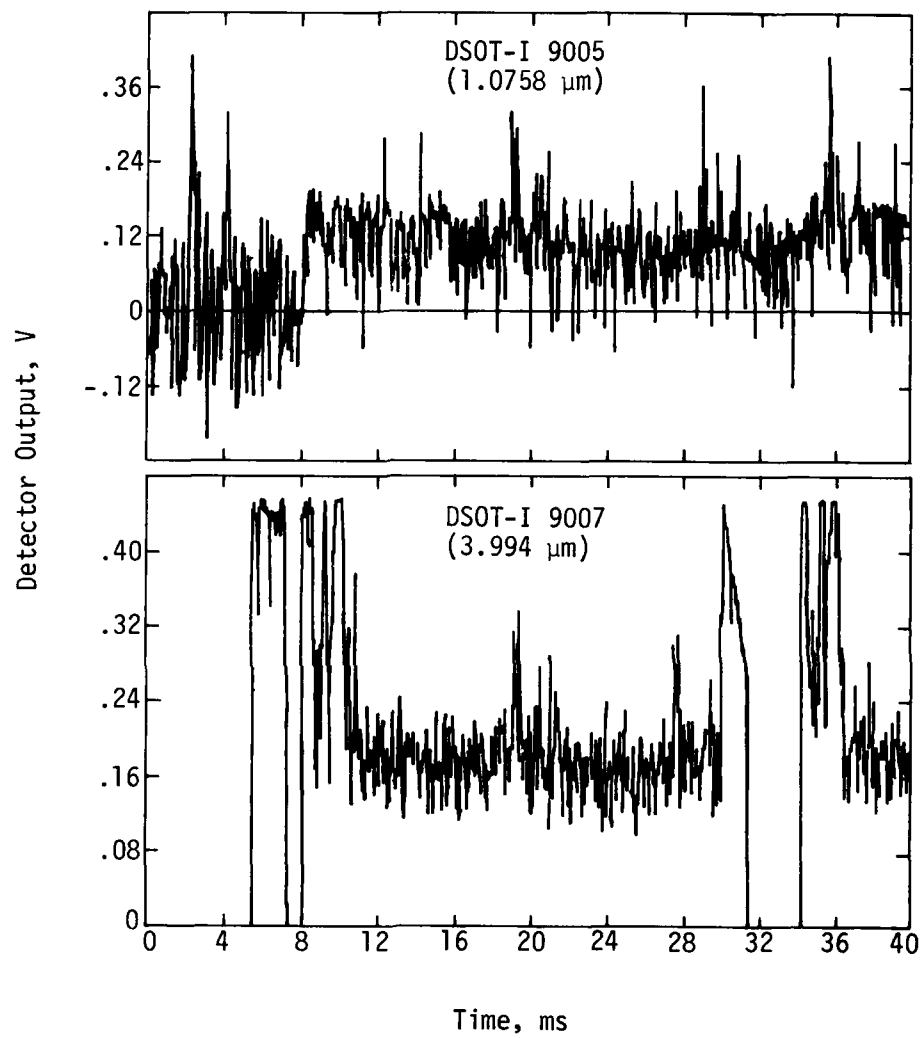


Figure 33. Data from IR Detector Unit 2, DSOT-I

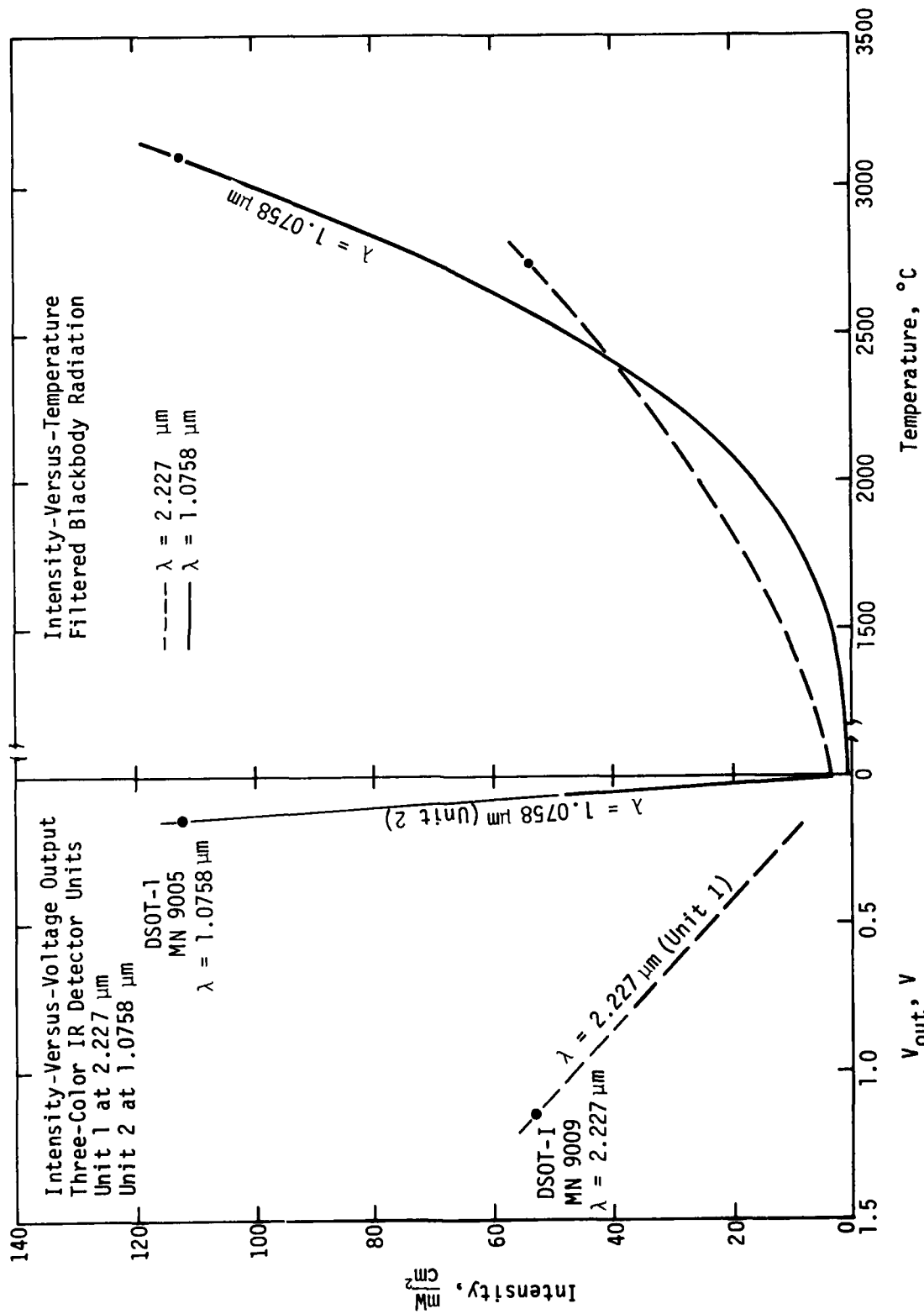


Figure 34. Reduction of DSOT-I Data from IR Detector Units 1 and 2

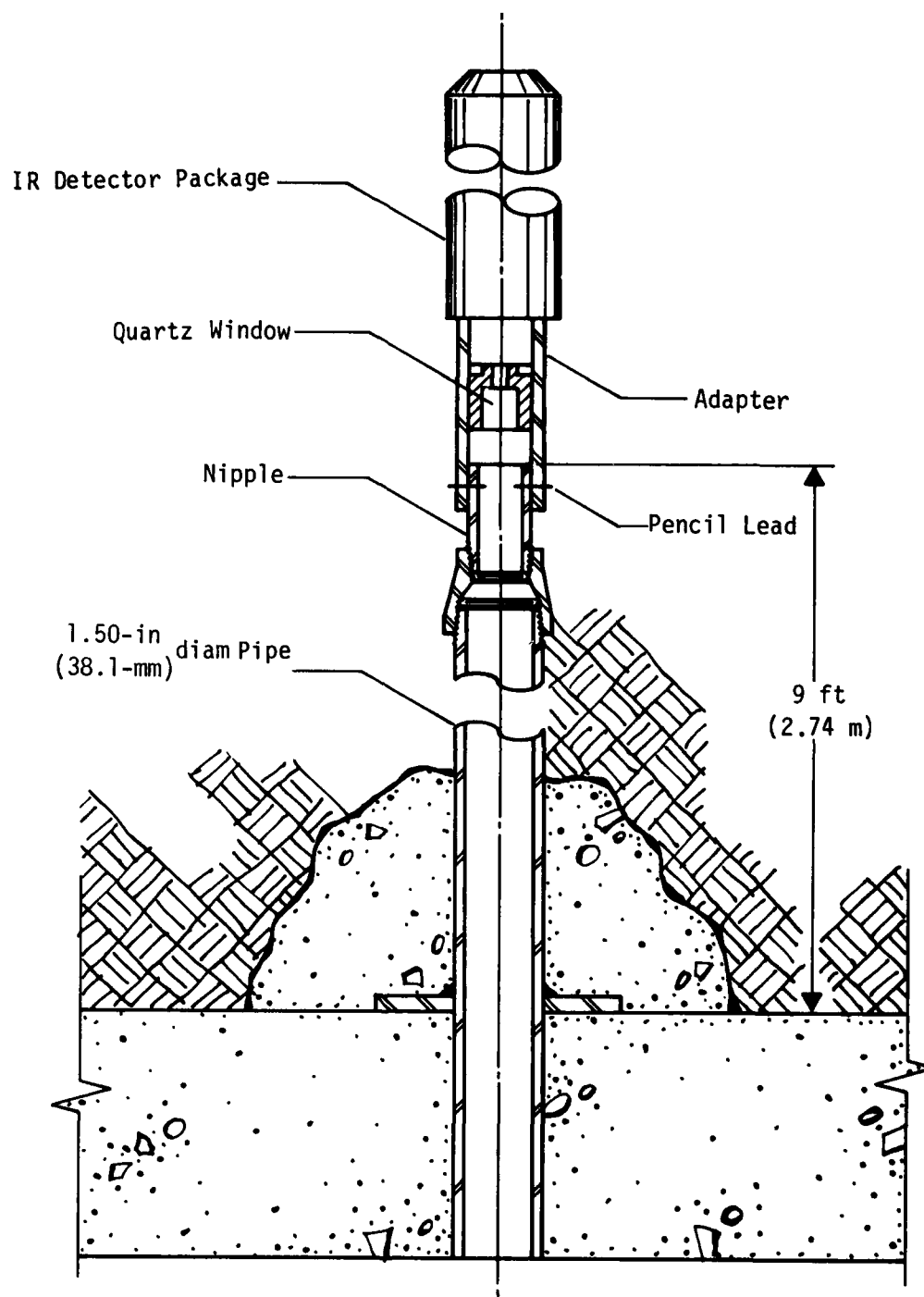


Figure 35. IR Detector, DABS-IIIA

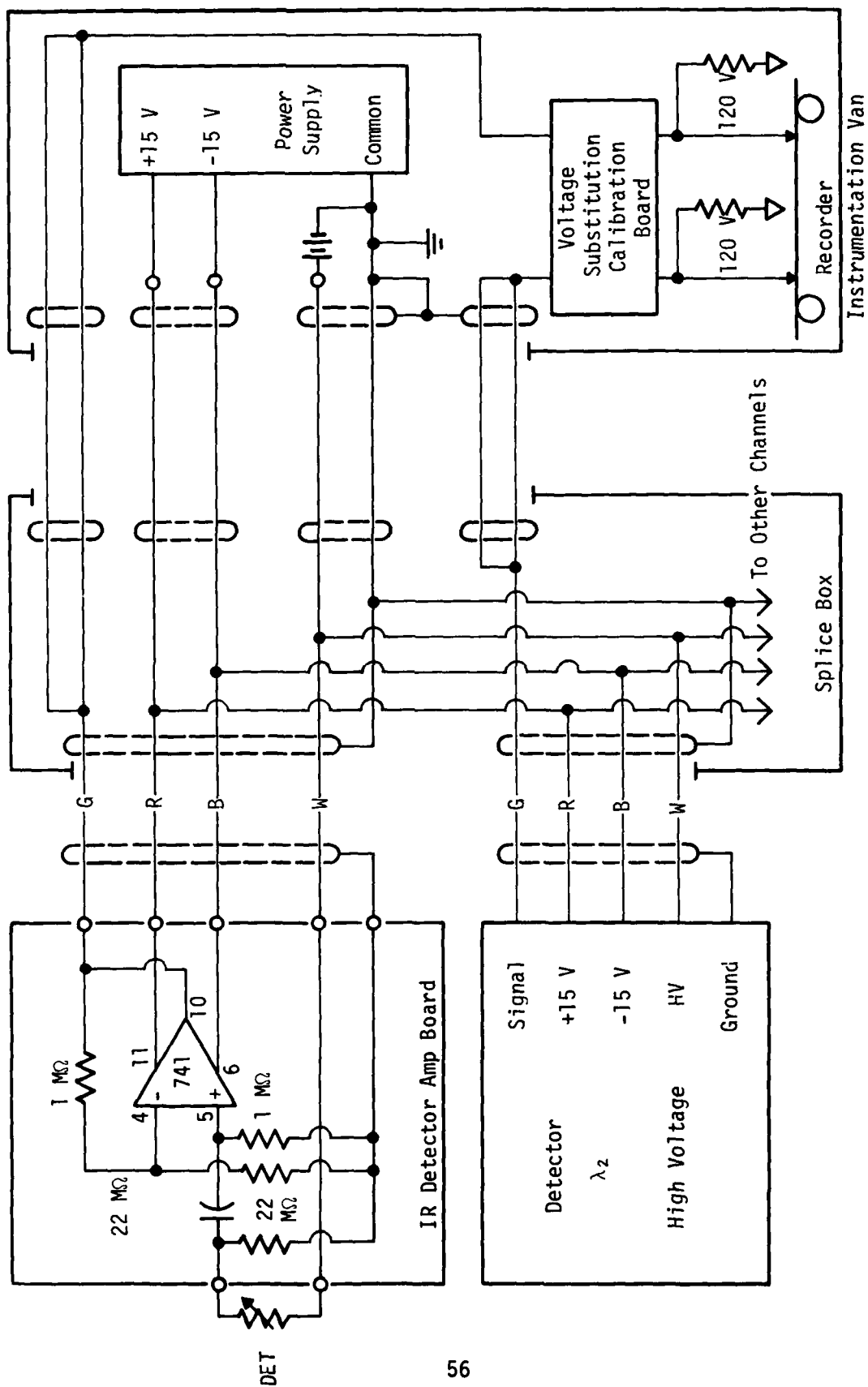


Figure 36. IR Detector Instrumentation, DABS-IIIA

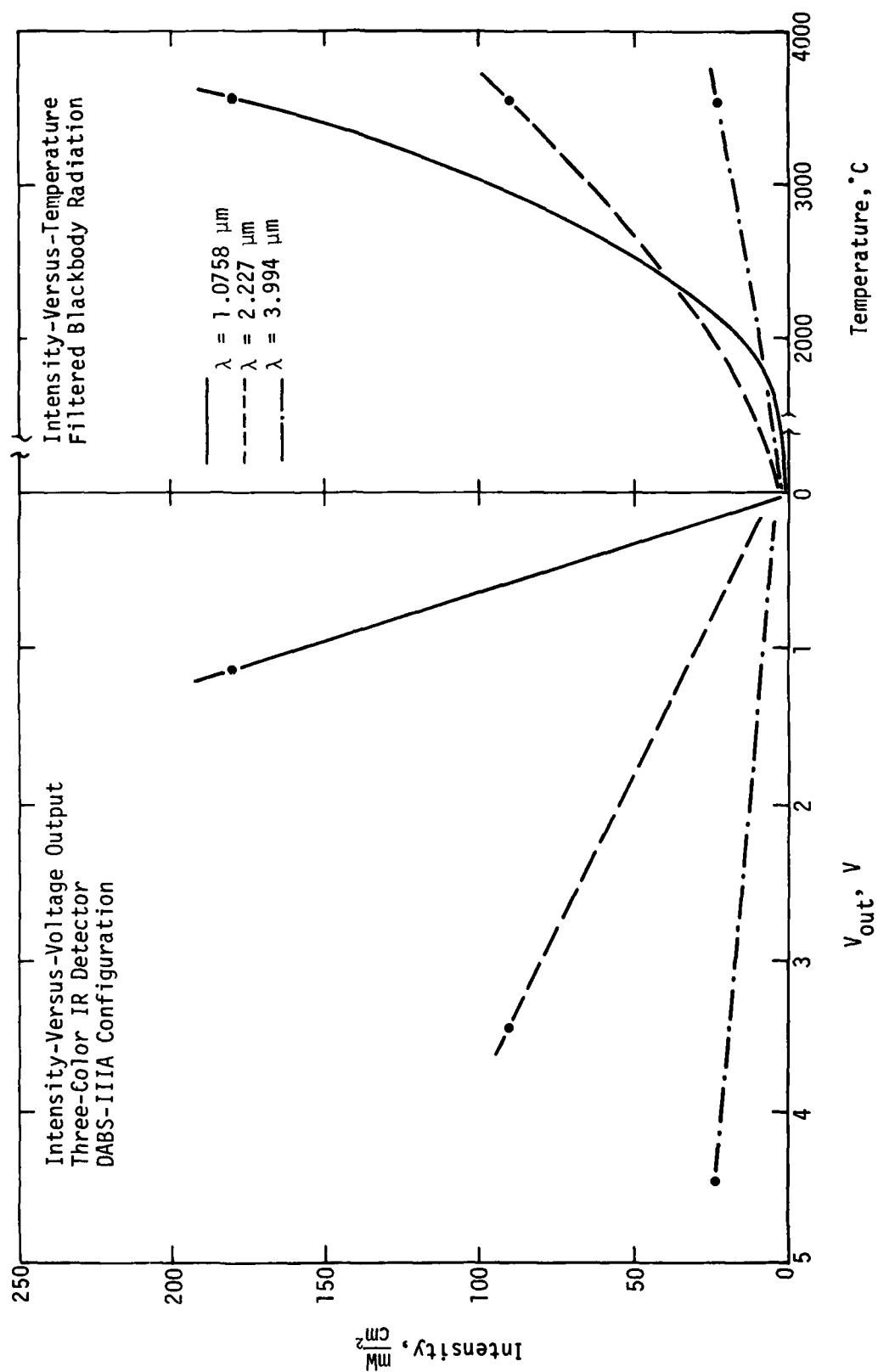


Figure 37. Calibration of Three-Color IR Detector, DABS-IIIA

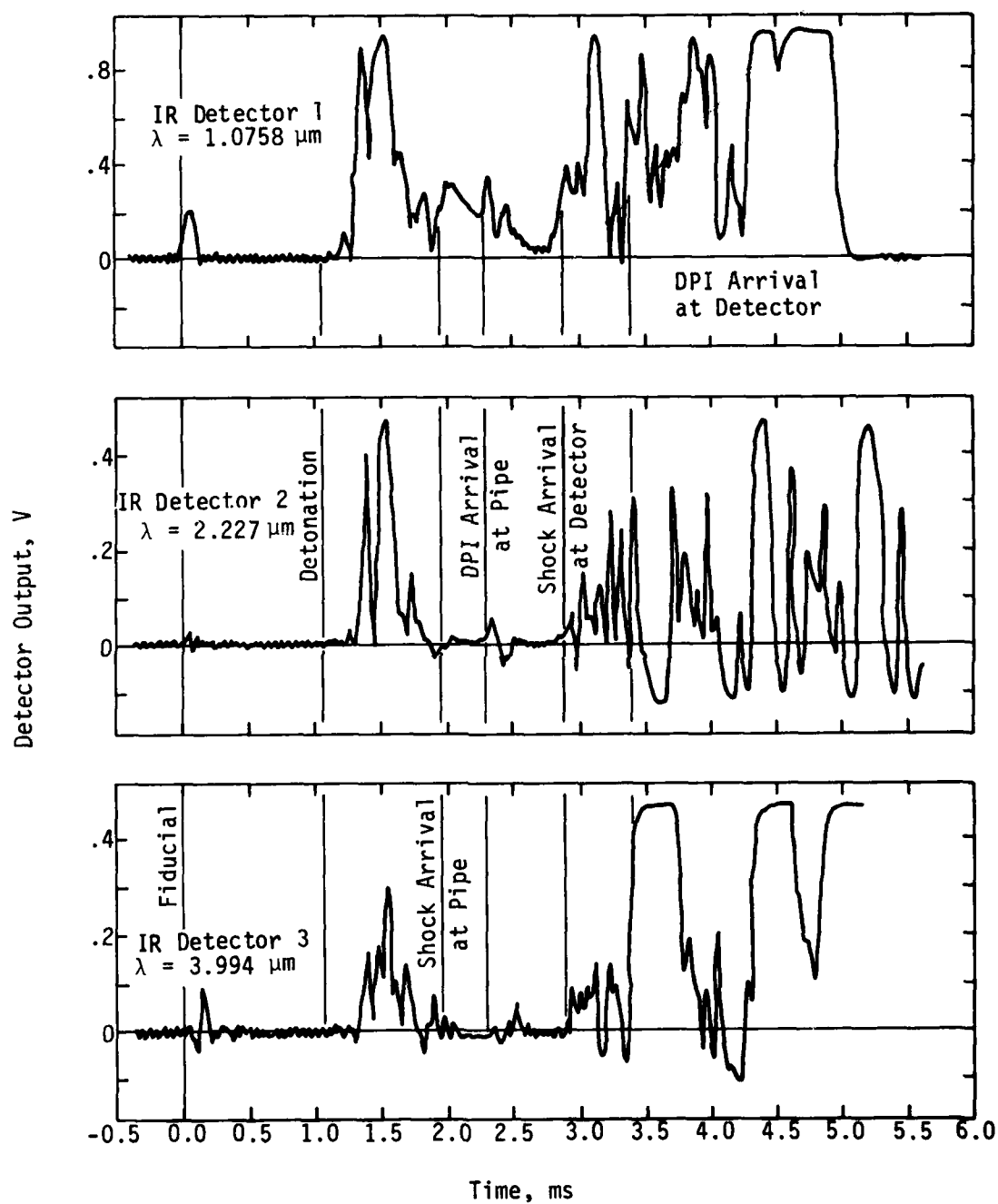


Figure 38. DABS-IIIA Data from IR Detector

amplifier circuit. However, as in the previous instance, the noise was not present before the shot. The amplifier output circuit, moreover, was terminated at this time.

There is a marked difference between the waveforms of the DABS-IIIA data and the data from the previous tests. In previous tests, the detector signal shows several small peaks at the time of detonation. It is not known whether these peaks are responses to optical radiation or to some other phenomena or to a combination of both. The signal then increases steadily to the TOA of the DPI, at which point it peaks sharply. No response to shock arrival is evident in previous tests because the shock front has become relatively cool by the time it hits the detector. The DABS-IIIA waveforms differ from the foregoing because the detector is at the end of a 10-ft (3.048-m) pipe and because it is much closer to the charge than previously. Here the signal peaks strongly just after detonation, which occurs at $0 + 1.07$ ms. These peaks are thought to be analogous to those associated with detonation in previous tests. The signal then peaks weakly at shock arrival at the mouth of the pipe, 1.97 ms (measured from crystal pin TOA data); it peaks again at what is assumed to be shock arrival at the detector, 3.02 ms. These times indicate that the DPI lags the shock front by about 0.375 ms at the 12-ft (3.658-m) station.

After shock arrival at the detector, there are several peaks which are thought to represent radiation from enhanced burning of the detonation products in the oxygen-rich pipe. This phase in previous tests was characterized by a steady rise in the signal. The strong coincident peaks at 3.75 ms are assumed to be the arrival of the DPI at the detector. The magnitudes of these peaks were reduced to temperatures as shown in Figure 39. The DPI seems to be radiating like a blackbody between 1600 and 1800 °C, within the uncertainties associated with the "calibration" curves. These curves, it should be re-emphasized, are derived from a calibration point from a previous test. Several other peaks, for example, were reduced to temperature at such points as shock arrival at the mouth of the pipe and at the detector and the DPI arrival at the mouth of the pipe. The general pattern of the data demonstrated close agreement between the temperatures indicated at 2.227 and 3.994 μm , and a significant difference between these and the higher temperature indicated by the 1.0758- μm detector.

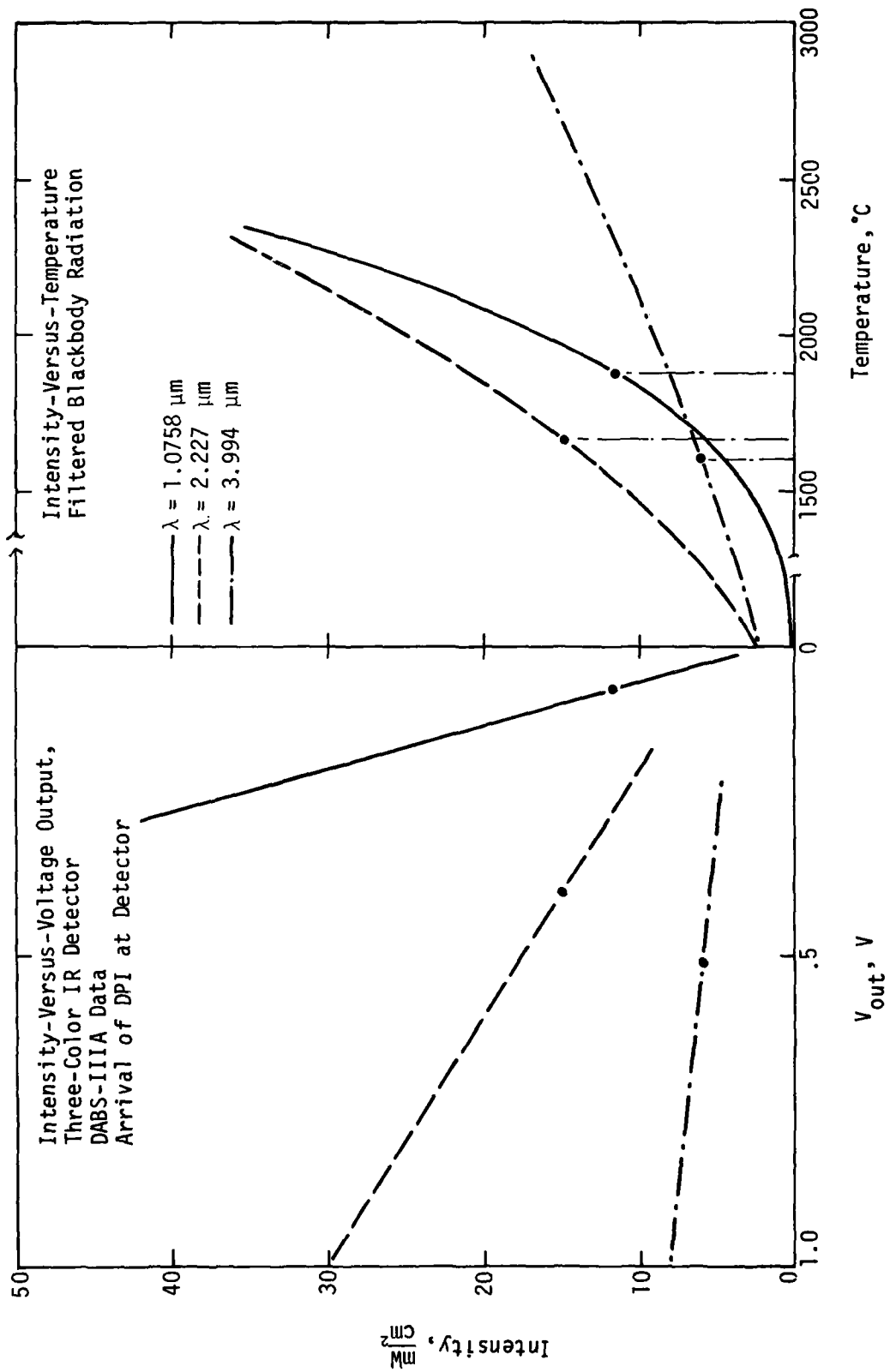


Figure 39. Reduction of DABS-III IR Detector Data - DPI at Detector

This suggests the possibility of a gross error in the 1.0758- μ m detector calibration curve or an emission line near 1 μ m in the spectrum of the DPI.

In an attempt to shed additional light on the large peaks just after detonation, the largest ones were reduced to temperatures as shown in Figure 40. The disparity in the indicated temperatures is larger than and somewhat different from that in the temperatures indicated for the DPI arrival at the detector and other coincident peaks which were reduced, particularly at the 3.994- μ m wavelength. Had the divergence been the same or proportional, that fact would have supported the speculation that the peaks are in fact responses to optical radiation.

The results of Phase II experimentation with IR detectors are summarized in Table 3. Several conclusions are apparent from the table. First, there is a wide discrepancy between lag times for the DPI behind the shock front. This disparity casts suspicion upon the HH-S1 and the HH-S2 data as compared with later tests and may indicate that what seems to be detector response to the DPI may be a response to something else. Second, the 1.0758- μ m detector has a less-than-admirable track record for the test series. This poor record may be partly due to the high sensitivity which has of necessity been used in order to bring this detector into a reasonable operating range. For whatever reasons, the 1.0758- μ m detector either gave a substantially higher or lower temperature than the other two or was too noisy to use.

In general, the three-color detection scheme seems to have potential for temperature measurement in the incandescent environment. Several improvements are needed, however, to make the scheme work reliably. Of primary importance is a good calibration method permitting calibration (preferably dynamic) at several temperatures in the 3000-4000 $^{\circ}$ C range. The present flashbulb method is deficient because only one point is available and because there is only an average specification instead of an accurate, specific temperature for any given bulb.

Another needed improvement is a close-coupled amplifier circuit which will not go into oscillation with large slew rates as the present circuit seems prone to do. An additional improvement might be made in the 1.0758- μ m detector

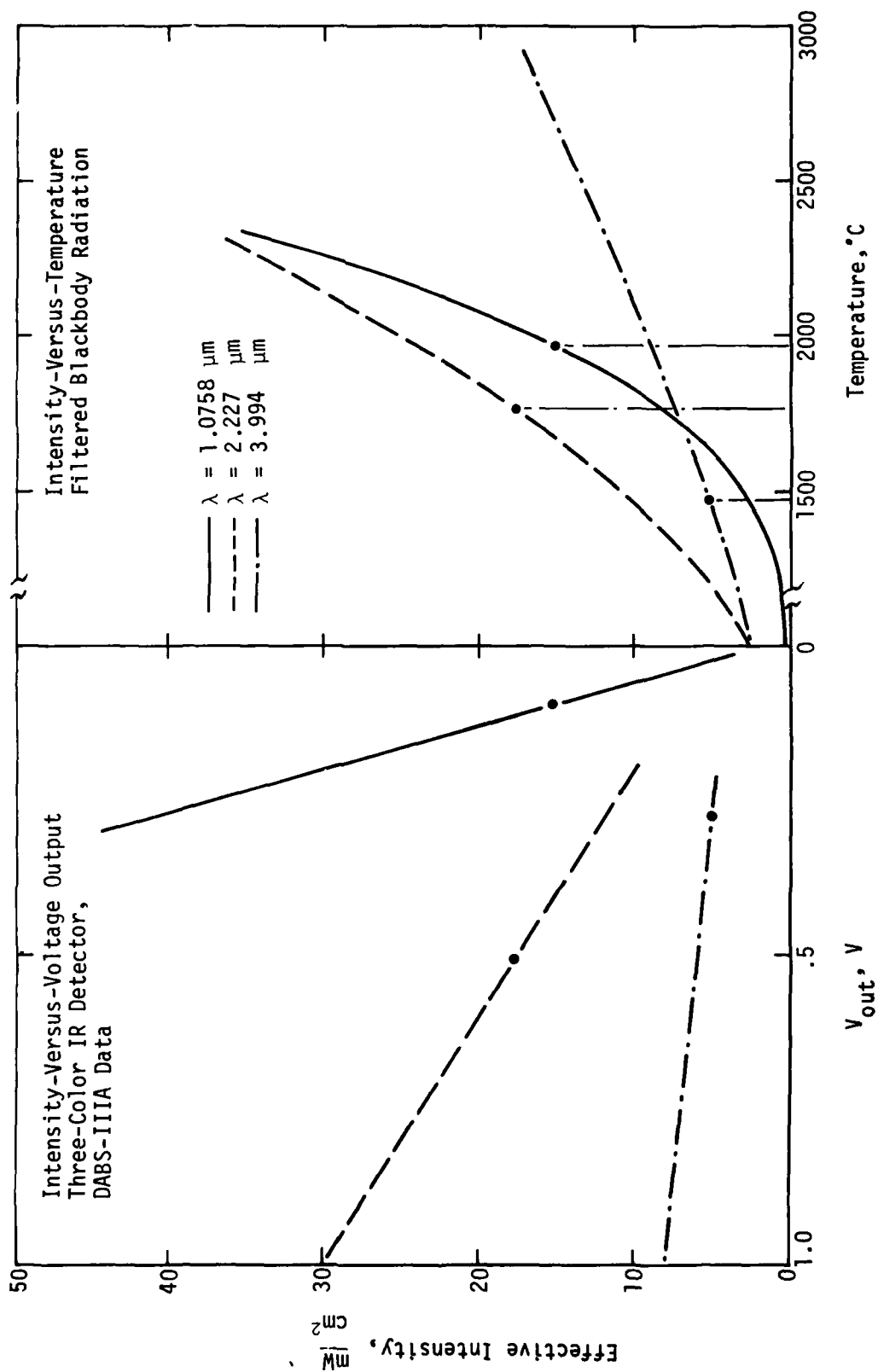


Figure 40. Reduction of DABS-IIIA IR Detector Data, Detonation Peak

TABLE 3. RESULTS OF INFRARED-DETECTOR EXPERIMENTS

Event-Detector	X (m)	Δt Shock-DPI (ms)	T_{Y3} (°C)	T_{Y2} (°C)	T_{Y3} (°C)	T_{AVG} (°C)	Remarks
HH-S1-1		4.600					Failed electrically preshot.
HH-S1-2							
HH-S2-1	15.00	2.250					
HH-S2-2							Failed due to shock.
HH-S3-1	15.20	0.500	3350	4500	4125	3992	1.075 μ m detector temperature low, compared to 2.227 μ m and 3.994 μ m detectors.
HH-S3-2	28.00	0.500	--	2725	2675	2700	1.075 μ m detector too noisy.
DSOT-II	9.15	0.000	--	2750	--	2750	1.075 μ m and 3.994 μ m detectors failed.
	8.15	0.000	3100	--	--	3100	3.994 μ m detector too noisy to read.
DABS-IIA	3.60	0.375	1880	1660	1600	1713	Detector at end of 10-ft pipe. 1.075- μ m detector temperature high, compared to 2.227 μ m and 3.994 μ m detectors.

performance. It may be advantageous to select another filter (in the 1.0758- μm region) which has a wider bandpass. Such a filter would allow the amplifier to be operated at a lower gain and would thus reduce the noise.

In order to widen our experience and increase our confidence in or more clearly reject the blackbody DPI hypotheses, more tests should be conducted using detectors filtering at different wavelengths. If there are emission lines in the DPI which are at or near the chosen wavelengths, it is possible that they could be avoided by using, for example, 1.5, 2.75, and 3.25 μm filters. Of course, the possibility of an emission line at any of these wavelengths does exist; nevertheless, three new wavelengths would help to define the spectrum of DPI better. The next step would then be to try six simultaneous measurements. This would necessitate a close-coupled multiplex scheme and a complementary discrimination system but would increase the confidence in the overall description of the spectrum of the DPI. This improvement is illustrated in Figure 41, which shows the data taken from HH-S3 detector Unit 1 with three additional hypothetical points which might be obtained from the three additional detectors. These kinds of data would help to identify emission lines and would help to show the basic spectrum more clearly, provided that just one or two of the three additional points were not on emission lines.

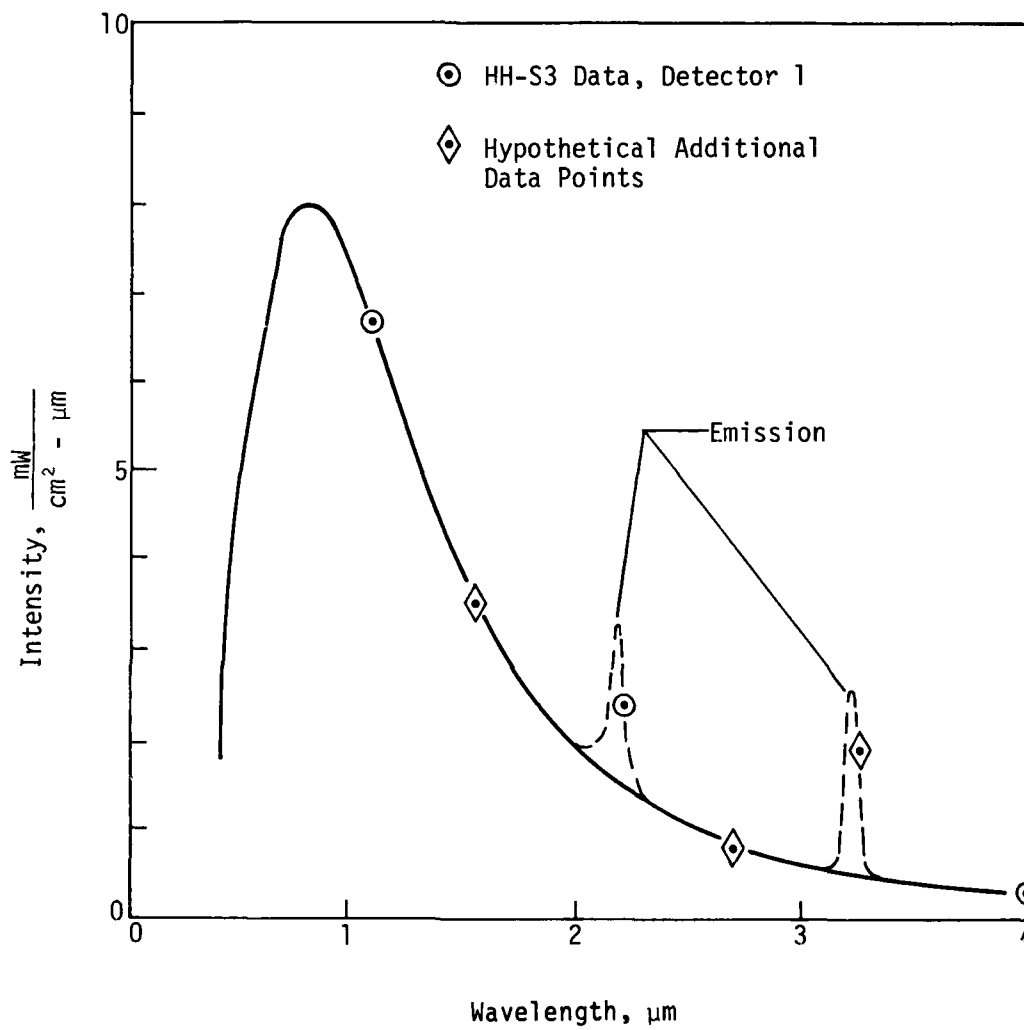


Figure 41. Improved Spectral Definition Resulting from Additional Data Points

SECTION IV BLAST BEHIND BLAST (B³)

The Blast-Behind-Blast (B³) or Shock-On-Shock (SOS) technique provides a method of measuring the local Mach number in the flow behind the shock wave after it has passed the measurement point. The Mach number is defined as the ratio of the flow or particle velocity to the local acoustic velocity, u/c . These two velocities are measured in the B³ experiment. A secondary explosive charge is detonated some time after the primary blast wave has passed the measurement point where TOA measurements are made by an array of detectors. The velocities are calculated from the TOA data and the geometry of the experiment layout.

A typical B³ experiment layout is shown in Figure 42. It is to be assumed that the primary blast wave has passed over the detector array and that the atmosphere behind the shock is flowing to the right with a (flow) velocity of \vec{u} . The secondary charge is detonated, and the secondary blast wave propagates outward from the working point with (local acoustic) velocity \vec{c} . The secondary wavefront then propagates toward the detector array with velocity \vec{v} , the vector sum \vec{u} and \vec{c} . In other words, the flow "blows" the secondary wavefront downstream toward the detector array.

The simplifying approximation can be made that the distances between the detectors are small compared to the distance between the array and the origin of the secondary blast; i.e., that the wavefront is planar when it passes over the array. It should be noted that the wavefront is not perpendicular to the resultant direction of propagation, which is along a ray from the origin to the array. The ray is at an angle of ϕ with the direction of the primary flow, and the wavefront is at an angle of θ with the primary flow. By means of the foregoing approximation, it can be shown that:

$$\tan \theta = \frac{\Delta X}{\Delta Y} \frac{\Delta t_2}{\Delta t_1} \quad (10)$$

$$u = \frac{\Delta Y}{\Delta t_2} \tan (\theta - \phi) \quad (11)$$

$$c = \frac{\Delta Y}{\Delta t_2} \sin \theta \left(1 - \frac{\tan (\theta - \phi)}{\tan \theta} \right) \quad (12)$$

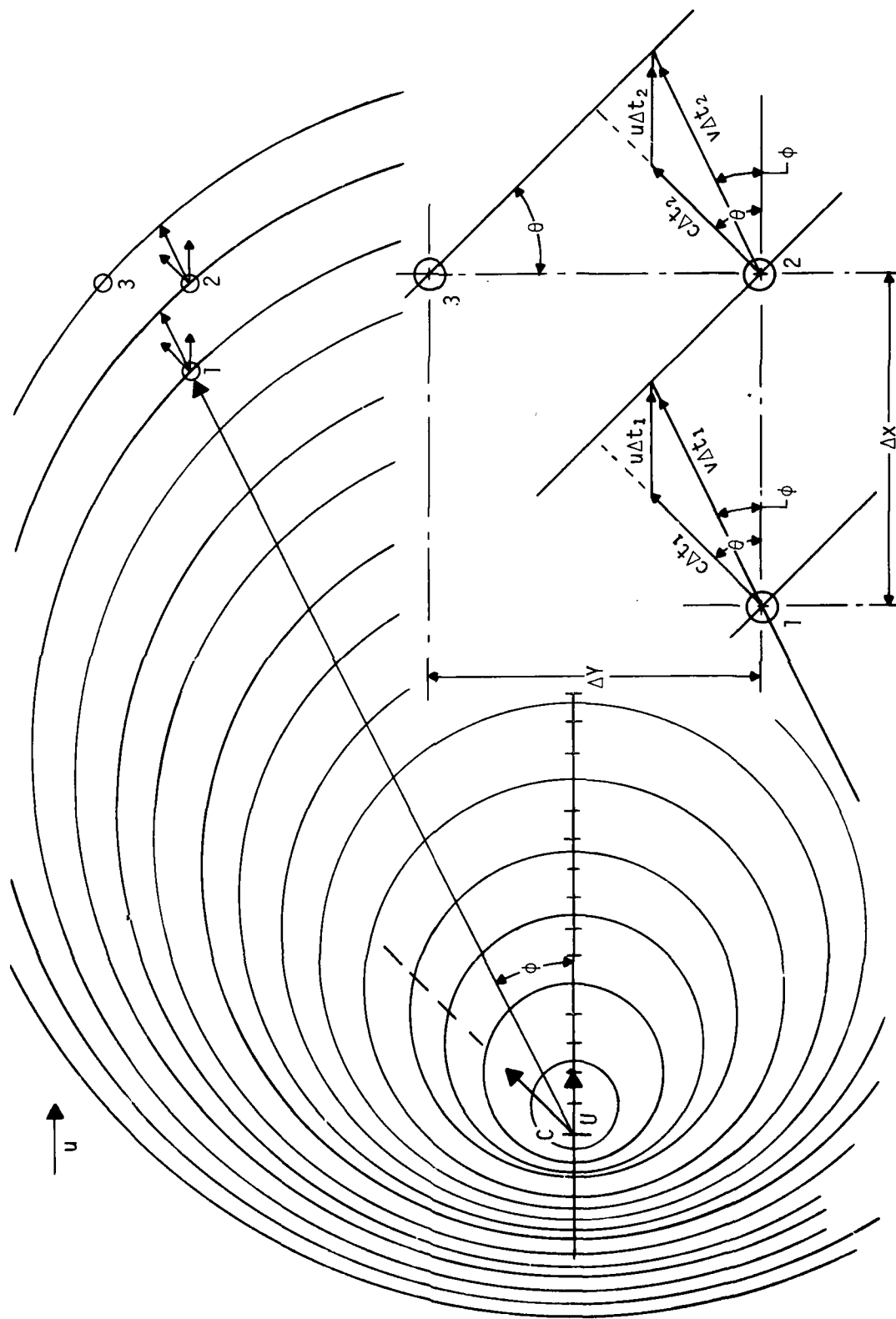


Figure 42. Blast Behind Blast (B³) Experiment Layout

The detectors used in the DABS tests were PCB piezoelectric pressure transducers, which feature very fast rise times and integral electronics. Various methods have been used to detonate the secondary charge, including crystal pins and pressure switches placed downstream from the array and time delay circuits which fire the secondary charge at a present time after the primary charge is fired. The latter method has proved most successful in the DABS tests conducted so far.

Development of the B^3 technique in Phase I was limited to one experiment in the DABS-IE test. The experiment was a qualitative but not quantitative success. While the secondary charge was successfully detonated by downstream crystal pins, the magnitude of the secondary pressure pulses was so small (Fig. 43) that they could not be separated clearly enough from the noise to obtain sufficient precision to calculate \vec{c} and \vec{u} . This problem was overcome in Phase II by using a larger secondary charge and by "aiming" it more directly at the detector array.

The first Phase II B^3 experiment fielded on HH-S1 is shown in Figure 44. The secondary charge was contained in a steel canister welded to an arch rib. The canister served to direct the secondary blast toward the detector array, which in this case consisted of four detectors, three of which were in a straight line. The secondary charge was intended to be detonated by a pressure switch located 30 ft (9.144 m) downstream from the detector array. Unfortunately, the charge was detonated concurrently with the main charge. The reason for the premature detonation was investigated exhaustively but not found.

The layout of the B^3 experiment fielded on HH-S2 is shown in Figure 45. For this experiment, the secondary charge was detonated by means of a relay closure from the Test Command and Control (TCC) station, which was delayed approximately 10 ms from the closure for the primary detonation.

The data resulting from the HH-S2 B^3 experiment are shown in Figure 46. The glitches were used to improve time correlation between the four data channels. The glitch induced by the primary fiducial pulse on the detector records was used to normalize the records to a common time base.

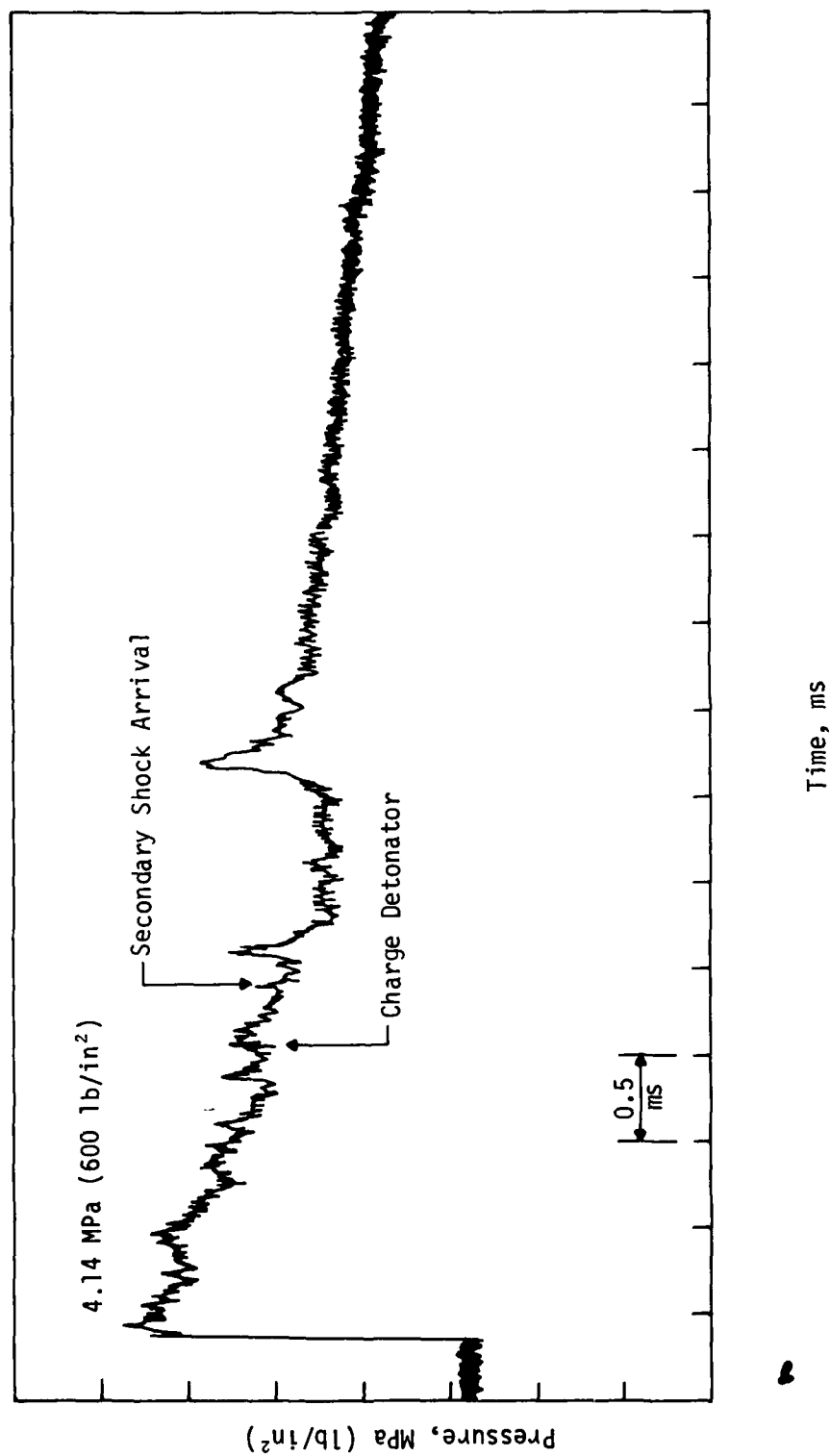


Figure 43. Shock-on-Shock (SOS) Experimental Data (Gage 1 Output)

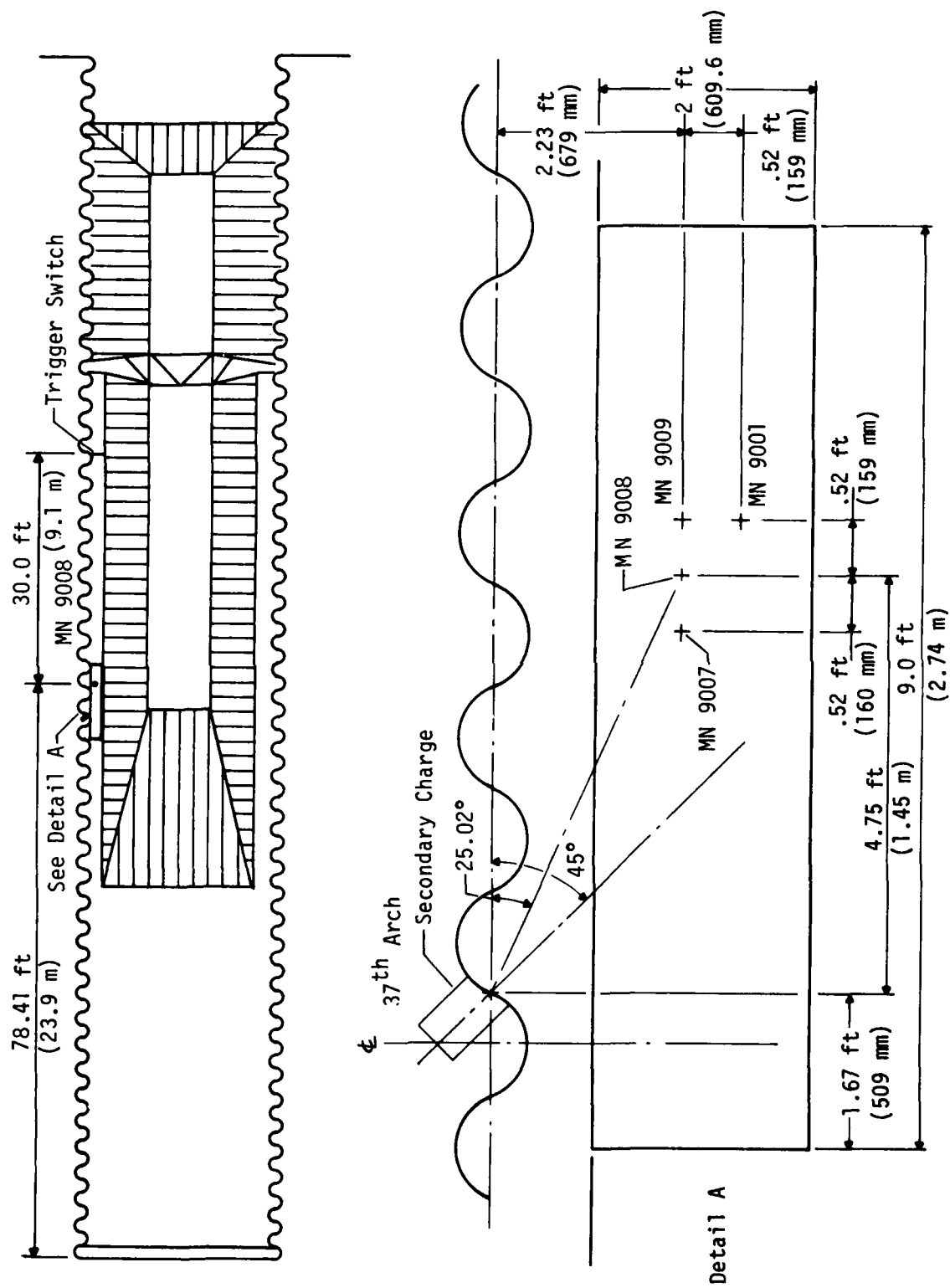


Figure 44. Test-Bed Layout, HH-SI B³ Experiment

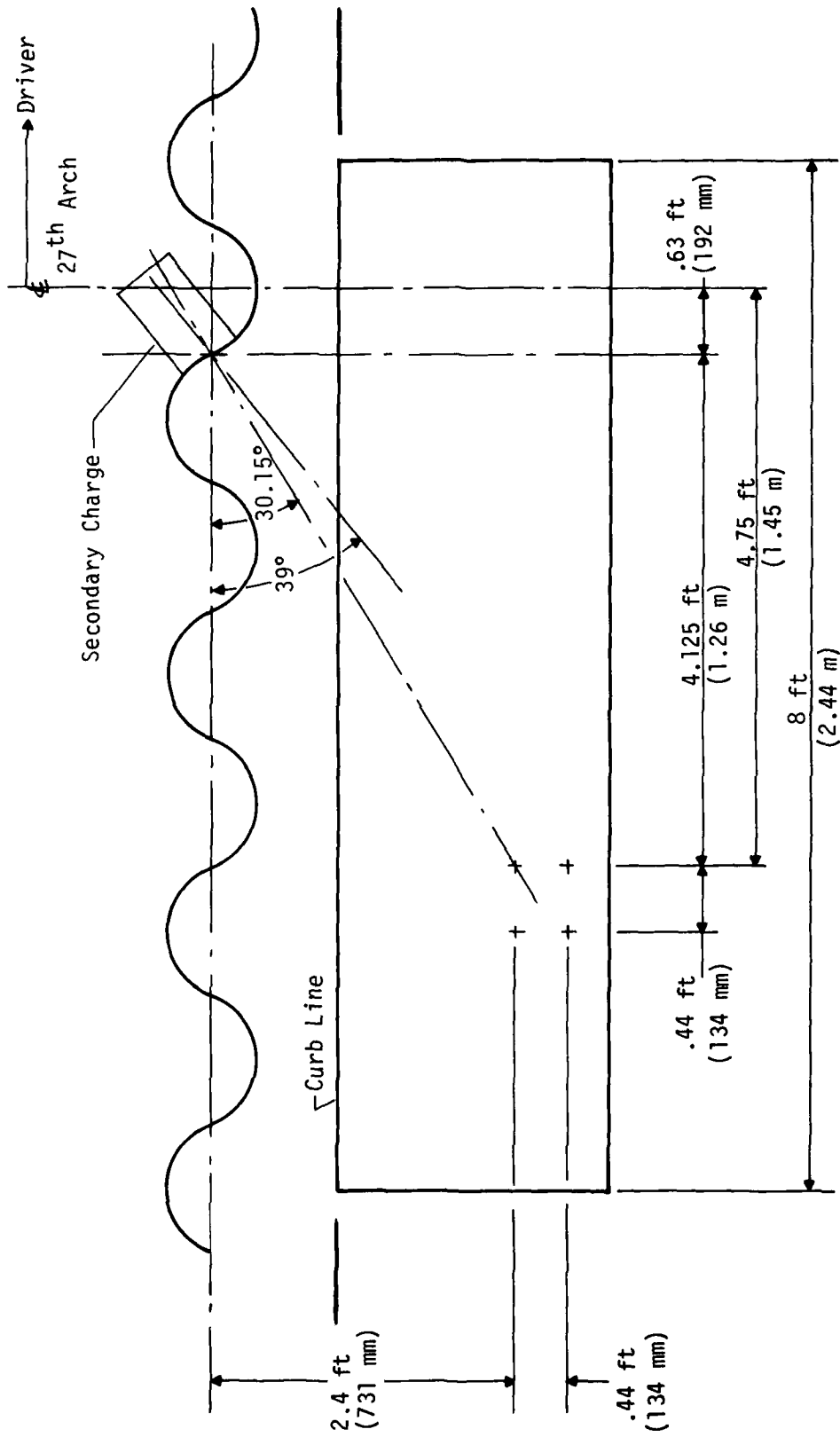


Figure 45. Test-Bed Layout, HH-S2

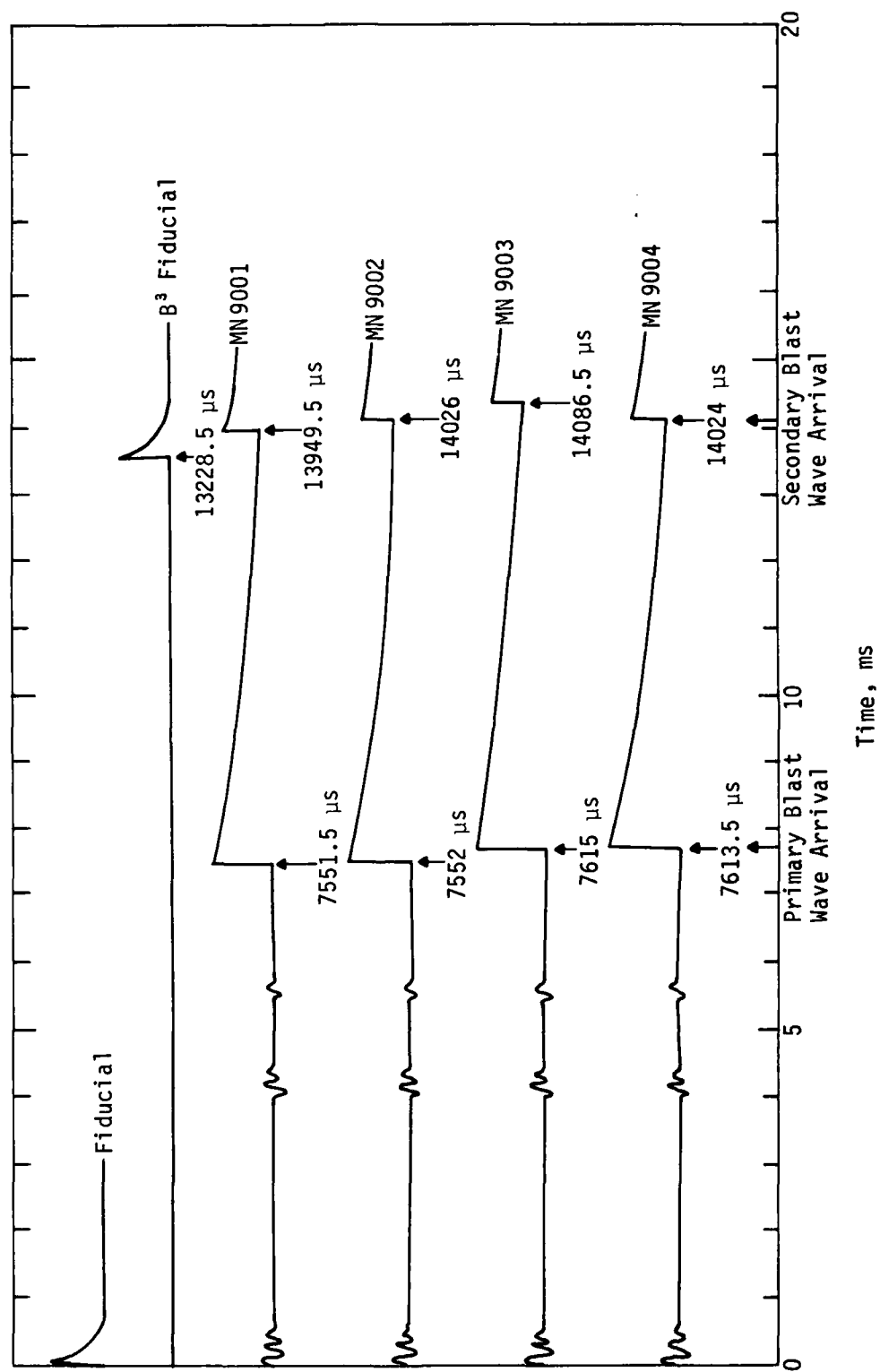


Figure 46. B³ Data HH-S2

The layout of the B³ experiment fielded on HH-S3 is shown in Figure 47. It is very similar to the HH-S2 experiment. The secondary charge was again detonated by means of a timed relay closure. The four detector signals and the two fiducial signals, in addition to being recorded separately (one channel per track), were also mixed together and recorded on one channel. This step was taken to obtain more precise timing by eliminating intertrack timing errors (track skew) from both record and playback operations.

The circuitry for this procedure is shown in Figure 48. The various pulses are discriminated by time division and polarity as shown in the timing diagram of the inputs and the output.

The data from the HH-S3 B³ experiment are shown in Figure 49. Here the secondary fiducial pulse was readily identifiable on the outputs of all the functioning detectors. Therefore, this point was used to synchronize the time. Unfortunately, the pressure gage on Measurement Number (MN) 9001 failed, but the three other gages functioned. It is suspected that this failure was caused by a break in the cable near the gage since the magnitude of the induced noise from the primary fiducial pulse is greater on this channel than the other channels and because no other signals are present.

Comparison of the separate data traces with the multiplexed data trace indicates time-base disparities of up to 5 ms or 8 percent. It seems most reasonable to attribute the higher confidence level to the multiplexed data, from which errors associated with plotter drum speed, tape playback speed, etc., are eliminated.

It was hypothesized that the anomalous results of the HH-S2 and HH-S3 B³ experiments were due to the turbulent flow in the area of the detector caused by corrugations in the walls. In order to verify this hypothesis, a B³ experiment was fielded on DSOT-I (a smooth-walled DABS test conducted at KAFB). The test-bed layout is shown in Figure 50. In this case, the secondary-charge canister was cast into the wall of the DABS facility. A square detector array was used as in HH-S2 and HH-S3. The secondary charge was detonated by the use of a timed relay closure.

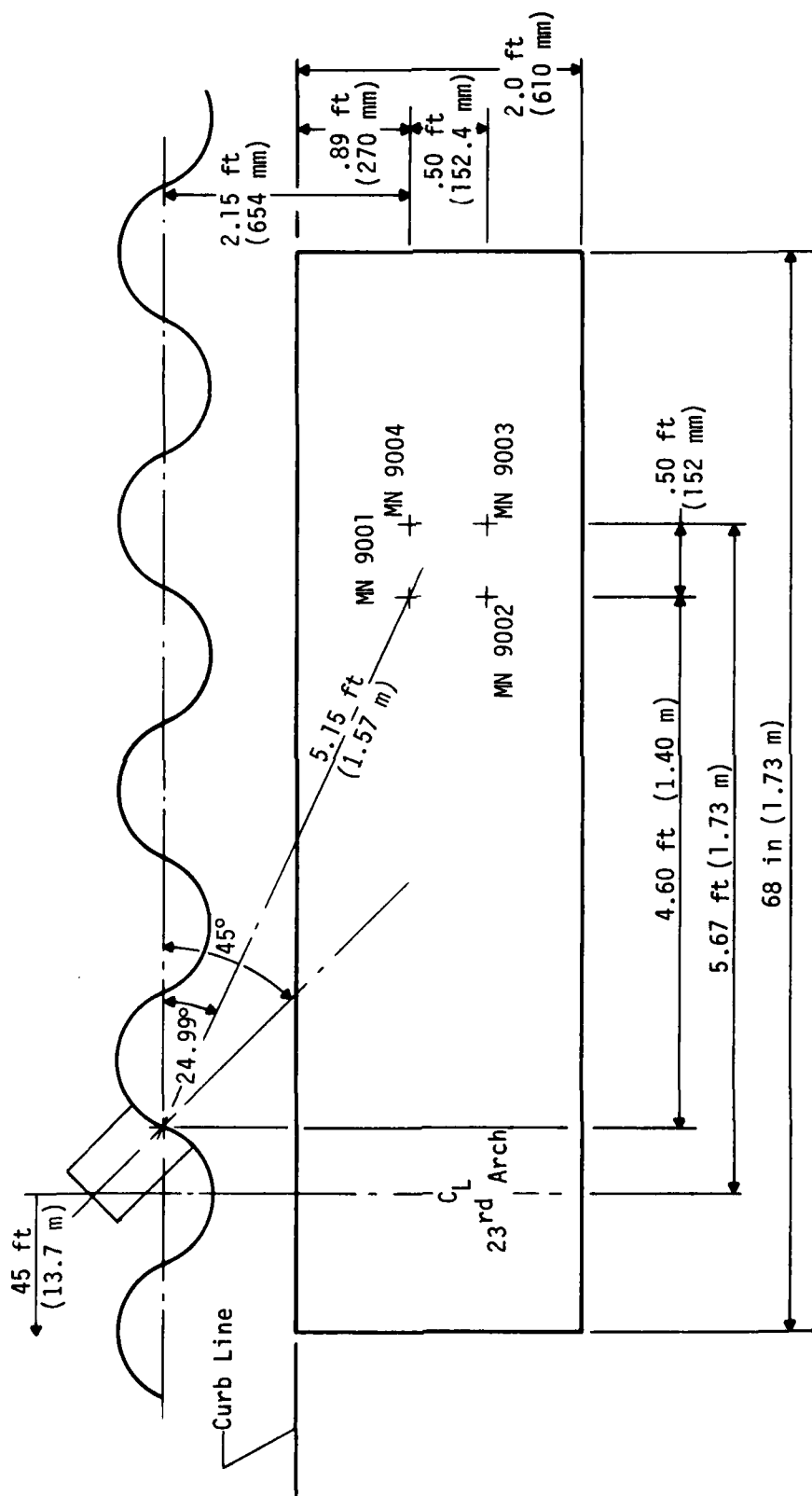


Figure 47. B³ Test-Bed Layout, HH-S3

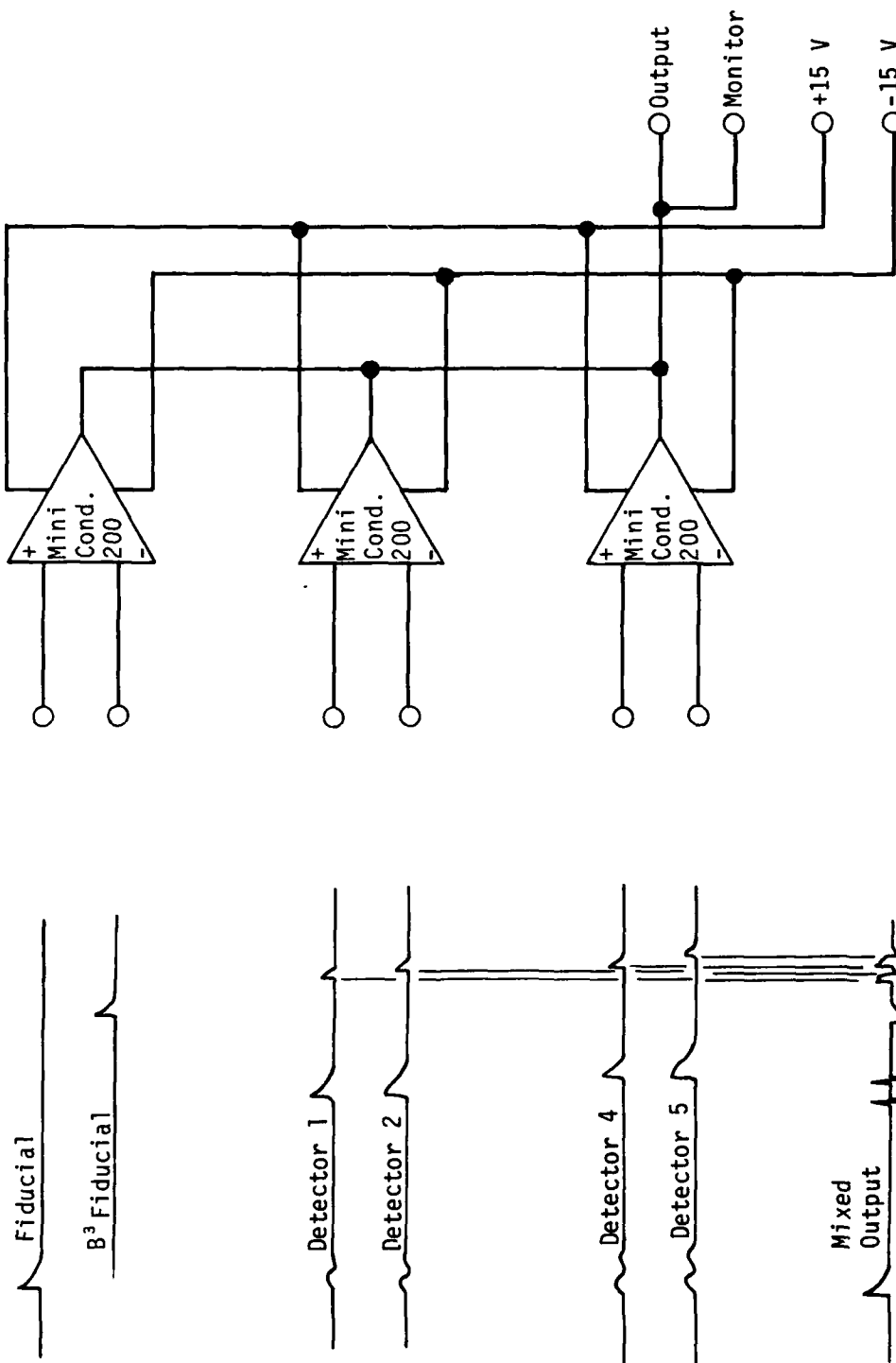


Figure 48. Schematic B³ Mixer

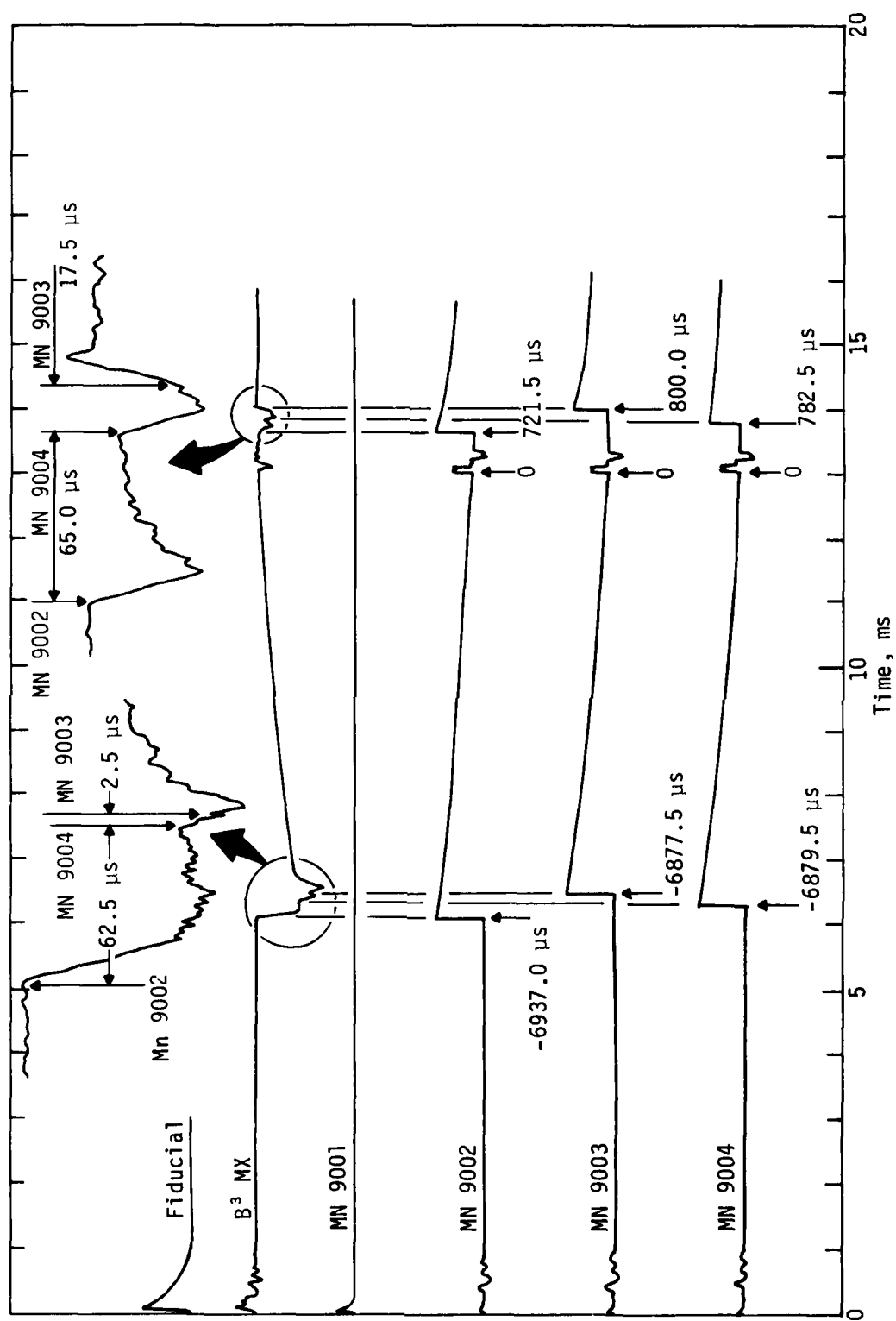


Figure 49. B³ Data HH-S3

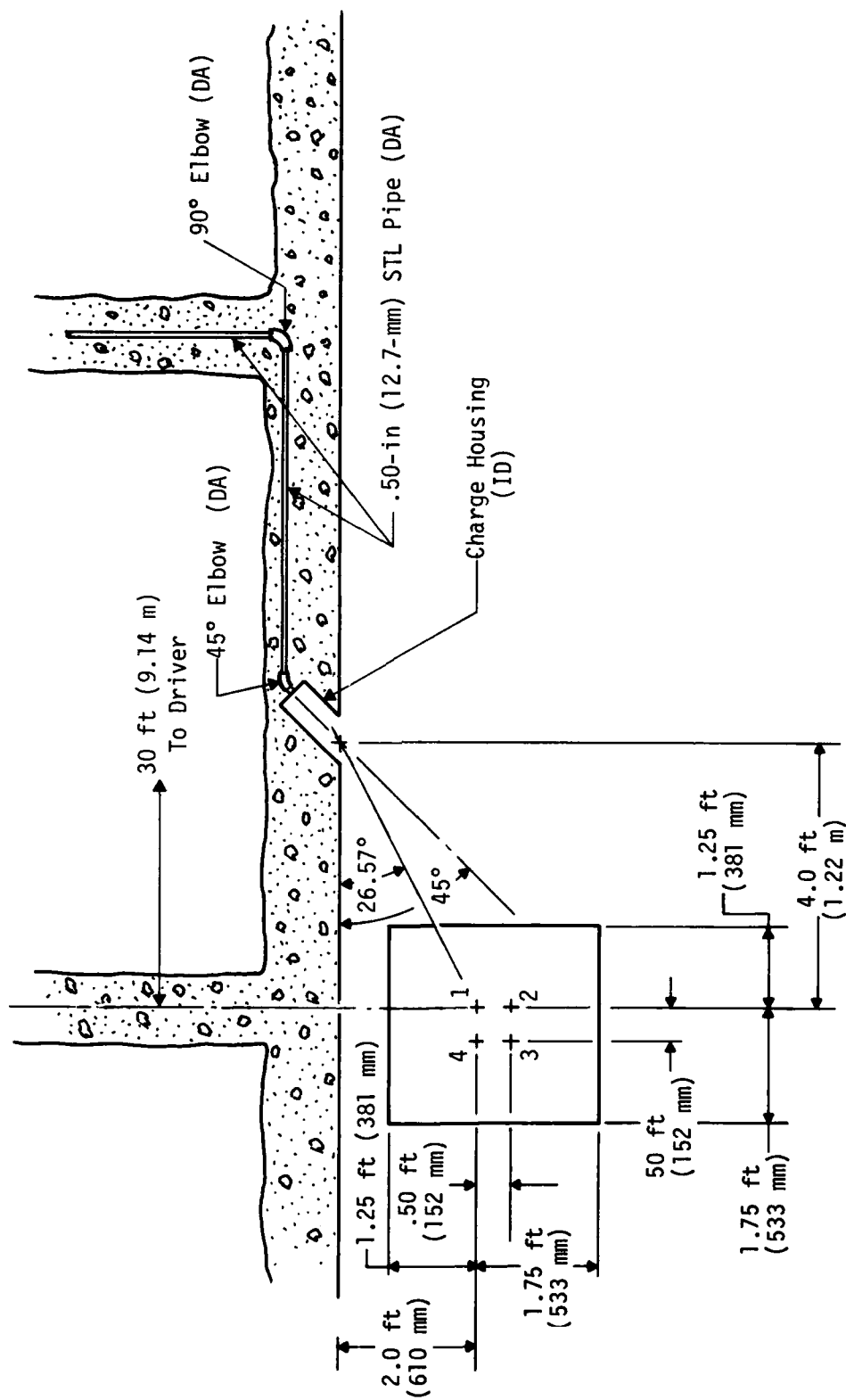


Figure 50. B³ Test-Bed Layout, DSOT-I Experiment

The data from the DSOT-I B³ experiment are shown in Figure 51. The excellent correlation of times should be noted as evidenced in the exact correlation of the pulses induced on the detector outputs by the fiducial pulses and by the close agreement between the TOA data for the primary blast wave and the positions of the detectors.

The results of DSOT 1 test of the B³ experiment indicated a secondary shock velocity of 1.75 mm/ μ s and a shock-crest particle velocity of 1.08 mm/ μ s. The secondary shock velocity can be normalized since the overpressure ratio of this shock with respect to the initial shock is known. In this case it was 6, or the secondary shock front Mach number was 2.36. This implies a sound speed in the detonation products of 0.74 mm/ μ s. Thus the Mach number of the flow was 1.46, a reasonable value.

From the other experiments, one could infer sound velocities much lower at ambient pressure and temperature and particle velocities much larger than possible. Thus in order for this experiment to succeed, a condition of low turbulence is required.

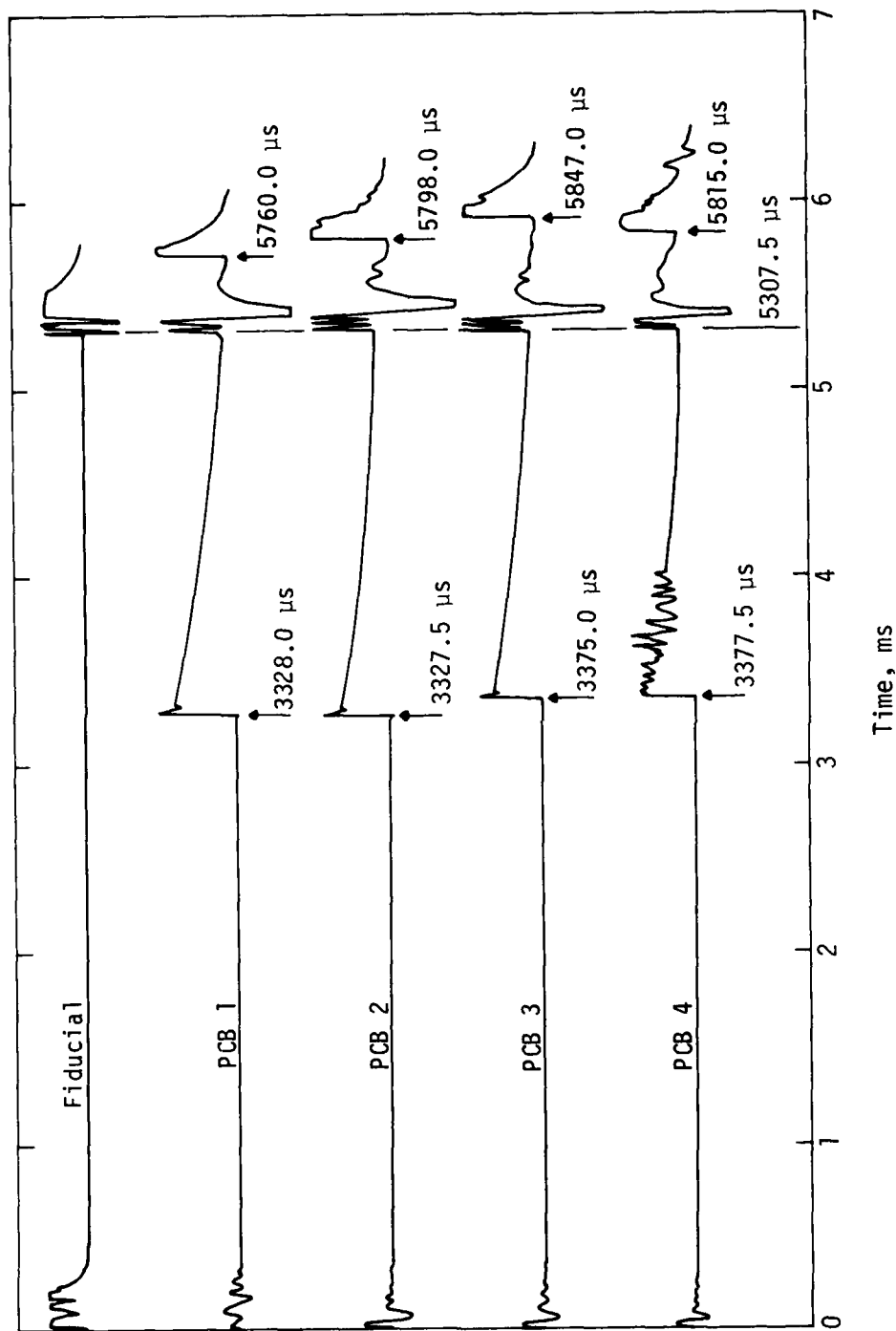


Figure 51. B³ Data, DSOT-I

SECTION V DRAG BODIES

ANALYSIS

The end-on drag of a blunt cylinder was measured in several of the DABS tests. These measurements were made in order to determine the flow Mach number and the dynamic pressure in the shock wave, which is comprised of airblast and high-explosive detonation products. The drag (D) is the total force on the end of the blunt cylinder minus the contribution due to the incident pressure integrated over the same surface. It is defined as being equal to:

$$D = 1/2 \rho u_p^2 C_D^A = 1/2 \gamma P M^2 C_D^A \quad (13)$$

where

- ρ = the density of the gas
- u_p = the particle velocity in the gas
- C_D = the drag coefficient
- γ = the ratio of the isobaric and isovolumetric specific heat of the gas
- P = the incident pressure
- M = the flow Mach number
- A = the cross sectional area.

The product $1/2 \rho u_p^2$ is the dynamic pressure (Q) in the flow.

Equation 13 and the drag properties of the blunt cylinder were the basis for the choice of this geometry to measure the drag. The nose coefficient of a blunt cylinder has been well characterized and is a known function of the Mach number (Ref. 2); namely:

$$C_D = 0.748 \quad M < 0.5 \quad (14)$$

$$M^2 C_D = 1.048 M^{2.487} \quad 0.5 < M < 2 \quad (15)$$

2. Zel'dovich and Raizer, *Physics of Shock Waves and High Temperature Hydrodynamic Phenomena*, Vol. 1, Academic Press, New York, 1966.

This empirical relationship shows that for Mach numbers of flow less than 2, there exist no great anomalies in the drag coefficient. This is not the case for some other geometrical shapes.

If one uses the relationships:

$$\frac{u_s - u_p}{u_s} = \frac{(\gamma + 1) + (\gamma + 1) A}{(\gamma + 1) + (\gamma + 1) A} \quad (16)$$

$$u_s = c_0 \left[\frac{(\gamma - 1) + (\gamma + 1) A}{2\gamma} \right]^{1/2} \quad (17)$$

$$\left(\frac{u_s - u_p}{c_1} \right)^2 = \frac{(\gamma - 1) + (\gamma + 1) A}{2\gamma} \quad (18)$$

where

- u_s = Shock velocity
- A = Overpressure ratio in the shock
- c_0 = Undisturbed speed of sound
- c_1 = Local sound speed in the shock

then the Mach number of flow $\frac{u_p}{c_1}$ can be determined.

The procedure can be simplified by noting that in the limit of strong shock $\frac{1}{A} \ll 1$ and:

$$\frac{u_s - u_p}{c_1} = \left[\frac{(\gamma - 1)}{2\gamma} \right]^{1/2} \quad (19)$$

Thus, for the case of shocked air one can show (using the above equations and assuming a γ of 1.4) that the Mach number of flow for peak pressures below 4 to 5 MPa (582 to 727.5 lb/in²) is always less than 2.

Peak incident pressures of 4 to 5 MPa (582 to 727.5 lb/in²) were exactly the pressures used in the DABS to test structures. Thus, for this application, a blunt cylinder is an ideal drag body.

The design of the principal drag body used is given in Figure 52. It shows a 2.5-in (63.5-mm) diameter blunt cylinder capped by a 0.062-in (1.57-mm) thick copper diaphragm. The purpose of this diaphragm is to contain a cavity filled with an incompressible fluid (glycerin). The pressure in the fluid is measured and is interpreted to be the average pressure, P_G ; or the total force is considered to be equal to $P_G A$.

There are two obvious possible sources of error in the measurement. These are the effect of the diaphragm and of the perturbation of the rim used to contain the liquid.

The approach to the study of the first of these possible effects is to determine if the copper diaphragm would pick up a significant portion of the drag load on the front of the cylinder. A calculation was done to determine the pressure necessary to push the copper diaphragm far enough to bottom out in the 0.125-in (3.18-mm) deep cavity (Ref. 3). This was determined to be approximately 0.2 MPa (29.1 lb/in²) overpressure. Since the peak drag pressures were expected to be in the range of 15 to 30 MPa, (2175.5 to 4351 lb/in²) this effect was felt to be negligible.

The second of these possible effects is the effect of the lip used to contain the glycerin. This 0.125-in (3.18 mm) wide lip could not be made any thinner and still be expected to withstand the hoop stress induced by the blast loading. This requirement for containment uses a significant portion of the area (19 percent) of the nose of the cylinder. In order to correct for this fact, the results of an empirical study by Holder and Chinneck (Ref. 4) were used. They measured the pressure distribution across the nose of a blunt cylinder and other bodies of revolution in a supersonic wind tunnel. The results of this study, showing significantly lower pressures at the edge of the cylinders, were used to correct the data. This correction was a 4-percent reduction in the measured drag pressure (P_D). Thus, Equation 13 may be rewritten as:

$$\frac{D}{A} = P_D = 0.96(P_G - P) = QC_D = 1/2\gamma PM^2 C_D \quad (20)$$

3. Timeshenko and Woinowsky-Krieger, *Theory of Plates and Shells*, McGraw Hill Book Company, Inc., New York, 1959.
4. D. W. Holder and A. Chinneck, *The Aeronautical Quarterly*, Volume IV, February, 1954, p. 317.

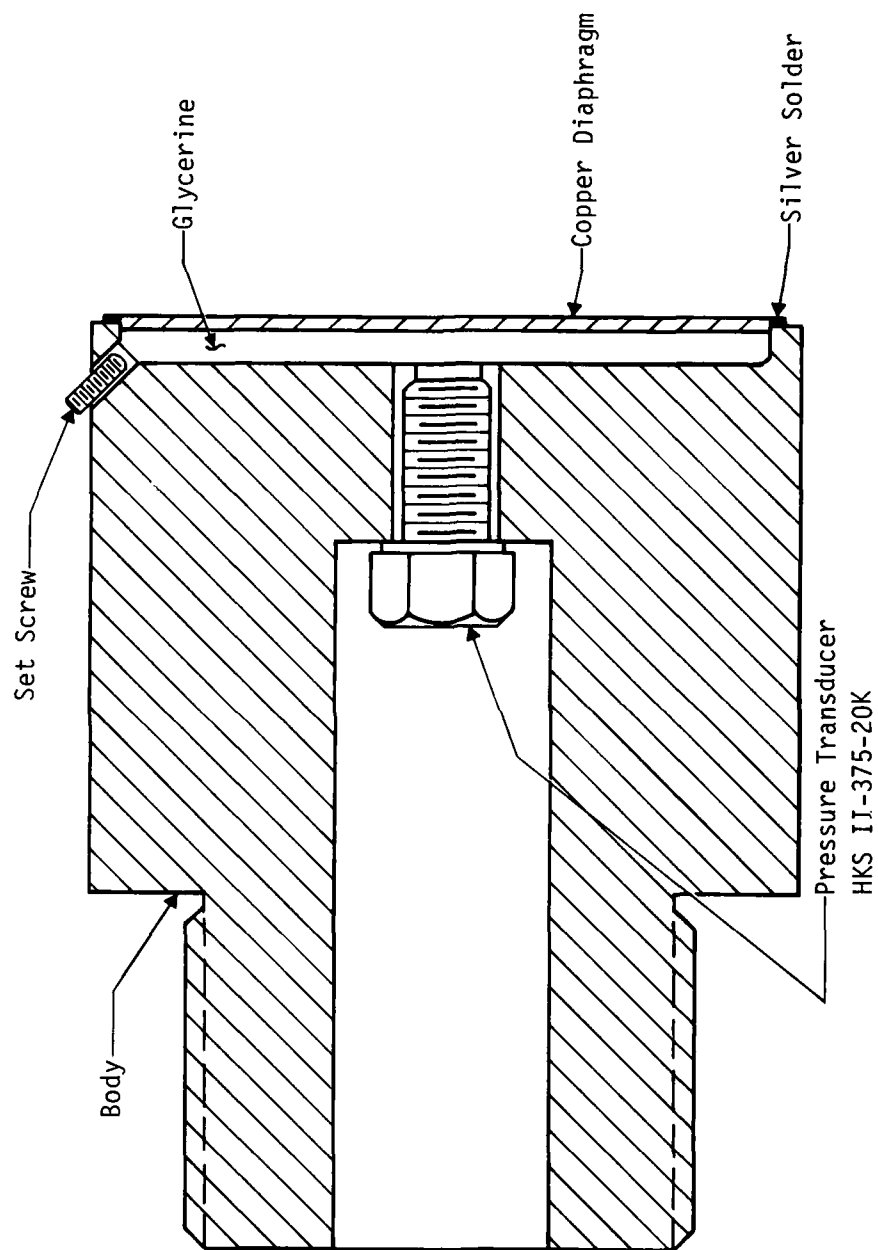


Figure 52. Drag Body Assembly

This type of drag body was fielded in two DABS events, HH-S2 and HH-S3. They were mounted on the end of appropriately sized probes attached to wings in the tunnels. There were two in HH-S2 and three in HH-S3. The results of these experiments are shown in Tables 4 and 5. The range referred to is the distance from the explosive driver. The time is the length of time after detonation. The value of γ used was 1.32. The incident or side-on pressures used were taken from other measurements in the vicinity of the drag body. These results agreed favorably with those inferred from the stagnation pressure measurements.

With one exception, all of the gages survived this rather harsh environment. The one exception was the drag body closest (14.5 ms) to the explosive driver on HH-S3. It ceased to function approximately 2 to 3 ms after shock arrival. Posttest inspection revealed that it had been impacted by a piece of debris which ruptured the copper diaphragm.

The second type of drag body used is shown in Figure 53. It contains a fully moment-compensated load cell. That is to say, the Wheatstone bridge contained eight elements, two in each arm. These two elements were placed 180 deg apart inside the load cell. This arrangement gave bending-moment compensation.

There was also a total pressure measurement made at the center of the nose of the blunt cylinder. This was a Kulite pressure gage covered with a Model V AFWL debris shield.

The load cell was calibrated in a uniaxial load-testing machine and loaded up to 133 kN. It was linear and had a sensitivity to pressure on the blunt nose of about 225 μ V/V-MPa.

Two of these units were placed in test event DABS-IIIA, an experiment conducted at McCormick Ranch on KAFB. Figure 54 shows one of the outputs of these drag bodies. The peak pressure indicated is reasonable and agrees with stagnation pressures at the same location. However, the ringing of approximately 1 kHz and a large negative offset make the utility of the measurement minimal.

TABLE 4. DRAG BODY MEASUREMENT IN HH-S2

Range, m	P, MPa	P _G , MPa	Time, ms	M	Q, MPa
22	4.20	18.50	9.80	1.87	9.66
	3.00	7.50	11.20	1.34	3.57
	2.00	3.75	14.00	1.08	1.54
	1.00	2.00	16.80	1.14	0.86
	1.30	1.75	18.00	0.74	0.48
	1.00	2.50	26.00	1.34	1.19
36	3.90	15.00	17.00	1.74	7.77
	2.00	6.40	20.00	1.57	3.24
	1.50	4.00	20.80	1.40	1.94
	1.00	1.50	27.00	0.86	0.49
	0.80	1.00	32.00	0.65	0.23

TABLE 5. DRAG BODY MEASUREMENT IN HH-S3

Range, m	Time, ms	P_G , MPa	P, MPa	M	Q, MPa
14.500	6.0	28.0	6.30	1.88	14.63
	7.0	24.0	4.00	2.18	12.54
23.708	10.5	21.0	5.93	1.66	10.79
	12.0	10.2	3.30	1.53	5.13
	14.0	$\frac{8.0}{9.0}$	2.18	$\frac{1.69}{1.80}$	$\frac{4.13}{4.69}$
	16.0	9.5	1.75	2.08	4.97
43.700	22.0	15.0	2.75	2.08	7.85
	24.0	6.0	1.95	1.53	3.02
	26.0	3.0	1.65	1.05	1.21
	28.0	5.0	1.20	1.81	2.60
	30.0	3.0	1.05	1.46	1.48

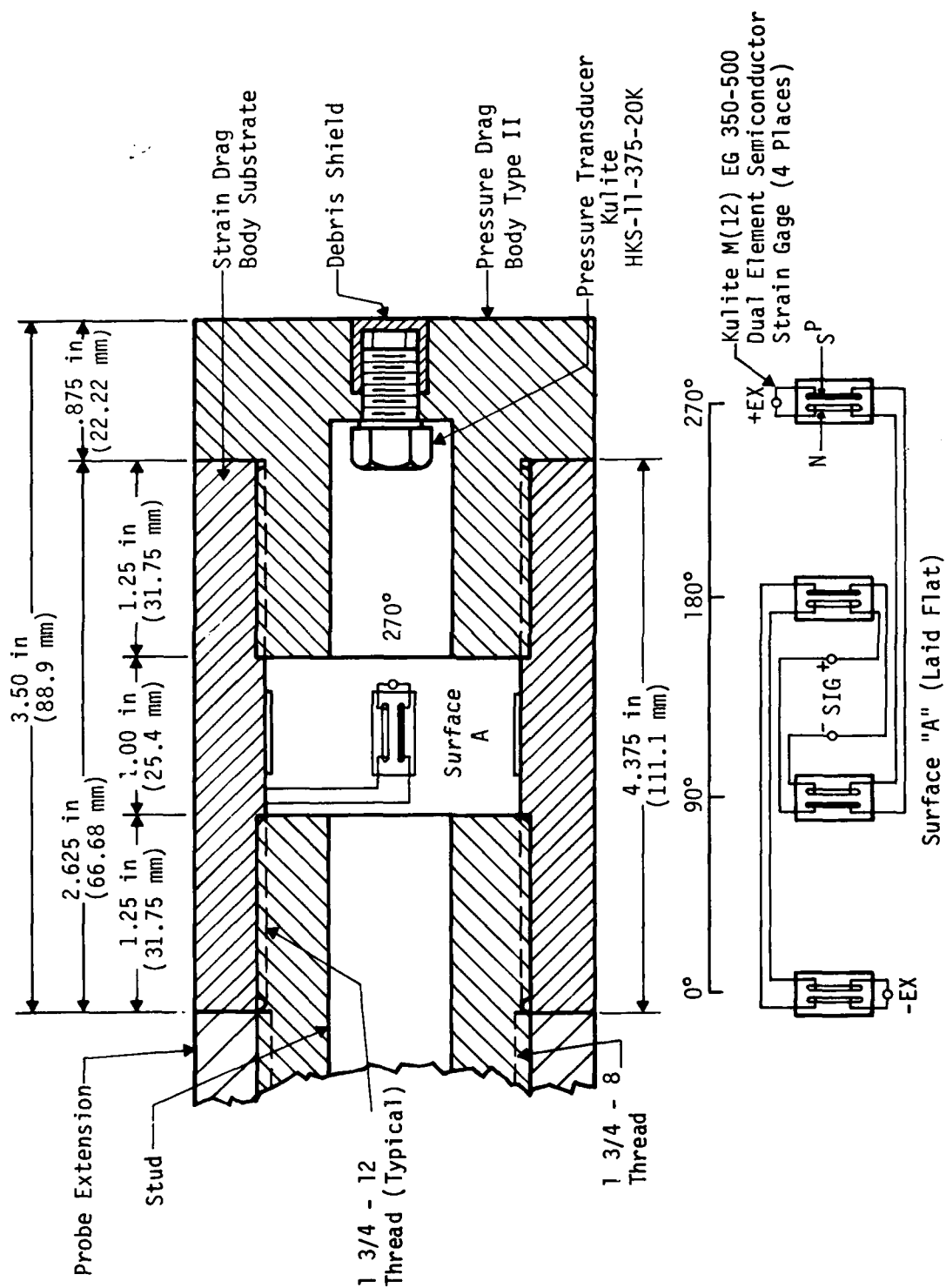


Figure 53. Strain/Pressure Drag Body Assembly, DABS-III A5

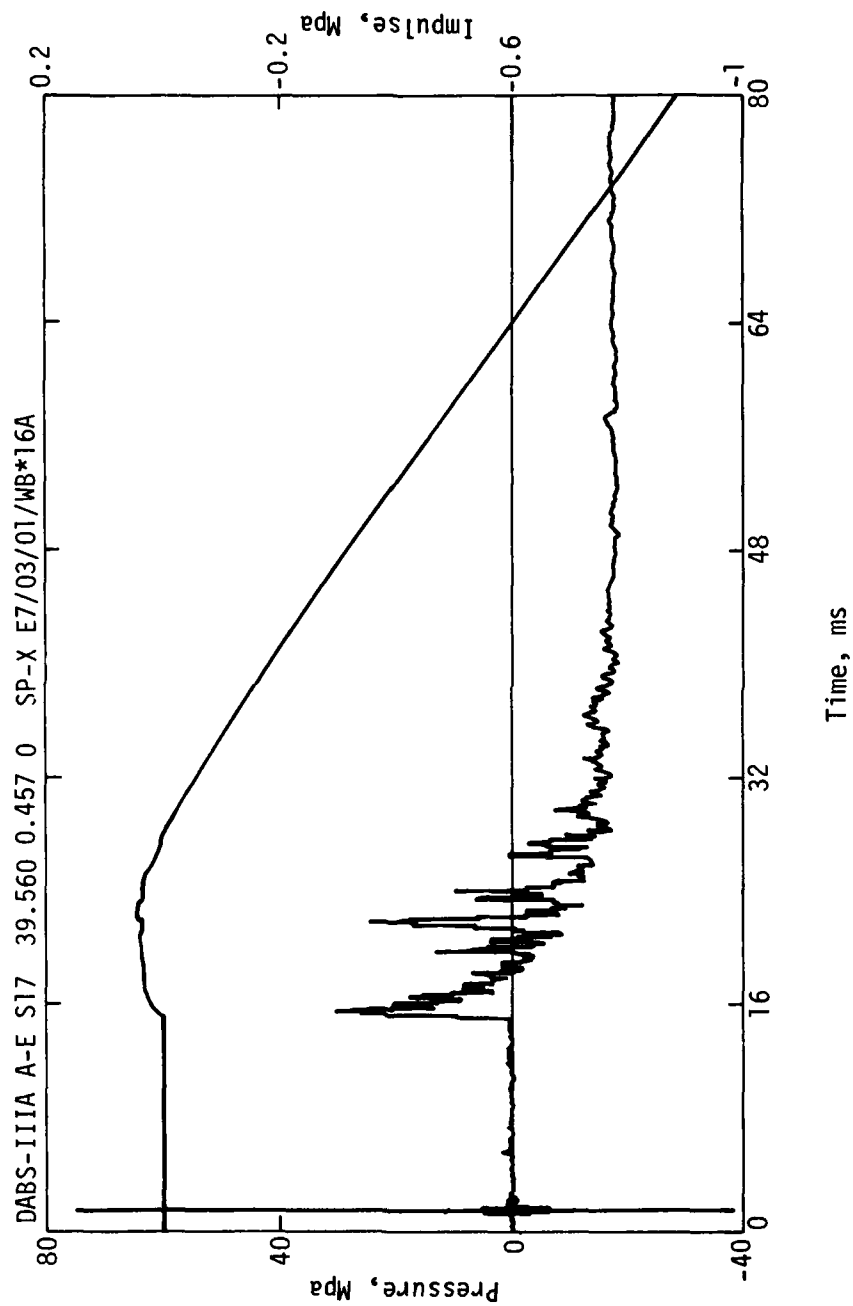


Figure 54. Load Cell Drag Body Response

The ringing is most likely due to ringing in the probe on which the load cell was mounted. The cause of the negative offset is unknown and is, in fact, quite confusing. The negative offset indicates residual tension at the location of the strain gage element. A possible explanation is that the shock induced by an effective annealing of the material and the resulting release of a residual compressive stress in the material put the strain gages under tension. This hypothesis is partially confirmed by the posttest calibration of the load cell drag body (Fig. 55), which showed increased ductility in the load cell.

CONCLUSIONS AND RECOMMENDATIONS

The measurement of blunt cylindrical drag in environments in which the Mach numbers of flow range between 0.5 and 2 is an extremely useful experiment. It gives the parameter of the dynamic pressure and Mach number of the flow in a simple manner. That is to say that the measurement may be reduced in a manner easier than the iterative technique required for the reduction of Pitot tube measurements.

The glycerin drag body performed quite well in this set of experiments and gave results that agreed with the Pitot tube measurements in all the DABS experiments. The load cell drag body read the peak drag pressure adequately. However, the subsequent offset and ringing negated the value of the measurement. This method needs to be redesigned before it is fielded again.

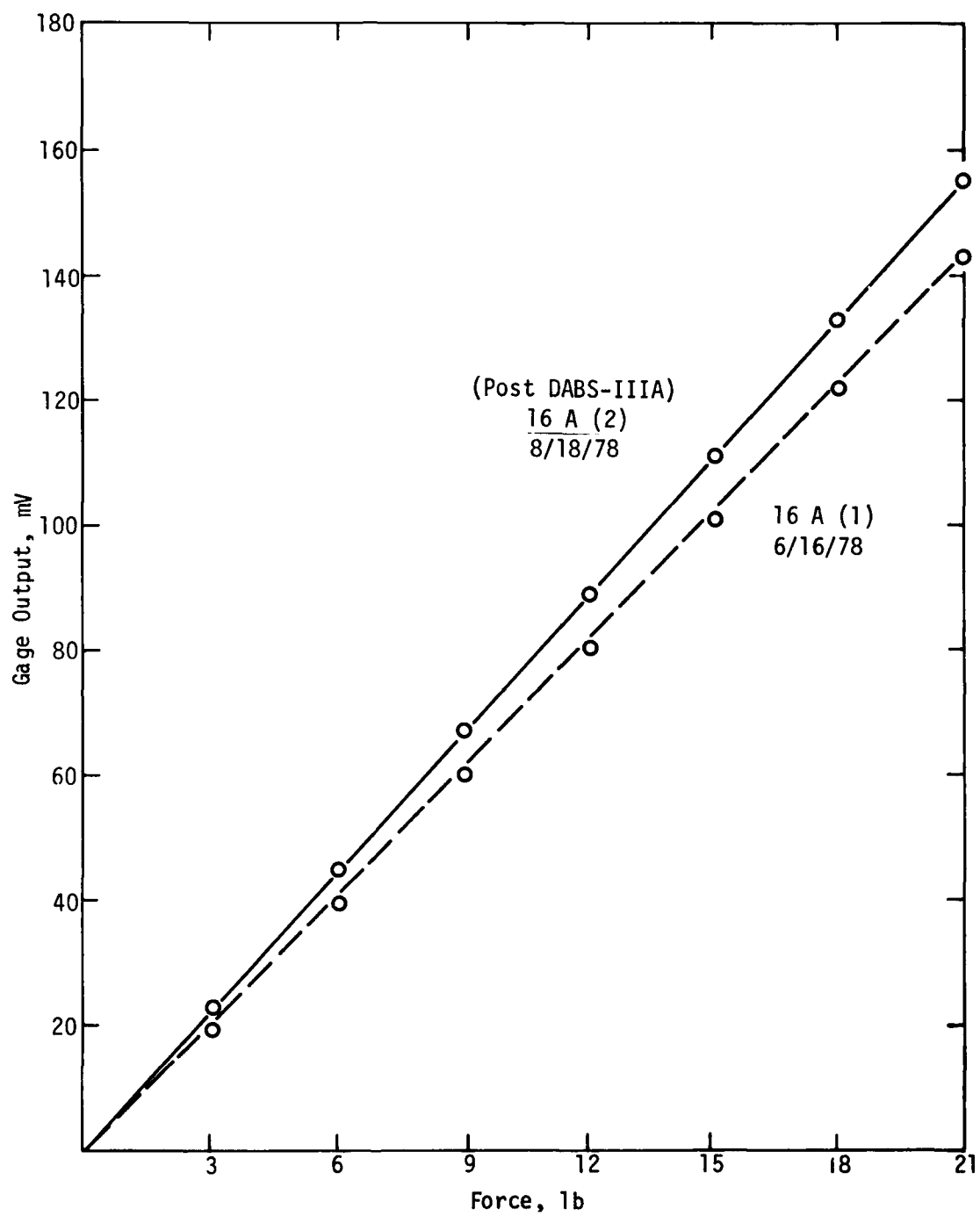


Figure 55. Pre- and Posttest Calibration of a Load Cell Drag Body

SECTION VI

DRIVER CHAMBER MOTION MEASUREMENTS

Motion of the driver chamber induced by the high-explosive charge detonation is directly related to the pressure generated inside the chamber by the explosion. Accordingly, the driver chamber on the DABS IIIA test was instrumented to obtain measurements of rigid-body displacement of the back wall of the driver chamber, particle and shock velocities in the back wall, and stress in the back wall. These measurements and their purposes are indicated in Table 6, and the layout of the measurements is shown in Figure 56.

TABLE 6. DRIVER MOTION MEASUREMENTS

Measurement Number	Purpose	Type of Instrumentation
TOA 1	Shock propagation in back wall by time-of-arrival (TOA) of shock front	Piezoelectric crystal "pins"
TOA 2	Rigid-body motion of back wall	Progressive break wire gage
MIPV 1	Particle velocity in back wall	Mutual Inductance Particle Velocity (MIPV) Gage
ASMP 1	Particle velocity in back wall	Axially Symmetric Magnetic Probe (ASMP)
MG 1	Stress in back wall	Manganin Stress Gage
MG 2	Stress in back wall	Manganin Stress Gage

RIGID-BODY MOTION OF CHAMBER BACK WALL

The gross motion of the back wall of the driver chamber was recorded by means of a progressive-break wire gage. The gage was suspended by bungee cords from the top of a section of 24-in (610-mm) diameter sonotube, as indicated in Figure 56. It was located directly behind a 0.50-in (12.7-mm) steel anti-spall plate which was cast into the wall. A section through the gage is shown in Figure 57. The body of the gage is a standard concrete test cylinder 6 in (152 mm) in diameter by 12 in (305 mm) long with plastic pipe sleeves cast into it.

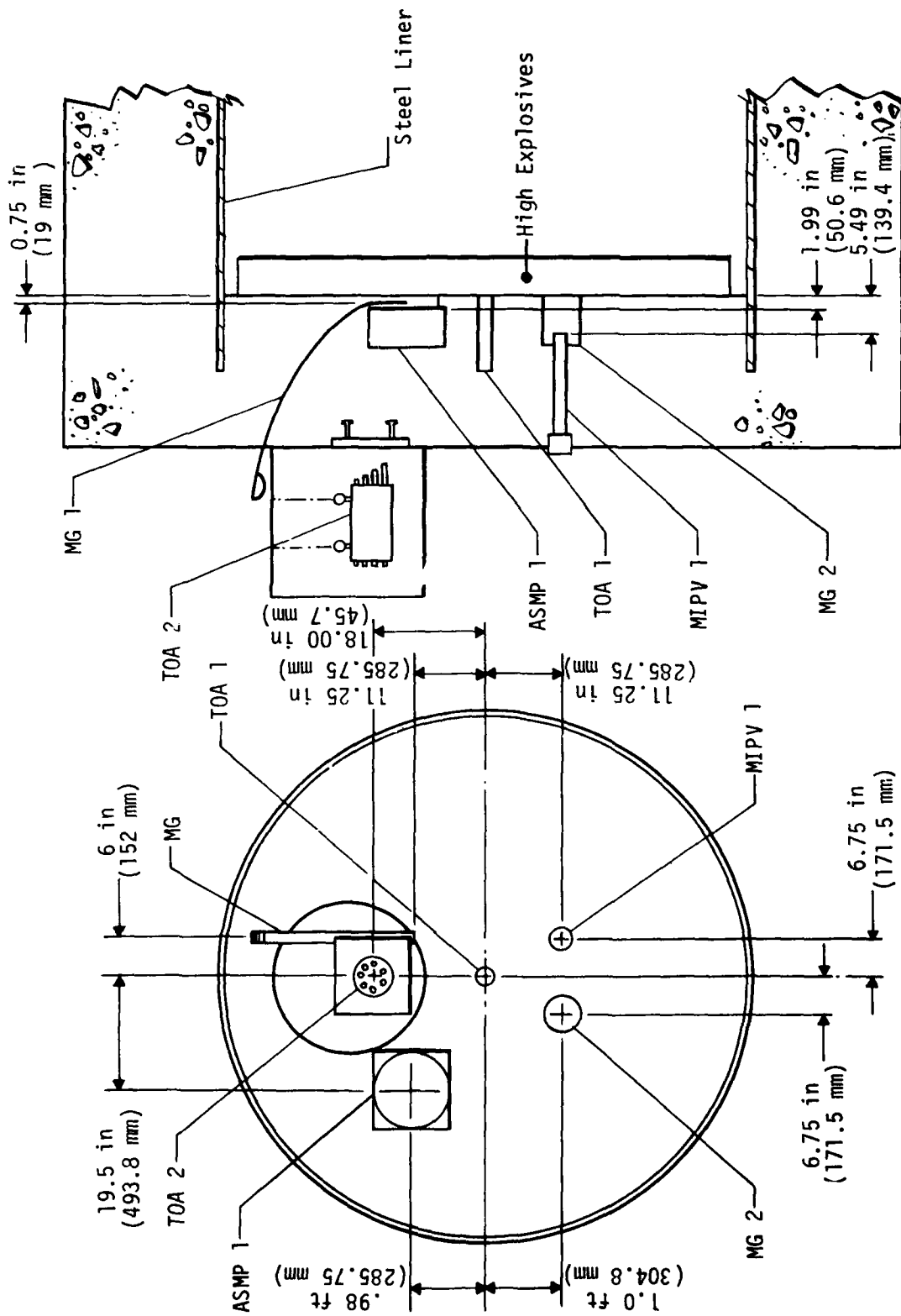


Figure 56. Developmental Instrumentation Layout - Driver, DABS-III A

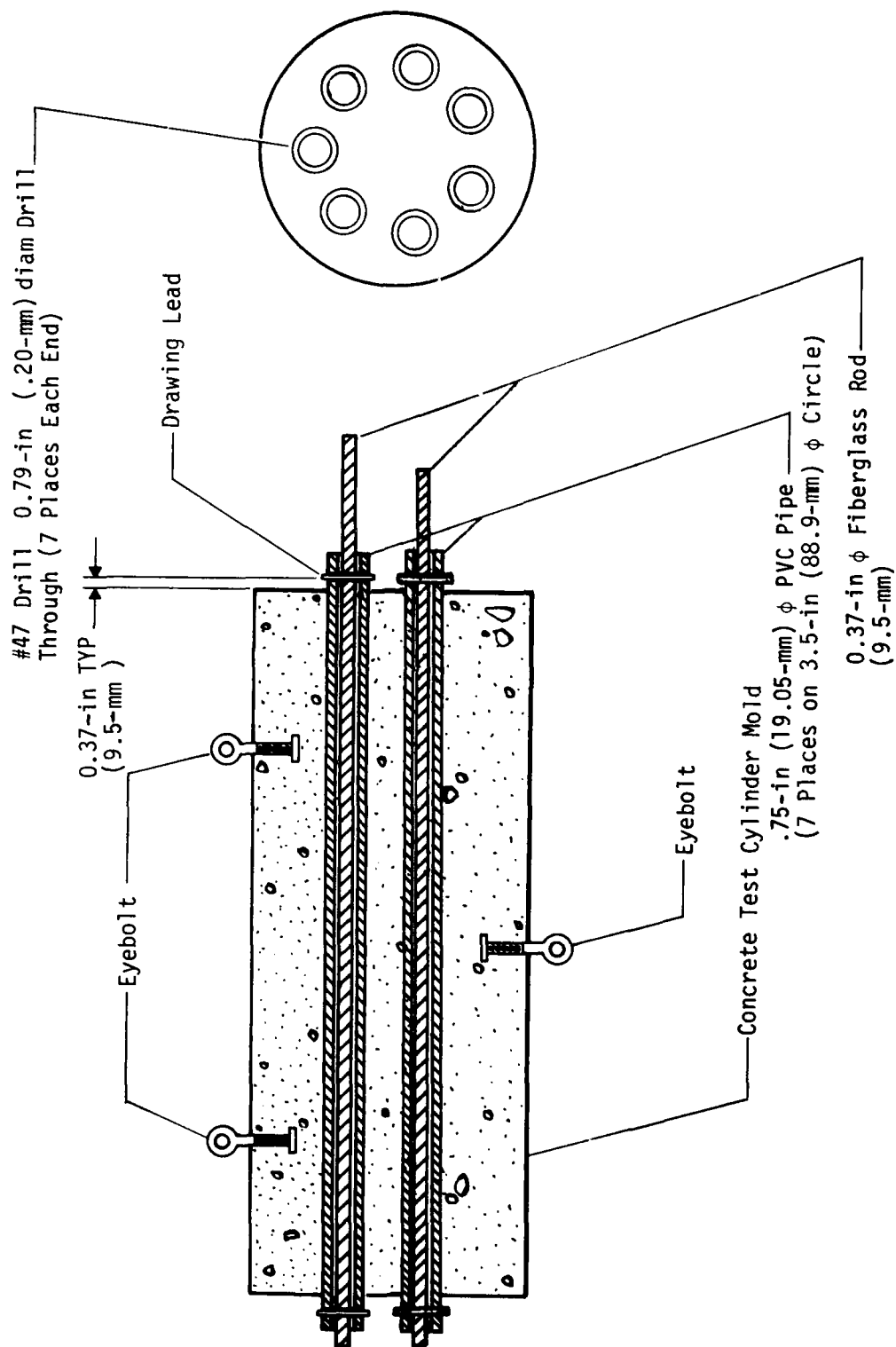


Figure 57. Gage Body - TOA Gage 2 DABS-111A

The break "wires" (drafting pencil leads in this application) pin 0.39-in (9.9-mm) diameter fiberglass rods to the sleeves. When the end of each rod is struck by the antispall plate, the lead which pins it to its sleeve is severed. The lengths of the rods are staggered at convenient intervals so that the motion of the antispall plate (and thus the motion of the back wall of the driver chamber) is described by the times of the breakage of the leads.

The breaking of the leads was recorded by the instrumentation system shown in Figure 58. The breakage of each lead results in a step in the signal at the recording van, according to the relation:

$$V_{out} = \frac{V_{in}}{R_{eff} + R_1} \quad (21)$$

where

$$\begin{aligned} V_{out} &= \text{Signal voltage, volts} \\ V_{in} &= \text{Excitation voltage, volts} \\ R_1 &= \text{Ballast resistance, ohms} \\ R_{eff} &= \text{Effective resistance of gage, ohms} \end{aligned}$$

R_{eff} depends on how many leads have been broken, according to:

$$R_{eff} = (7 - i) \frac{R_2 R_3}{R_2 + R_3} + i(R_2) \quad (22)$$

where

$$\begin{aligned} R_2 &= \text{Resistor shunted by lead} \\ R_3 &= \text{Resistance of lead} \\ i &= \text{Number of leads that have been broken} \end{aligned}$$

In the present application, $V_{in} = 45 \text{ V}$, $R_1 = 10 \text{ k}\Omega$, $R_2 = 150 \Omega$ and $R_3 = 10 \Omega$. These data yield the following voltages:

Impact No.		0	1	2	3	4	5	6
Break No. (i)	0	1	2	3	4	5	6	7
V_{out}	0.43	0.91	1.5	2.1	2.7	3.2	3.8	4.3

No particular problems were encountered in fielding this instrument on DABS-IIIA. The data trace from this gage is shown in the composite data plot (Fig. 59). The data from the oscilloscope photo and the tape are plotted in

AD-A090 531

NEW MEXICO UNIV ALBUQUERQUE ERIC H WANG CIVIL ENGINE--ETC F/G 18/3
DYNAMIC AIRBLAST SIMULATOR (DABS) INSTRUMENTATION DEVELOPMENT. --ETC(U)
JUN 80 W R EDGEL, N P BAUM F29601-76-C-0015

UNCLASSIFIED

AFWL-TR-79-155

NL

2 OF 2

AD
ALMA-HST

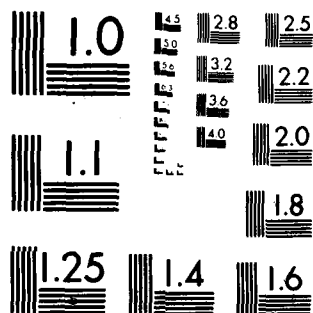
END

DATE

FILED

11 80

DTIC



MICROCOPY RESOLUTION TEST CHART
NATIONAL BUREAU OF STANDARDS-1963-A

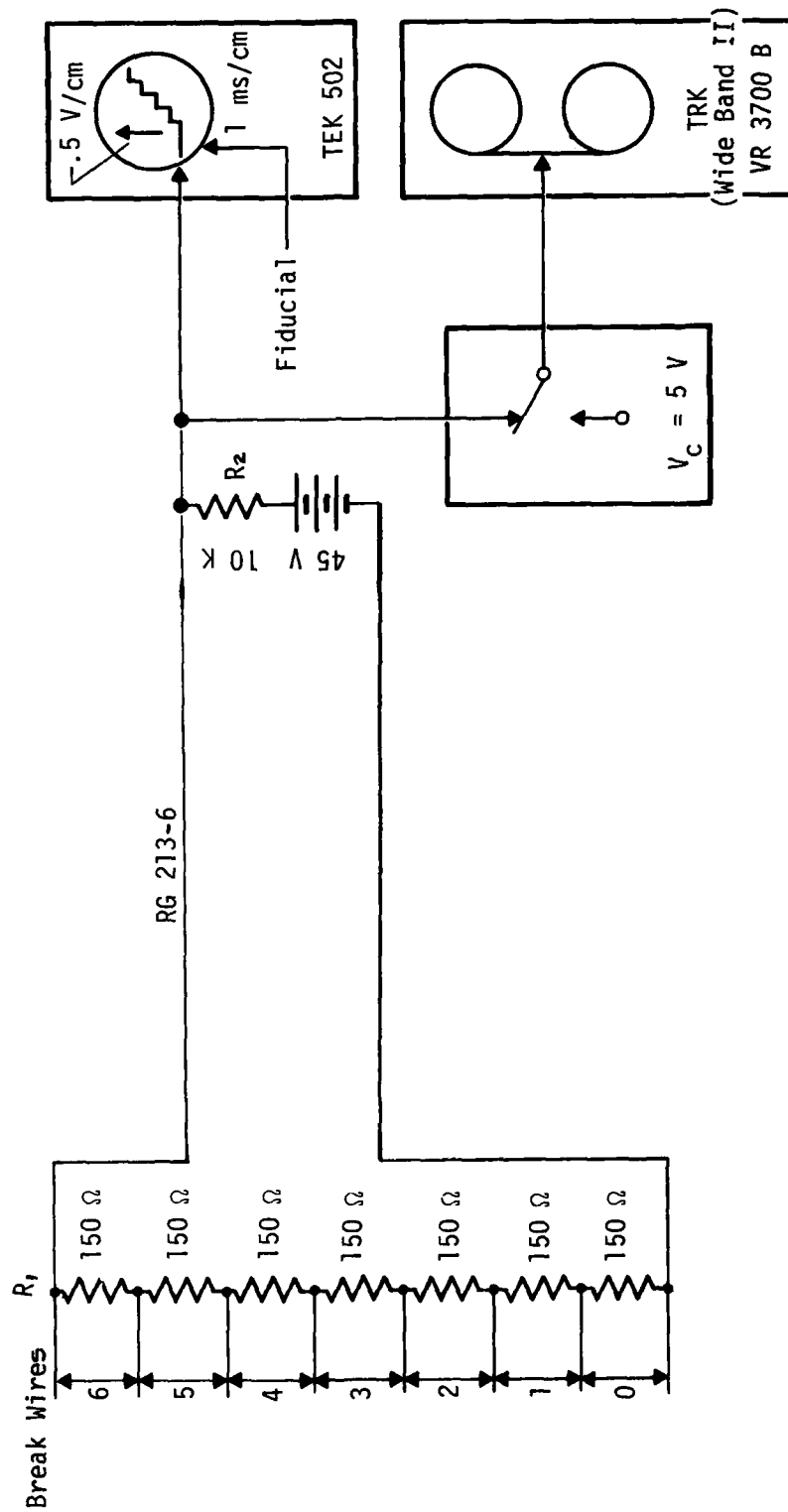


Figure 58. TOA 2 Instrumentation DABS-IIIA

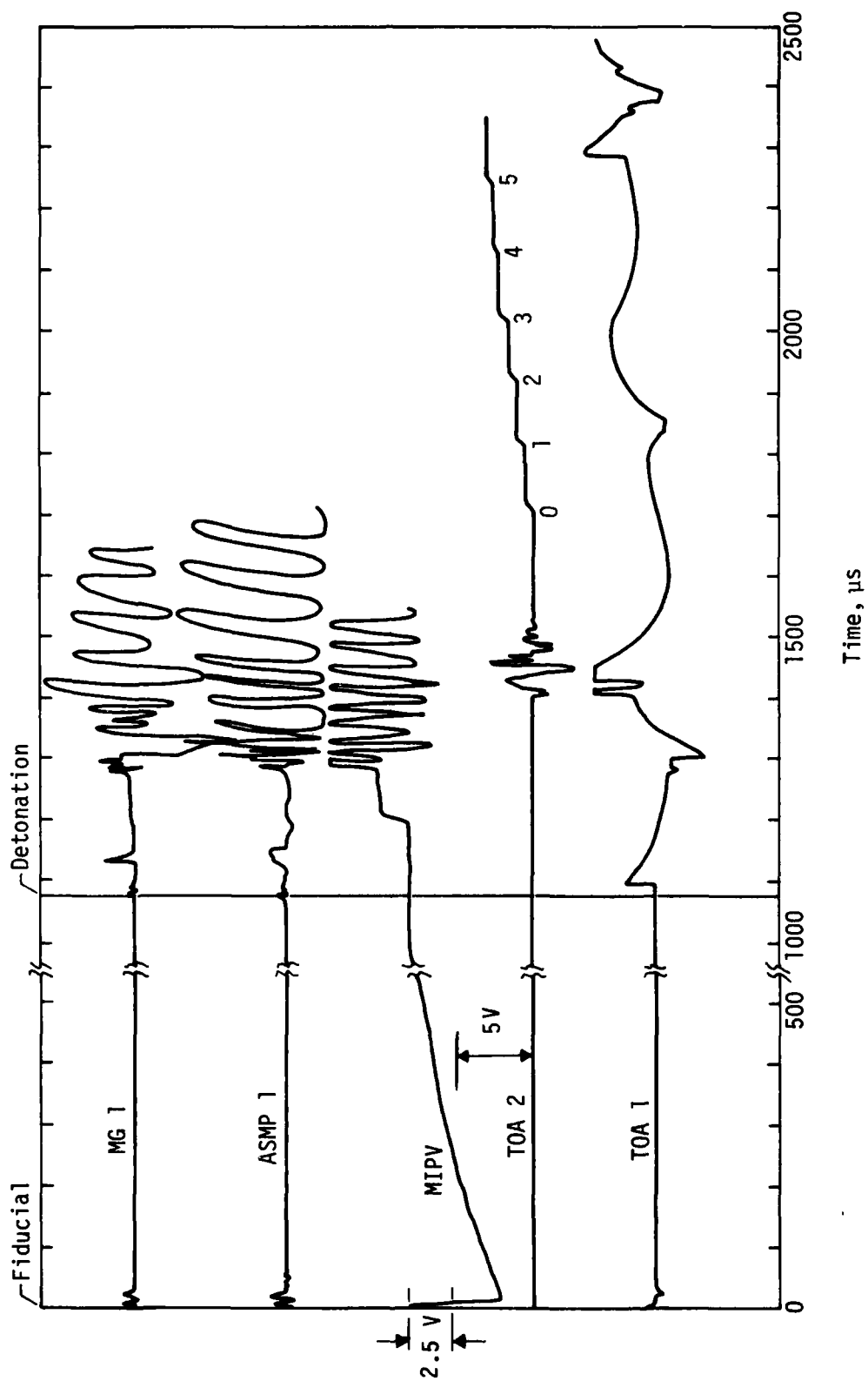


Figure 59. DABS III-A Driver Motion Measurements

Figure 60. They indicate back-wall velocities of 805 ft/s ($0.245 \text{ mm}/\mu\text{s}$) for the tape data and 740 ft/s ($0.226 \text{ mm}/\mu\text{s}$) for the photo data. On the basis of visual resolution, the tape data (2 percent) are much better than the oscilloscope data (10 percent). Therefore the tape data are regarded as more nearly correct.

SHOCK PROPAGATION IN CHAMBER BACK WALL

A piezoelectric crystal pin TOA gage was used to measure shock propagation velocity in the chamber back wall. The gage used is shown in Figure 61. Individual pins were taped to a plexiglass rod, and then the assembly was potted in a cardboard cylinder with "clearcast resin." The gage was installed as indicated in Figure 56; but during the pouring of the chamber, it became displaced about 45 deg from the principal axis of the DABS. This displacement ruined the measurement as far as velocity of the shock wave was concerned, but a TOA point at the front surface of the wall was obtained. The instrumentation for this measurement is shown in Figure 62. A diode-mixing and pulse stretcher circuit was used at the test bed to send all the pulses from the individual pins to the van on one signal line and to reduce the amplitude (nominally 40 V) and increase the (half amplitude) duration (nominally $10 \mu\text{s}$) to 5-V amplitude and $0.5\text{-}\mu\text{s}$ duration. Unfortunately, the off-axis orientation so "smeared" or prestretched the pulses that the pulse stretcher smeared the pulses beyond discrimination as shown in the composite data plot, Figure 59. The only usable data is the first positive pulse, which represents the TOA of the shock wave at the front surface of the chamber wall, $+1090 \mu\text{s}$. This is a reasonable time since detonation-induced noise on several of the other channels occurs at $+1060 \mu\text{s}$.

PARTICLE VELOCITY IN CHAMBER BACK WALL

Particle velocity in the back wall of the chamber was measured at two points with two different types of particle velocity gages; a Mutual Inductance Particle Velocimeter (MIPV) at a point 6 in (152.4 mm) behind the front surface and an Axially Symmetric Magnetic Probe (ASMP) at a point 2 in (50.8 mm) behind the front surface. Both gages operate on the principle of time variant magnetic induction, whereby particle motion produces a changing magnetic field through a loop, inducing a voltage in the loop which is related

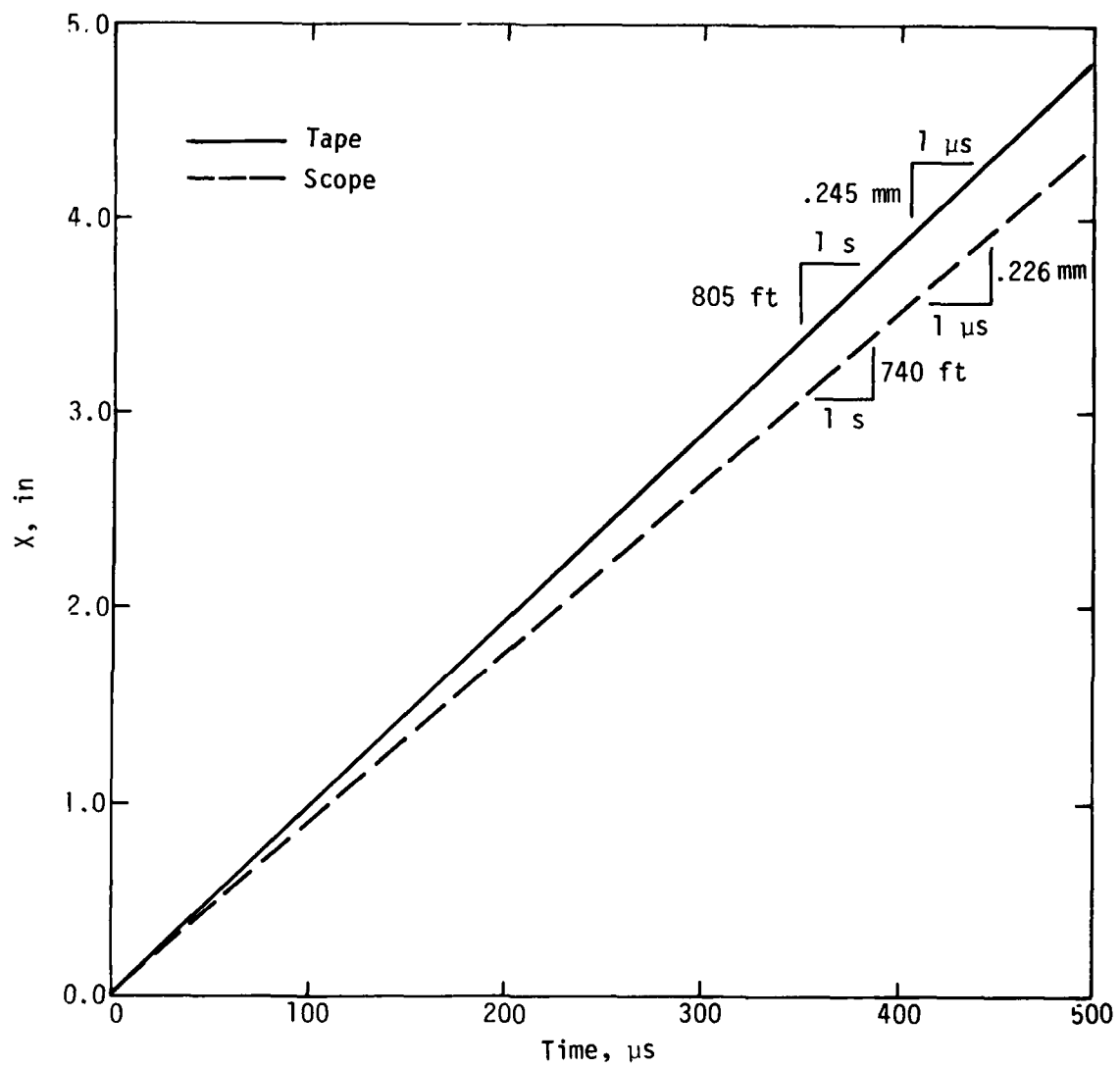


Figure 60. DABS III-A TOA 2 Data Reduction

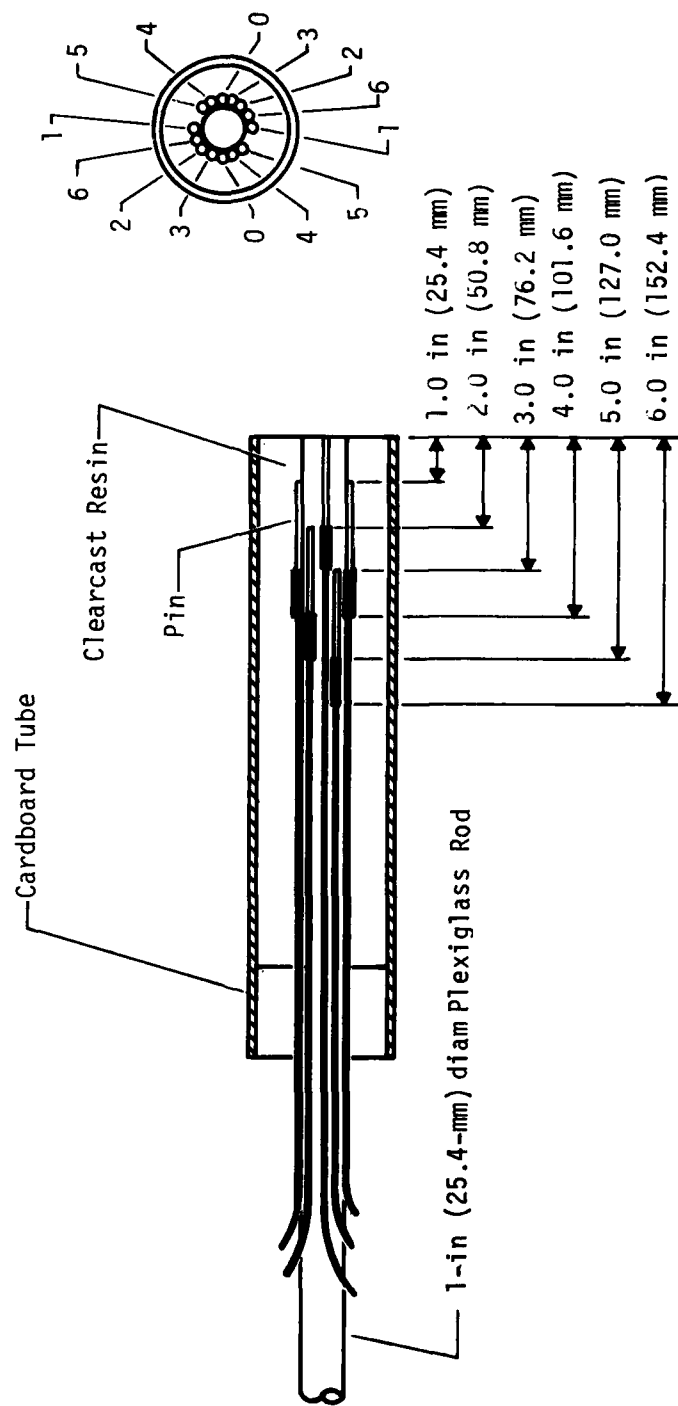


Figure 61. TOA 1 Gage, DABS-IIIA

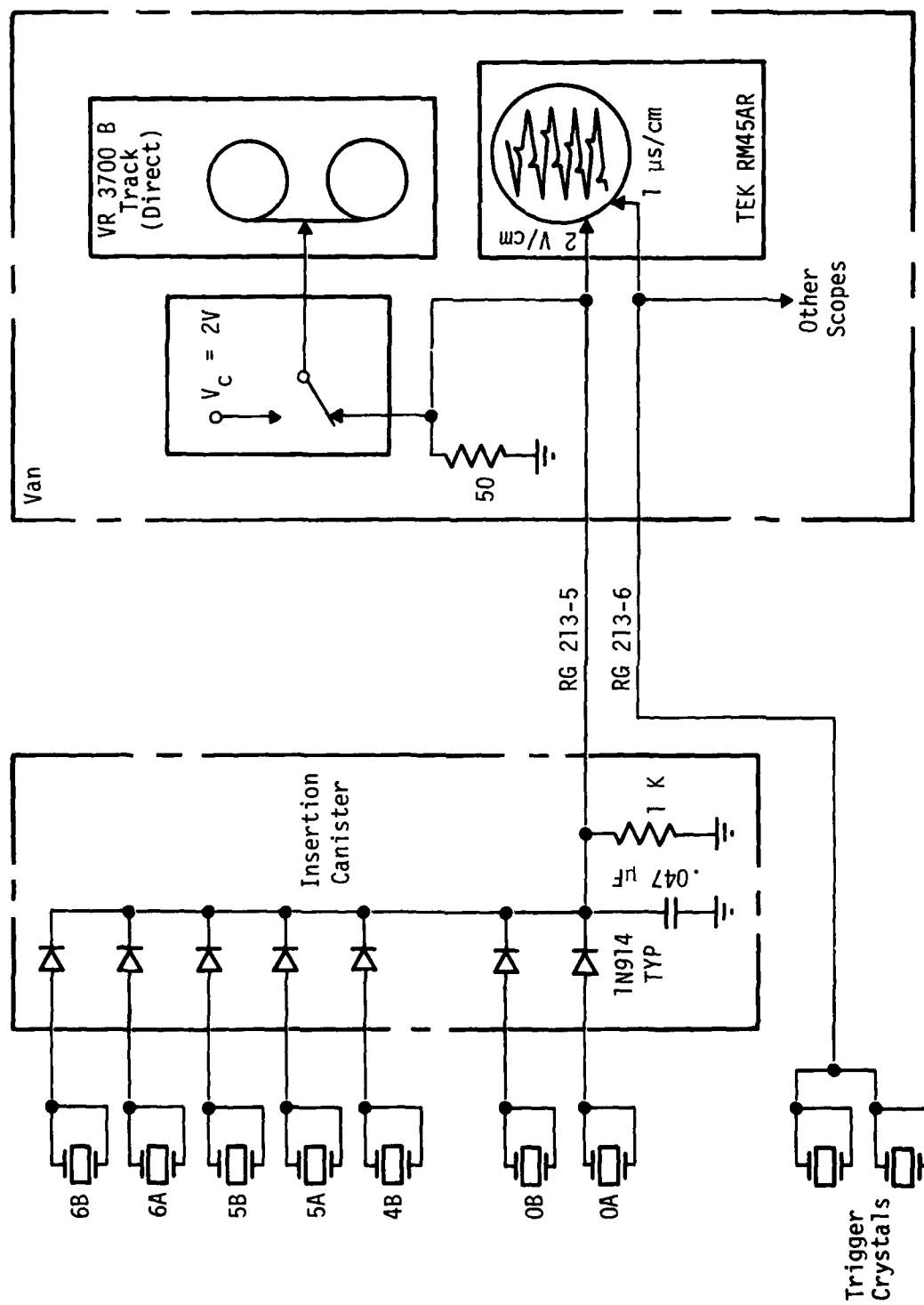


Figure 62. TOA 1 Instrumentation for DABS-IIIA

to the particle velocity. The MIPV consists of two rectangular loops, a primary (excitation) loop and a secondary (signal) loop. The loops are wound in bifilar fashion as shown in Figure 63. If it is postulated that a planar shock wave is propagating along the major axis of the gage, X, at velocity C, the ends of the loops are assumed to flow with the medium at particle velocity u. A (nearly) constant current is supplied to the primary loop. A voltage proportional to the rate of deformation of the loops (which is simply the particle velocity in the medium) is induced in the secondary loop. The voltage in the secondary loop is given by

$$V = - \frac{d\phi}{dt} = - \frac{d}{dt} MI \quad (23)$$

where

- V = Output voltage, Volts
- ϕ = Magnetic flux in the loops, Weber-meters
- M = Mutual inductance of the loops, Henrys
- I = Current in the primary loop, Amperes.

If the current in the primary loop is constant during the time of interest, then

$$V = -I \frac{dM}{dt} \quad (24)$$

For an on-axis, planar shock front,

$$\frac{dM}{dt} = \frac{\partial M}{\partial X} \frac{\partial X}{\partial t} = \frac{\partial M}{\partial X} u \quad (25)$$

where

$$u = \text{Particle velocity, mm}/\mu\text{s}$$

The partial derivative term can be made essentially constant by choosing the dimensions of the gage properly. Then the voltage output of the secondary loop is proportional to the particle velocity so long as the loops move with the particles in the medium. The gage output then becomes

$$V = \frac{\partial M}{\partial X} u I \quad (26)$$

where

$$\frac{\partial M}{\partial X} = \text{Gage factor, } \frac{\text{mV}(\mu\text{s})}{\text{AP}(\text{mm})}.$$

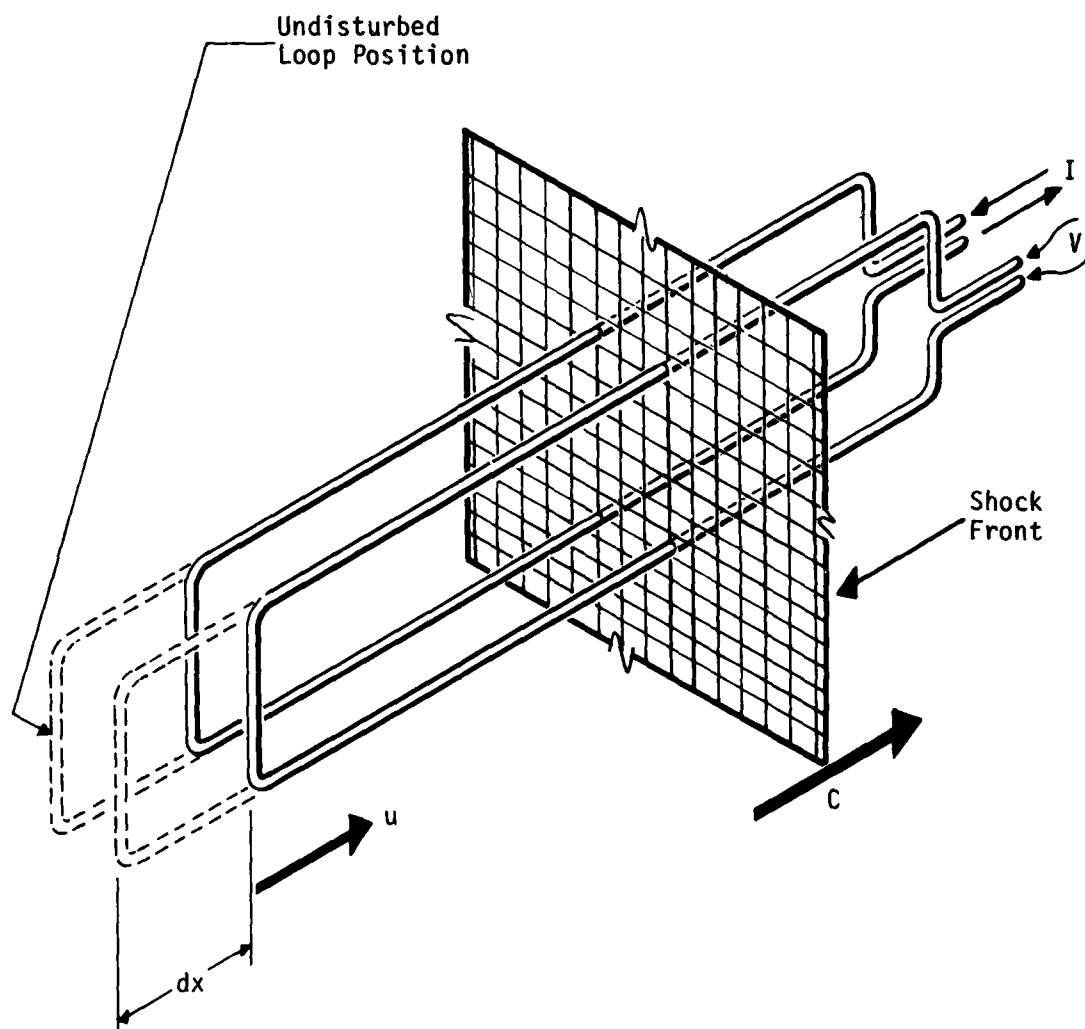


Figure 63. MIPV Gage Undergoing Deformation from Particle Motion

Renick Ref. 5 has tabulated mutual inductances and gage factors for various sizes of MIPVs. These tables were used to select the dimensions of the MIPV for DABS IIIA.

The "constant" current is supplied by discharging a large capacitor through the primary loop as shown in Figure 64a. The current is actually not constant, but is given by

$$I(t) = \frac{V_i}{2bL} e^{-at} (e^{bt} - e^{-bt}) \quad (27)$$

where

V_i = Initial voltage on capacitor

L = Inductance of the primary circuit

$$a = \frac{R}{2L}$$

$$b = \sqrt{a^2 - \frac{1}{LC}}$$

R = Resistance of primary circuit, ohms

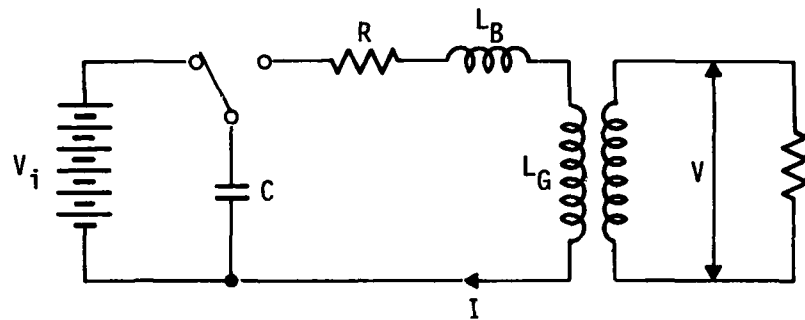
C = Capacitance of capacitor, Farads.

Figure 64b shows a plot of $I(t)$ for the particular values of L , R and C used on DABS IIA. These values were chosen to make $I(t)$ peak at about 1.2 ms after det 0, which was the expected time of arrival of the shock wave at the gage. This provides a window of about 1400 μ s when $I(t)$ may be taken as a constant.

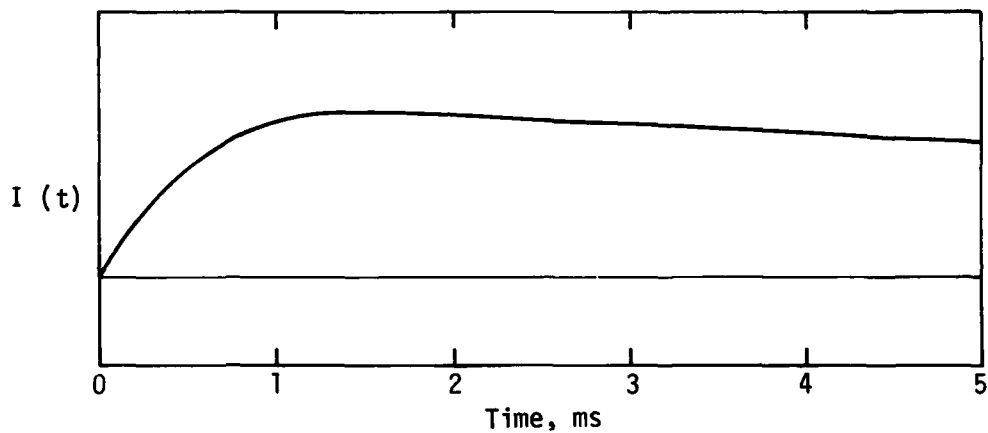
In order to obtain a large enough value of L to produce the current shown in Figure 64b, a ballast inductor of inductance L_B was introduced in the primary circuit, so that the total inductance L is the sum of L_B and the gage inductance, L_G .

The voltage output of the secondary is given by Equation 28. Taking M as a constant (before TOA when the gage is not subjected to a moving medium) and

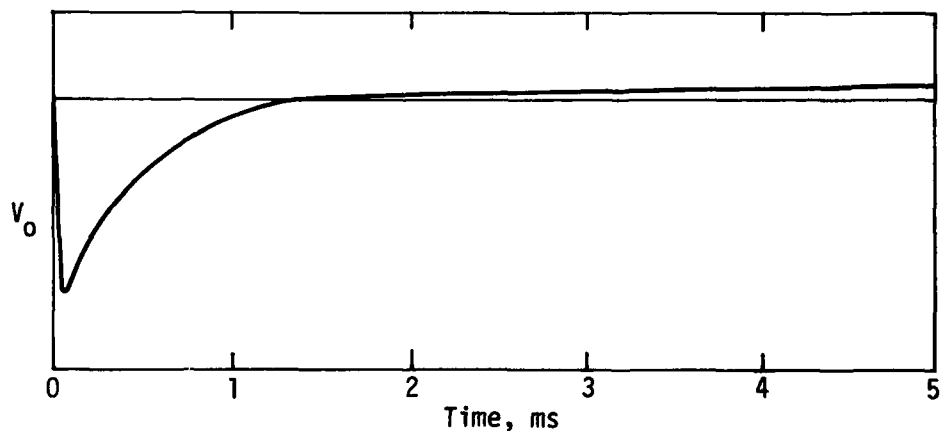
5. Renick, J. D., *Analysis of the Mutual Inductance Particle Velocimeter (MIPV)*, AFWL-TR-74-205, Air Force Weapons Laboratory, Kirtland AFB, New Mexico, November 1974.



(a) MIPV Circuit



(b) Current in Primary Circuit



(c) Voltage Across Secondary Loop

Figure 64. MIPV Circuit Characteristics

allowing I to vary according to Equation 27,

$$V(t) = -M \frac{dI(t)}{dt} \quad (28)$$

The output is plotted in Figure 64c. It is readily seen that the output is zero when the current in the primary loop is at its peak. This is the best time to take data. The timing of the discharge of the capacitor is adjusted so that $I(t)$ will be near its peak and thus essentially constant when the shock wave hits the gage.

The initial negative pulse in the output can be used to calculate I . Rewriting Equation 28,

$$MdI(t) = -V(t)dt \quad (29)$$

integrating Equation 29 up to the TOA of the shock wave at the gage yields the value of I at TOA:

$$\begin{aligned} \int_0^{TOA} MdI(t) &= - \int_0^{TOA} V(t)dt \\ MI_{TOA} &= \int_0^{TOA} V(t)dt \\ I_{TOA} &= \frac{1}{M} \int_0^{TOA} V(t)dt \end{aligned} \quad (30)$$

The integral can easily be obtained from the data.

The MIPV gage used on DABS-IIIA is shown in Figure 65. It features a 5-turn primary loop and a 4-turn secondary loop (both of #20 wire) on a 2-in (50.8-mm) x 2-in (50.8-mm) plexiglass substrate. The primary loop terminals are 1/4-20 brass studs to receive the large terminal lugs on the AWG #0 wire from the capacitor bank. The secondary loop is terminated by a BNC connector for convenience in attaching a signal cable. The end block is used to tighten the loops after they are wound, and then the substrate/loop assembly is potted

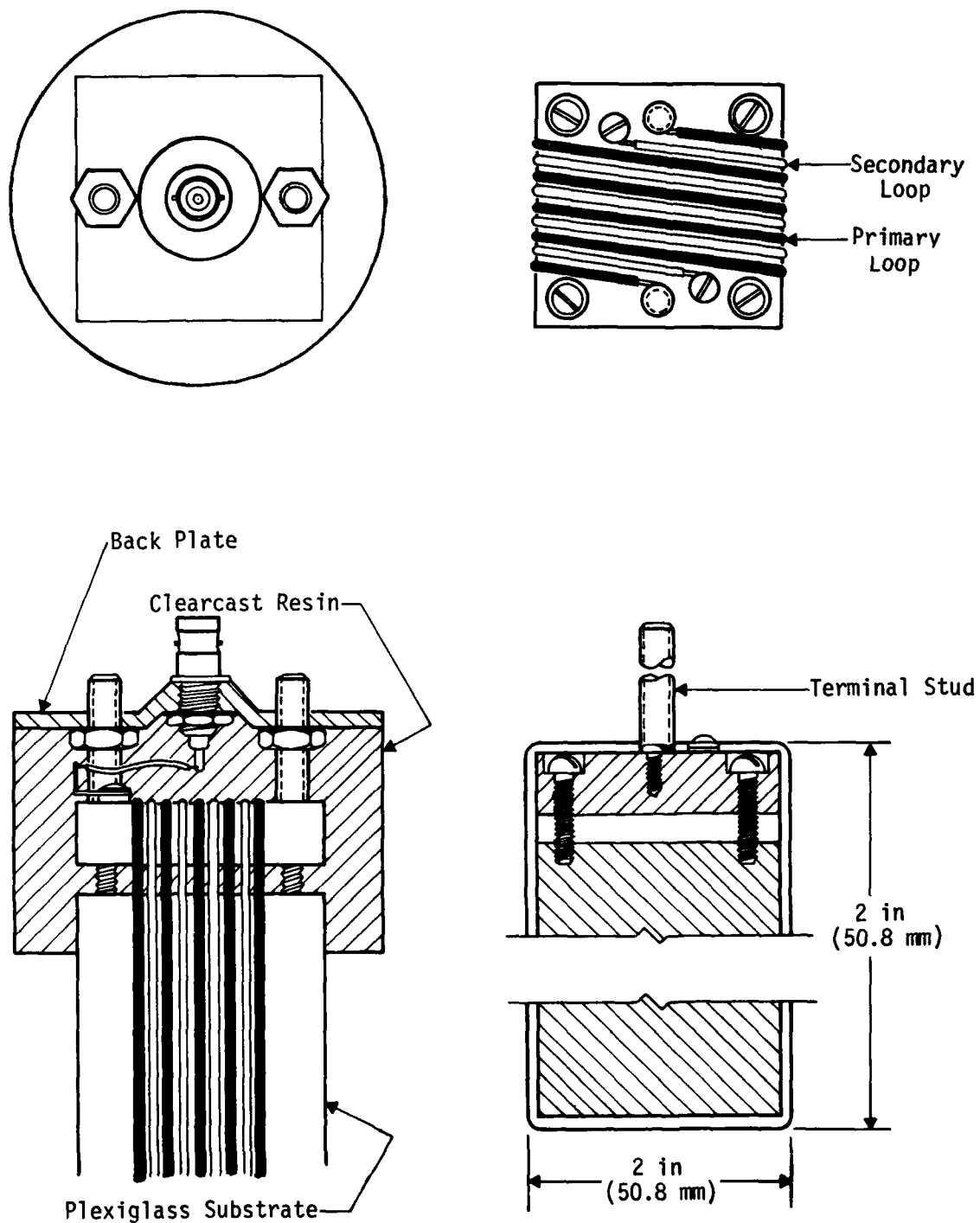


Figure 65. Mutual Inductance Particle Velocimeter (MIPV)

with the back plate to seal the terminal connections.

The instrumentation for the MIPV measurement on DABS-IIIA is shown in Figure 66. The capacitor is dumped into the primary of the gage by an SCR which is triggered by the fiducial pulse. The detonation of the explosive charge was delayed 1 ms by using an appropriate length of detonation cord between the detonator (which is fired at fiducial time) and the charge. This delay allowed the primary loop current to build up to its peak ("constant") value.

The specifications for the DAB-IIIA MIPV gage system are as follows:

Predicted particle velocity-----	0.8 mm/ μ s
Gage factor, $\frac{\partial M}{\partial X}$ (from Renick's table)-----	15.94 $\frac{\text{mV}(\mu\text{s})}{\text{A}(\text{mm})}$
Gage mutual inductance-----	8.477 μ H
Gage primary loop inductance-----	31.9 μ H
Gage resistance-----	0.21 Ω
Ballast inductor: 121 turns #20 wire, 8.5-cm diam x 19.43 cm long	
Ballast inductance-----	486.4 μ H
Ballast inductor resistance-----	250-300 VDC
Capacitance-----	0.015 F
Connection of capacitor to gage: 100 ft #0 wire	
Resistance at connection wires-----	.05 Ω
Primary circuit inductance-----	518.3 μ H
Primary circuit resistance-----	1.40 Ω

Using these specifications, $I(t)$ peaks at approximately 180 A at 1.4 ms. The expected voltage output is then

$$V = \frac{\partial M}{\partial X} \mu I = 15.94 \frac{\text{mV}(\mu\text{s})}{\text{A}(\text{mm})} \times 0.8 \frac{\text{mm}}{\mu\text{s}} \times 180 \text{ A} = 2295 \text{ mV} \quad (31)$$

or 2.3 V.

The data from the MIPV gage on DABS-IIIA is shown on the composite data plot, Figure 59. The initial peak is -4.31 V, and the data peak is 1.681 V.

Integrating the output up to the TOA of the shock gives

$$\int_0^{\text{TOA}} V(t) dt = 1.067 \times 10^{-3} \text{ V(s)} \quad (32)$$

Then using Equation 30,

$$I = \frac{1}{M} \int_0^{\text{TOA}} V(t) dt = \frac{1.067 \times 10^{-3} \text{ V(s)}}{8.477 \times 10^{-6} \text{ H}} = 125.8 \text{ A} \quad (33)$$

Using this value of I and rewriting Equation 26

$$u = \frac{V}{I \frac{\partial M}{\partial X}} = \frac{1681 \text{ mV}}{125.8 \text{ A } 15.94 \frac{\text{mV}(\mu\text{s})}{\text{A}(\text{mm})}} = 0.838 \text{ mm}/\mu\text{s} \quad (34)$$

This result is consistent with the prediction.

The MIPV gage is a simple, relatively easy-to-field gage which operated reliably on the DABS-IIIA event. Data reduction is not difficult but does require integration of the turn-on pulse.

The second time-variant magnetic field gage used for particle velocity measurements on DABS-IIIA was the Axially Symmetric Magnetic Prope (ASMP) developed by Los Alamos Scientific Laboratory (LASL).

The gage was built by staff at LASL who also supplied data reduction capability. It was fielded by UNM/CERF in the back wall of DABS-IIIA and was approximately 1.97 in (50 mm) away from the back surface of the explosive. The device is shown in Figure 67 and is described by Fritz and Morgan (Ref. 6). Basically it is a single, twin-magnetic coil attached to a coaxial cable (a). There was an aluminum plate (b) placed in front of this coil and separated by a void of length (Z). Three small plastic spacers (e) spaced 120 deg apart serve to elevate a plexiglass mounting disk (f) above the metal-free surface. The source of the magnetic field is a permanent ceramic magnet (g). The unit

6. J. Fritz and J. Morgan, *The Review of Scientific Instruments*, Vol. 44, p. 213, Feb. 1973.

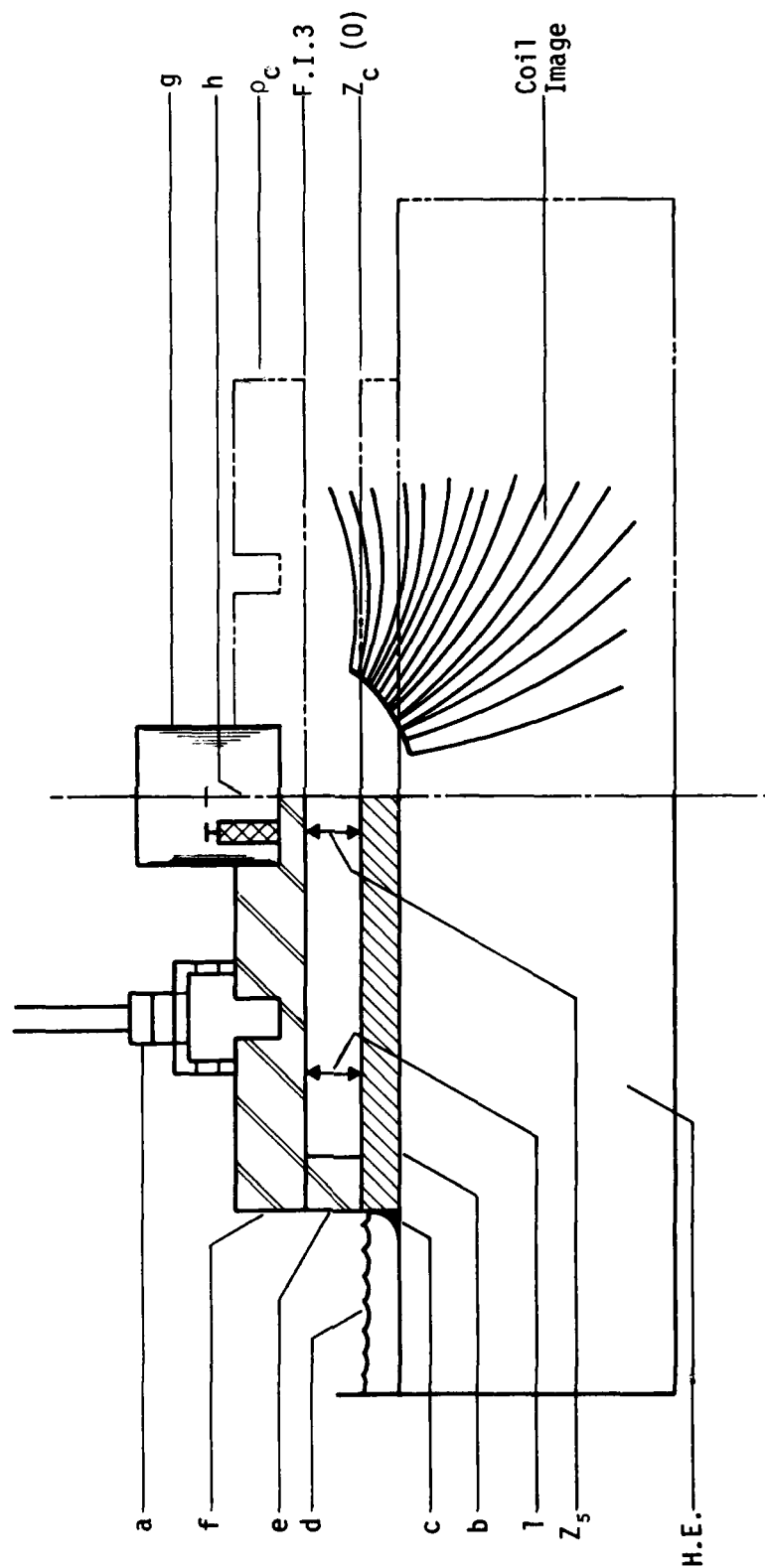


Figure 67. Construction and Magnetically Active Elements of an ASPM Probe

was mounted with the aluminum flush to the concrete; and the rest of the gage was encapsulated in front, leaving the void behind the aluminum plate.

The source of the signal picked up by the coil (h) is the time-varying eddy currents produced in the aluminum plate as it moves toward the magnet.

The result and voltage (E_t) produced can be described by the following equation:

$$E(t) = u_p(t) F(\zeta(t,t)) - [u_p(t) - u_i] \times \int_0^t dt' u_p(t') F'(\zeta(t,t)) - \infty \quad (35)$$

where $F(\zeta) = \sum_c \frac{2\pi p_c}{p} (p_c Z_c + \zeta)$ (Fig.68) u_p is the plate velocity and u_i is

recession image velocity (see method of images in virtually any electricity and magnetism text). The equation is solved by the use of an iterative technique developed at LASL.

The results of the experiment are shown in Figure 59. The average free surface velocity of the aluminum plate was 0.84 mm/ μ s. This corresponding particle velocity was half of this or 0.42 mm/ μ s in the aluminum. This corresponds to an approximate 0.80 to 0.90 mm/ μ s (Fig. 68) particle velocity in grout. This higher value than given by the MIPV was expected since the ASMP was closer to the explosive.

STRESS IN CHAMBER BACK WALL

It was intended to measure stress in the back wall of the chamber by the use of manganin stress gages at the locations shown in Figure 56. The two gages installed are shown in Figures 68 and 69. The instrumentation system is shown in Figure 70. It features pulsed d.c. excitation, which allows high gage currents to be used without damaging the gage since the power is only applied for a short time.

Unfortunately, because the power supply did not trigger, the only information obtained from the manganin gage system was an induced pulse at detonation and a self-generating response pulse at TOA (Fig. 59). The reason for the failure

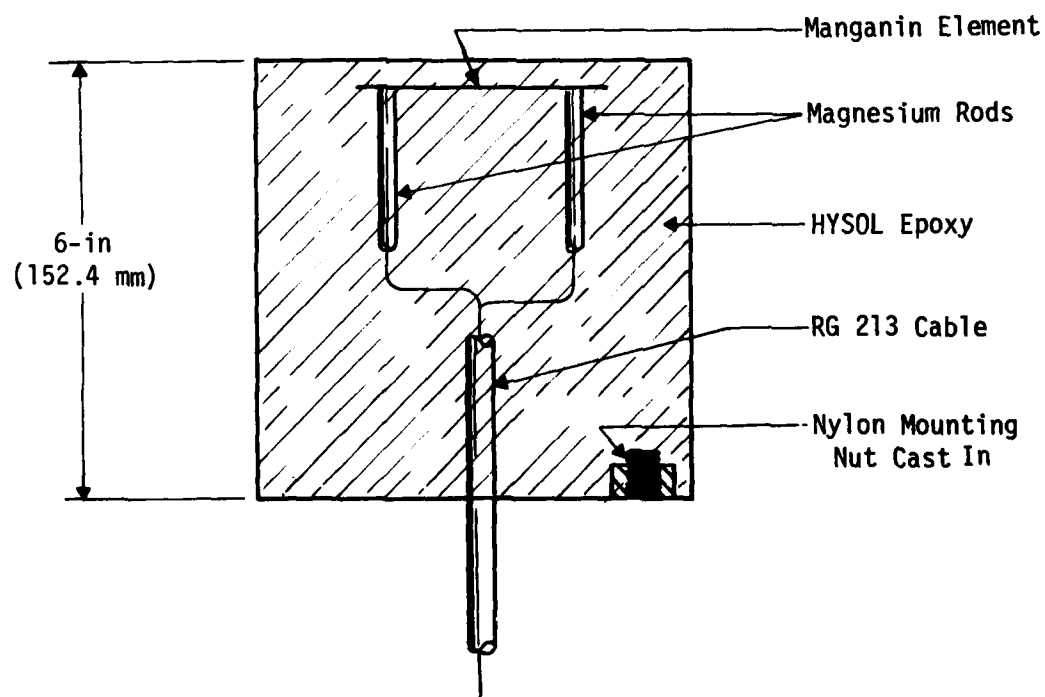
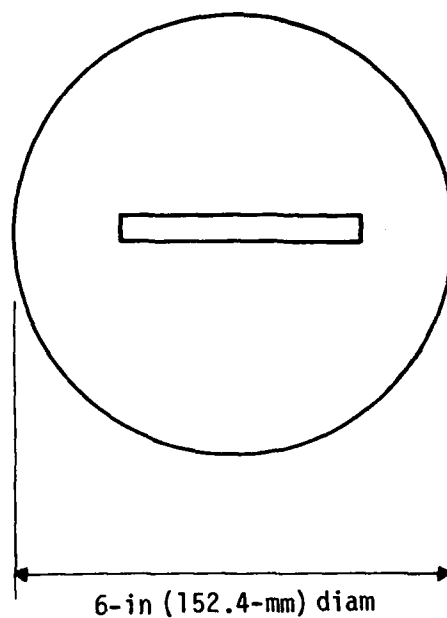
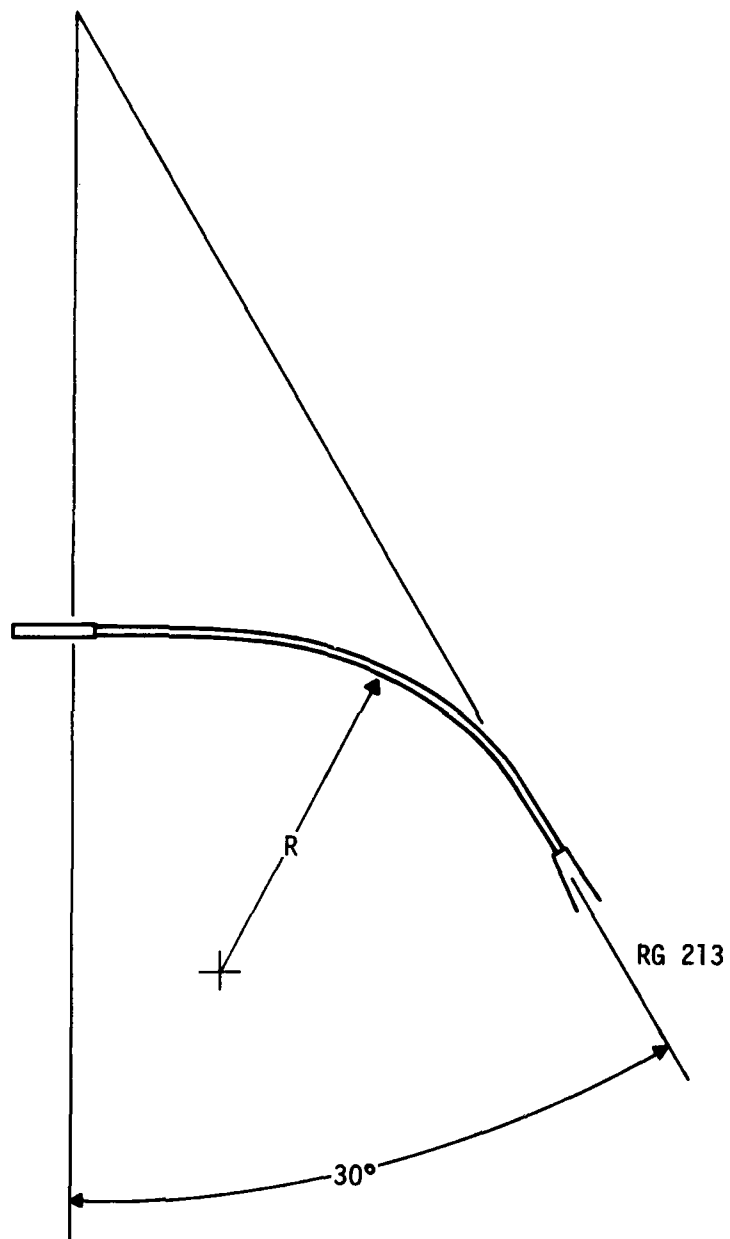


Figure 68. Manganin Gage Cylindrical Configuration - DABS-IIIA



Note: R to be such that the angle between output stem and a normal to the gage is ≤ 30 deg

Figure 69. Manganin Gage Flat Pack Configuration - DABS-IIIA

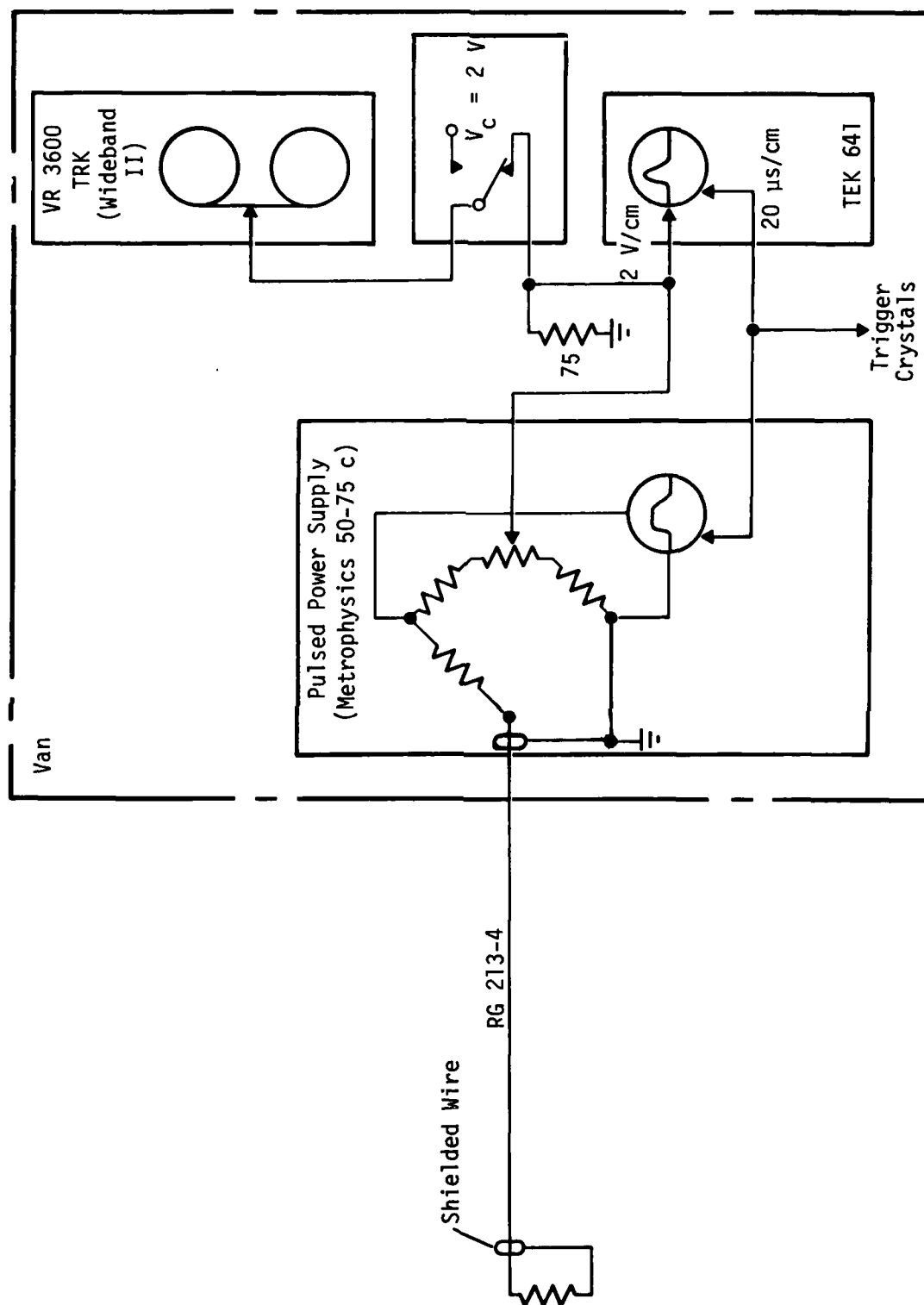


Figure 70. Manganin Gage Instrumentation DABS-IIIA

of the power supply trigger is unknown. The rest of the data acquisition system triggered properly and the manganin gage power supply triggered repeatedly on dry runs.

DISTRIBUTION LIST

ARPA (TIO)	Develco, Inc, Sunnyvale CA (L Rorden)
(NMRO)	Oakridge Natl Lab (Civ Def Res Proj, Kearny)
(PMO)	Boeing, Seattle (B Lempriere)
(STO)	(Aerospace Lib)
DTIC (DDA) (12 cy)	Civil Engr Rsch Fac UNM (N Baum) (10 cy)
DNA (SPTD)	H-Tech Labs, Santa Monica (B Hartenbaum)
FC/DNA (FCTMOF)	Kaman Sciences Corp, Colorado Springs
FC/DNA, Livermore (FCPRL)	(Library)
NATO School (SHAPE) (US Documents Off)	(D Sach)
Undersec of Def for Rsch and Engrg	Nathan M Newmark, Consulting Services
(Strat and Space Sys (OS))	Urbana IL (W Hall)
Harry Diamond Labs, Adelphi, MD	(Nathan Newmark)
(PRXDO-NP)	Physics Internatl Co, San Leandro
(DELHD-NP)	(C Vincent)
(DELHD-TI, Tech Lib)	(Doc Con for Tech Lib)
USACRREL (CRREL-EM)	(Doc Con for Fred M Sauer)
Civil Engrg Lab (R J Odello)	Geo-Centers, Newton Upper Falls MA
(Tech Lib)	(L Isaacson)
Naval Surface Wpns Cntr	Effects Technology, Santa Barbara CA
Silver Spring MD (Code F31)	(R Wengler)
AFWL (SUL) (2 cy)	R & D Assoc, Marina Del Ray CA
(HO)	(C MacDonald)
Asst Chief of Staff, Intelligence	(Tech Lib)
Dept of the Air Force, Washington	(J G Lewis)
(INT)	Systems, Science, and Software, La Jolla CA
BMO, Norton AFB (MNNH)	(Dr Donald R Grine)
(MNNM)	(Tech Lib)
AU, Maxwell AFB (AUL/LDE)	Weidlinger, Paul, Consulting Engr, New York
DOE, Lib Rm G-042, Washington	(Dr Melvin L Baron)
(Doc Con for Class Lib)	SAI, Las Vegas NV (K Sites)
LLL (Doc Con for Tech Info Dept and Lib)	The Singer Co, Fairfield NJ (J Evans)
Sandia Labs, LLL (Doc Con for Lib & Sec	Asst. to the Sec of Def, Atomic Energy
Clas Div)	DOD (Honorable Don R Cotter)
NBS (P Lederer) (31 cy)	DNA, Washington DC (TITL)
Artec Assoc, Inc, (D Baum)	(SPSS)
	FC/DNA (FCPR)
	(FCT)

US Army Engr Waterways Exper Sta, Vicksburg
(Leo Ingram)
(Library)
(F Hanes)
(J K Ingram)

US Army Mat Dev and Readiness Cmd
(Tech Lib)

US Army Nuc and Chem Agency (Library)

David W Taylor Naval Ship R&D Ctr
(Code L42-3 Library)

Naval Facilities Engr Cmd (Tech Lib)

Sandia Natl Labs
(Doc Con for 3141 Sandia R)
(Doc Con for Albert Chabai)
(Doc Con for Luke Vortman)

DOE Albuquerque Operations Ofc
(Doc Con for Tech Lib)

DOE Nevada Operations Ofc
(Doc Con for Tech Lib)

AF Inst. of Technology, AU
(Lib AFIT Bldg 640 Area B)

AFWL, AFSC (SUL)
(NTE, M A Plamondon)
(HO, Dr Minge)

Aerospace Corp (Tech Info Services)
(P Mather)

Agbabian Assoc, (M Agbabian)

Civil/Nuclear Systems Corp, Albuquerque
(J Bratton)

EGG&G Wash Anal Serv Ctr, Albuquerque
(Tech Lib)

General Electric Co, TEMPO-Ctr for Adv Studies
(J Shoutens)
(DASIAC)

Merritt CASES inc (J L Merritt)
(Tech Lib)

IIT Research Inst (Tech Lib)

TRW Def & Space Sys Group, San Bernardino
(F Y Wong 527/712)

SRI International, Menlo Park
(George R Abrahamson)
(Burt Gasten)

TRW Def & Space Sys Group, Redondo Beach
(Peter K Dai RI/2170) (2 cy)
(Tech Info Center/S-1930)

Weidlinger Assoc Consulting Engrs (J Isenberg)

SAI, La Jolla (Tech Lib)

Southwest Research Inst (A B Wenzel)
(Wilfred E Baker)

JAYCOR, Bedford MA (H Linerude)

Terra Tek Inc (S Green)

California Rsch & Tech Inc (K Kreyenhagen)

Electromechanical Sys of NM Inc (R Shunk)

Ofc of Naval Rsch (Code 715, Tech Lib)

US Army Ballistic Rsch Lab
(Tech Lib)
(J H Keefer, DRDAR-BLE)
(DRDAR-BLV)

Dpty Chief of Staff for R&D, Dept of the Army
(DAMA-AOA-M, Tech)

Naval Ship Engrg Ctr (Code 09G3, Tech Lib)

US Army Engr Waterways Exper Sta, Vicksburg
(William Flathau)

Official Record Copy, AFWL/NTED
(Joe V Quintana)